Color-Based Models For Outdoor Machine Vision

Shashi Buluswar

CMPSCI TR 02-11

COLOR-BASED MODELS FOR OUTDOOR MACHINE VISION

A Dissertation Presented

by

SHASHI D. BULUSWAR

Submitted to the Graduate School of
The University of Massachusetts Amherst in partial fulfillment
of the requirements for the degree of

DOCTOR OF PHILOSOPHY

February, 2002

Department of Computer Science

COLOR-BASED MODELS FOR OUTDOOR MACHINE VISION

A Dissertation Presented

by

Shashi D. Buluswar

Approved as to style and content by:

Allen R. Hanson, Chair

Bruce A. Draper, Member

Edward M. Riseman, Member

Andrew G. Barto, Member

Michael Skrutskie, Member

Bruce Croft, Department Chair
Computer Science

ABSTRACT

COLOR-BASED MODELS FOR OUTDOOR MACHINE VISION

FEBRUARY, 2002

SHASHI D. BULUSWAR, B.A., GOSHEN COLLEGE

M.S., UNIVERSITY OF MASSACHUSETTS AMHERST

Ph.D., UNIVERSITY OF MASSACHUSETTS AMHERST

Directed by: Professor Allen R. Hanson

This study develops models for illumination and surface reflectance for use in outdoor color vision, and in particular for predicting the color of surfaces under outdoor conditions. Existing daylight and reflectance models that have been the basis for much of color research thus far have certain limitations that reduce their applicability to outdoor machine vision imagery. In that context, this work makes three specific contributions: (i) an explanation of why the current standard CIE daylight model cannot be used to predict the color of light incident on surfaces in machine vision images, (ii) a model (table) mapping the color of daylight to a broad range of sky conditions, and (iii) a simplified adaptation of the frequently used Dichromatic Reflectance Model for use with the developed daylight model. A series of experiments measure the accuracy of the daylight and reflectance models by predicting the colors of surfaces in real images. Finally, a series of tests demonstrate the potential use of these methods in outdoor applications such as road-following and obstacle detection.

TABLE OF CONTENTS

LIST OF TABLES

LIST OF FIGURES

CHAPTER 1

INTRODUCTION

1.1 Overview

Several outdoor machine vision applications (such as obstacle detection [51], road-following [16] and landmark recognition [11]) can benefit greatly from accurate color-based models of daylight and surface reflectance. Unfortunately, as Chapter 4 will show, the existing standard CIE daylight model [42] has certain drawbacks that limit its use in machine vision; similarly, as Chapter 5 will show, existing surface reflectance models [56][70][80] cannot easily be used with outdoor images. In that context, this study makes three contributions: (i) an explanation of why the CIE daylight model cannot be used to predict light incident upon surfaces in machine vision images, (ii) a model (in the form of a table) mapping the color of daylight against a broad range of sky conditions, and (iii) an adaptation of the frequently used Dichromatic Reflectance Model [80] for use with the developed daylight model.

One notable application of the above models is the prediction of *apparent color*.[1] Under outdoor conditions, a surface's apparent color is a function of the color of the incident daylight, the surface reflectance and surface orientation, among several other factors (details in Chapter 2). The color of the incident daylight varies with the sky conditions, and the surface orientation can also vary. Consequently, the apparent color of the surface varies significantly over the different conditions. The accuracy of the

[1] In this study, the phrase *apparent color* of a surface refers to the physical measurement of the surface's color in an image.

developed daylight and reflectance models is tested over a series of experiments predicting the apparent colors of surfaces in real outdoor images.

1.2 Variation of apparent color

The following examples describe why robust models of daylight and reflectance are important for outdoor color machine vision. Figure 1.1 and Figure 1.2 demonstrate the variation in the apparent color of two matte surfaces across 50 images. These images were taken under a variety of sky conditions, ranging from a clear sky to an overcast sky, with the sun-angle between 5° (dawn and dusk) and 60° (mid-day). The illumination angle (i.e., the orientation of the surface with respect to the sun) varied from 0° to 180°, and the viewing angle (the angle between the optical axis and the surface) varied from 0° to 90°. Figure 1.1(a) shows an image with the two target surfaces; from each such image, the *RGB*[2] value of each surface was determined by averaging the pixels over a small portion of the surface (from the circles), in order to reduce the effect of pixel-level noise. Figure 1.1(b) shows the *RGB* color from a single image—predictably, the samples from each surface form a single point. Figure 1.2(a) shows the variation in apparent *RGB* color of the surface patches over the 50 images, and Figure 1.2(b) shows the variation in the intensity-normalized *rgb* space.[3]

---

[2] While there are some canonical "*RGB*" spaces [37], manufacturing inaccuracies cause each camera to, in effect, have its own unique *RGB* space. Hence, each camera should be calibrated to determine its unique response parameters; the calibration parameters for the camera used in this study are shown in Chapter 2.

[3] The *rgb* space is a normalized form of *RGB*, and is used to eliminate the effect of brightness. In *rgb*, $r=R/(R+G+B)$, $g=G/(R+G+B)$, and $b=B/(R+G+B)$; hence, $r+g+b = 1$ and given r and g, $b=1-r-g$. Therefore, *rgb* is a two-dimensional space that can be represented by the *rg* plane.

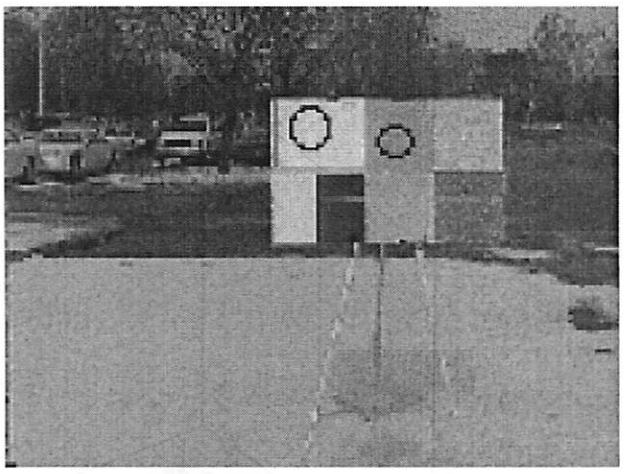

(a) Sample image

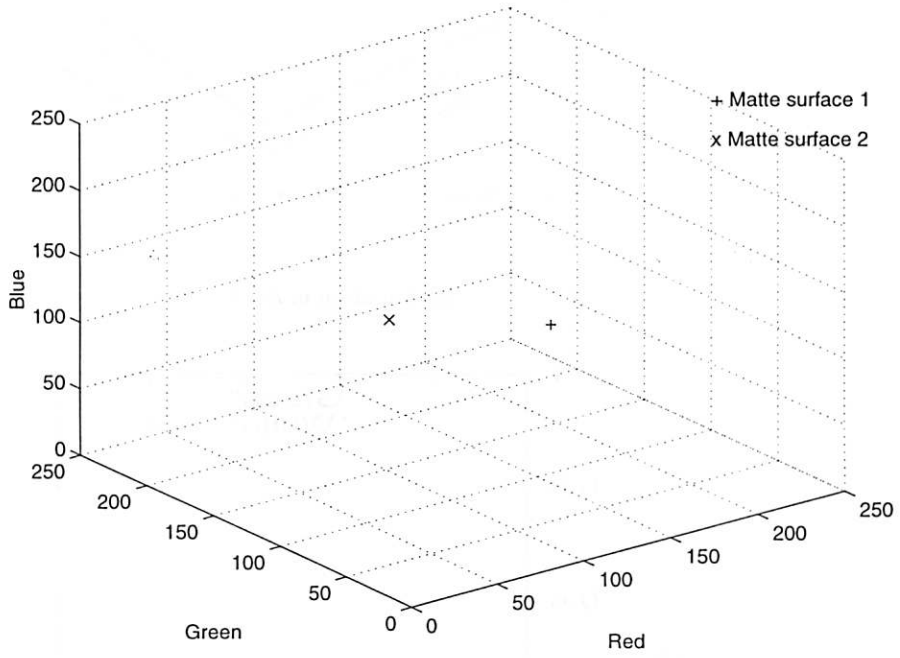

(b) *RGB* color from a single image

Figure 1.1. (a) Samples from two matte surfaces (extracted from the circles); (b) the *RGB* color from a single image.

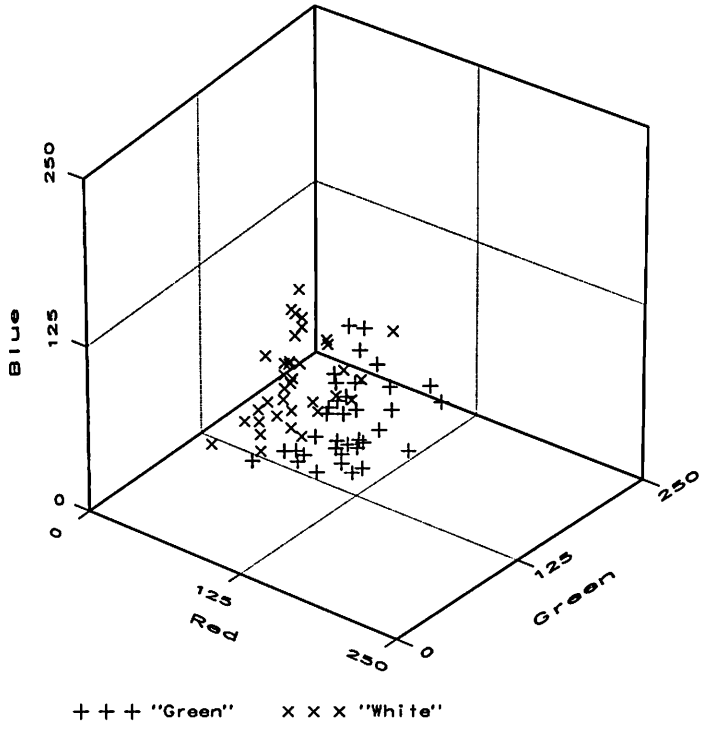

(a) Variation in *RGB*

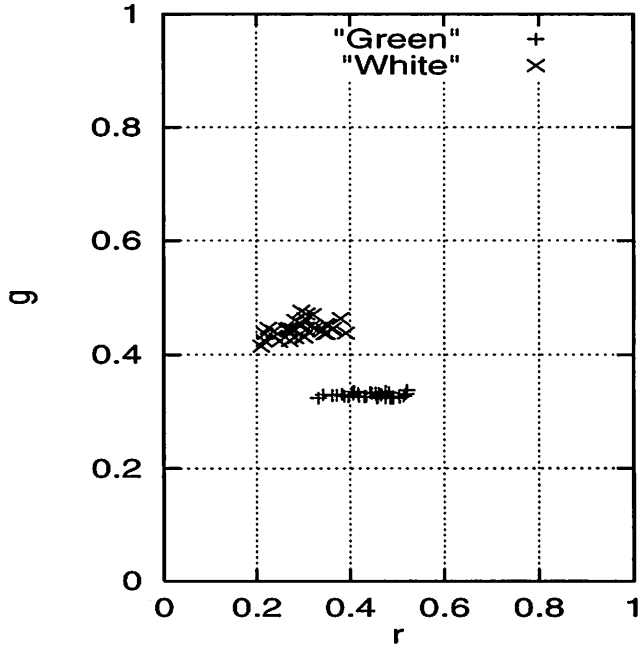

(b) Variation in *rgb*

Figure 1.2. Variation in the apparent color of the sample matte surfaces over 50 images (a) in the *RGB* space; (b) in *rgb*.

As the figures show, the apparent color of the two surfaces is not constant; rather, it varies significantly over the range of conditions in both *RGB* and *rgb*. The Cartesian spread of the clusters representing each surface is about 90 units (from a range of 0-255) in *RGB* (with a standard deviation of 35) and about 0.2 (out of the possible 0-1 range) units in *rgb* (with a standard deviation of 0.05). The significance of these numerical measures can be understood in two ways: first, in *RGB*, a range of 90 represents more than one-third of the overall range along each dimension (which is 255); in *rgb*, 0.2 is one-fifth of the entire range. Secondly, the *RGB* spread is about 250% of the distance between the centroids of the two clusters, while the *rgb* spread is about 105% of the inter-centroid distance. This means that the overall variation in the apparent color of a single surface can be greater (in terms of Cartesian distance in color space) than the difference between two perceptually distinct colors (in this case, white and green). The factors causing the variation in apparent color are examined in Chapter 2.

While Figure 1.1 and Figure 1.2 show the variation in the apparent color of simple matte surfaces, Figure 1.3 and Figure 1.4 show the variation for a specular surface—a "Stop" sign—from 50 images over the same range of illumination and viewing conditions as before.[4] Figure 1.3 shows "Stop" signs at two different orientations: (a) one facing away from the sun, and (b) the other, facing the sun (i.e., with the surface normal in the azimuthal direction of the sun, and partially reflecting the sun into the camera). Figure 1.4 shows the variation in (a) *RGB* and (b) *rgb*, respectively, as the orientation and illuminating conditions change. As the figures demonstrate, the variation in apparent color of a specular surface can form a bi-modal distribution. In this case, the Cartesian

[4] Note that the traffic signs used in this study are privately owned, and do not have retroreflective or fluorescent properties that are required for some public signs. Appendix A contains a more detailed description of these two phenomena.

distance between the centroids of the two clusters is about 195 units in *RGB* and about 0.23 units in *rgb*. In addition, as Figure 1.4(b) shows, a specular surface may be non-uniformly colored in an image when direct sunlight is incident upon it. Hence, a portion of the "Stop" sign is the characteristic red, while another portion exhibits the specular effect.[5]

Human beings are able to adapt to this evidently significant color shift due to a mechanism called color constancy, which is a combination of biological and psychological mechanisms. Although much work has been done on the processes involved in human color constancy [2][6][7][34][45][86], it has proven difficult to successfully simulate the proposed models in computational systems. The aforementioned examples suggest that in machine vision images, the notion of a color associated with an object is precise only within the context of scene conditions. The discussion in Chapter 6 shows that models of daylight color and surface reflectance, combined with a small number of reasonable assumptions, is an effective way of modeling scene context.

The discussion in the following chapter shows that color images of outdoor scenes are complicated by phenomena that are either poorly modeled or described by models which will more parameters to an already complicated problem. As a result, computational color recognition has been a difficult and largely unsolved problem in unconstrained outdoor images. To that end, the two models developed in this study—the daylight and reflectance models—are shown to be effective in relatively uncontrolled outdoor environments.

[5] Note that the characteristic specular effect of specular surfaces is apparent only when the surfaces are large enough to reflect a portion of direct light onto the camera.

Please note that while color prediction is an ideal application to test the two models, it is *not* the sole reason for their development; rather, the models attempt to add new insight into two important processes in outdoor color machine vision (namely, illumination and reflectance). The color prediction experiments discussed in Chapter 6 require input on some subset of the following parameters of scene context: sun angle, cloud cover, illumination angle, viewing angle and sun visibility.

1.3 Overview of chapters

Chapter 2 examines various factors that affect outdoor color images. Chapter 3 examines relevant existing work in color machine vision and shows that existing methods make assumptions that are not appropriate for unconstrained outdoor images.

In Chapter 4 it is shown that the existing standard model of daylight (the CIE model [42]) has limitations when applied to machine vision images due to the effect of ambient light and ground reflection. Hence a model of daylight is built, such that the color of the incident daylight can be predicted, given the sun-angle and sky conditions.

Chapter 5 shows that the prevalent surface reflectance models [56][70][80] cannot be easily applied to outdoor images because of their use of brightness values and their assumptions about the illumination and the independence of the specular effect from illumination; the Normalized Photometric Function (NPF) is then developed by simplifying the existing physics-based models for use in outdoor images.

Chapter 6 combines the daylight and NPF models in order to estimate the apparent color of a target surface under a given set of conditions, and then to classify image pixels as target or background.

Chapter 7 discusses the results from tests on images from road scenes; finally, Chapter 8 discusses directions of potential future research based on this study.

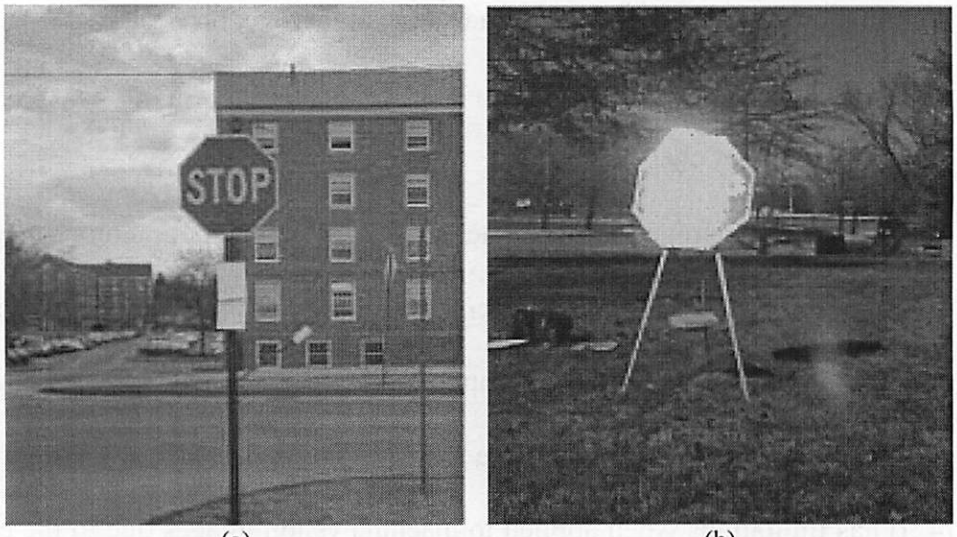

(a) (b)

Figure 1.3. Images of a specular "Stop" sign at two different orientations: (a) facing away from the sun; (b) facing the sun.

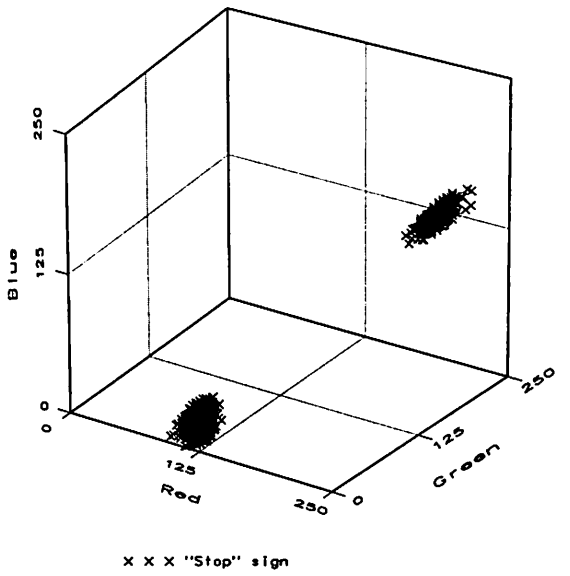

(a) Variation in *RGB*

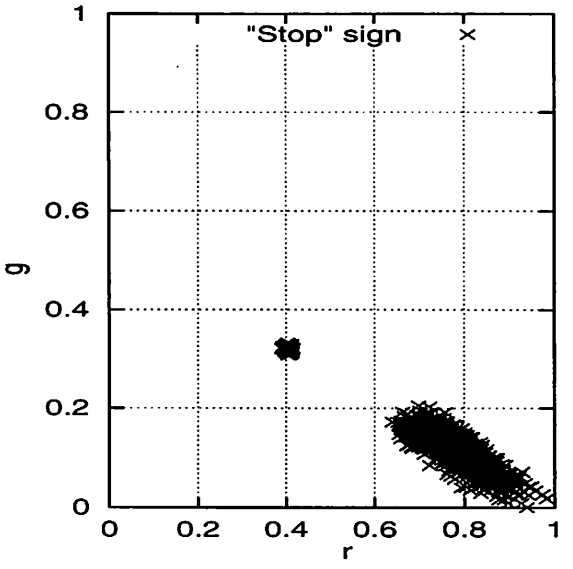

(b) Variation in *rgb*

Figure 1.4. Variation in the apparent color of a specular "Stop" sign over 50 images in: (a) the *RGB* space; (b) *rgb*.

CHAPTER 2

FACTORS IN OUTDOOR COLOR IMAGES

2.1 Overview

Since one major motivation of the models developed in the study is to predict the apparent color of surfaces in outdoor images, this chapter discusses the significant processes involved: (a) the color of the incident daylight, (b) surface reflectance properties, (c) illumination geometry (orientation of the surface with respect to the illuminant), (d) viewing geometry (orientation of the surface with respect to the camera), (e) response characteristics of the camera (and peripheral digitization hardware), (f) shadows, and (g) inter-reflections. In typical outdoor images, some of these factors remain constant, while others vary. Those that do vary can cause a significant shift in apparent surface color. The following sections provide some background on the processes involved in color and image formation, and examine the factors causing the variation in apparent surface color.

2.2 Light, the visual spectrum, and color

Visible light is electromagnetic energy between the wavelengths of about 380nm and 700nm. Figure 2.1 shows the visible spectrum along with the colors represented by the various wavelengths.

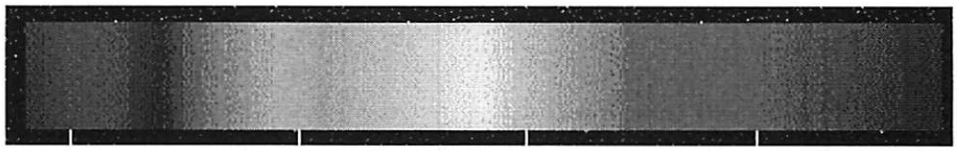

Figure 2.1. The visible electromagnetic spectrum, approximately between 380nm and 700nm. Just below and above the limits are the ultraviolet and infrared wavelengths, respectively.

Light can be represented by a *Spectral Power Distribution* (SPD) in the visual spectrum, which plots the energy at each wavelength (usually sampled at discrete intervals) between 380nm and 700nm. Figure 2.2 shows simplified SPD's that represent colors that are shades of pure (a) "red", (b) "green", (c) "blue", and (d) "white".[6] In this example, the red, green and blue SPD's peak at about 670nm, 550nm and 450nm, respectively. The white SPD, on the other hand, is flat, since white (by definition) contains an equal proportion of all colors.[7]

The SPD's shown in Figure 2.2 are simplified; only very spectrally concentrated light sources will have such SPD's. The SPD representing the color of daylight is not as narrow or smooth, as shown in Figure 2.3, which represents a typical blue cloudless sky [48][94].

[6] The names of the colors are in quotes because these are perceptual associations rather than precise definitions.

[7] The vertical axis for SPD's denotes the energy radiated; often, the energy measurements at the various wavelengths are normalized [94] and represented relative to a given wavelength. Hence, there is no unit of measurement along the vertical axis.

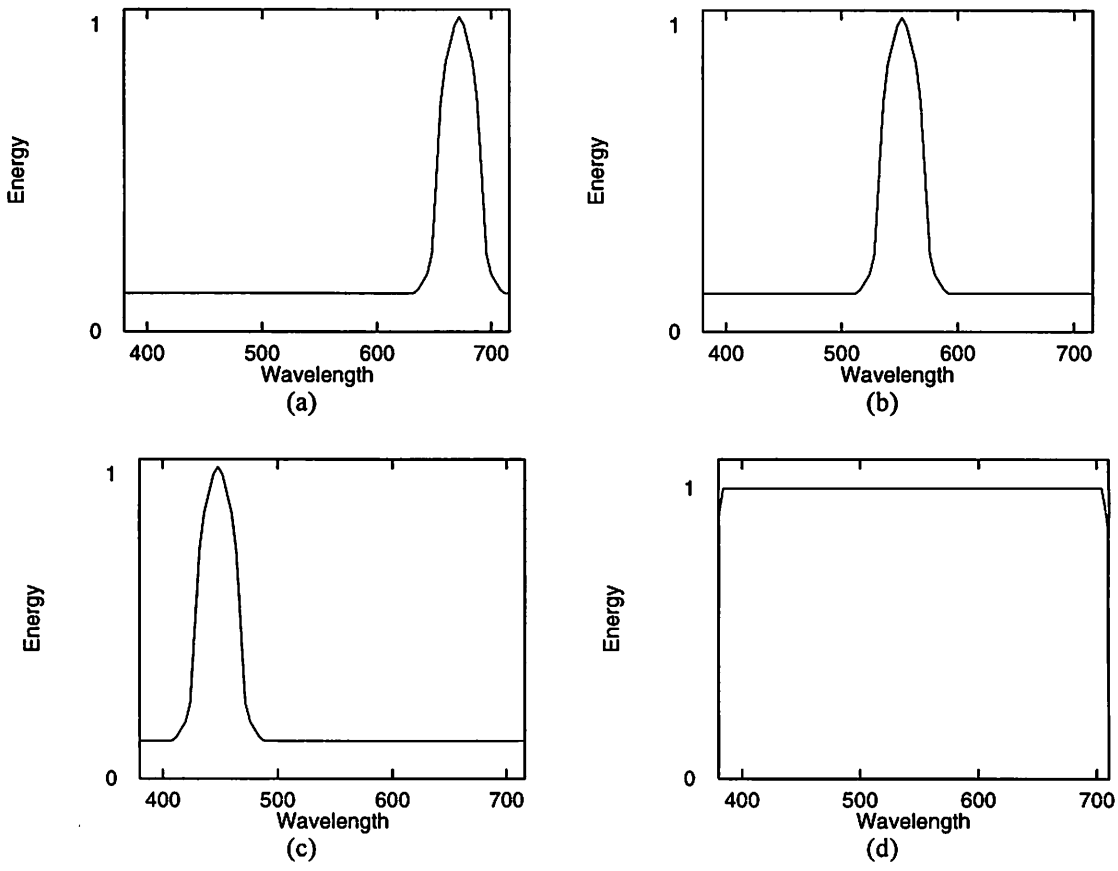

Figure 2.2. Simplified Spectral Power Distributions (SPD's) for (a) red, (b) green, (c) blue, and (d) white. The SPD's for the first three colors have peaks at different wavelengths, whereas the white SPD is flat.

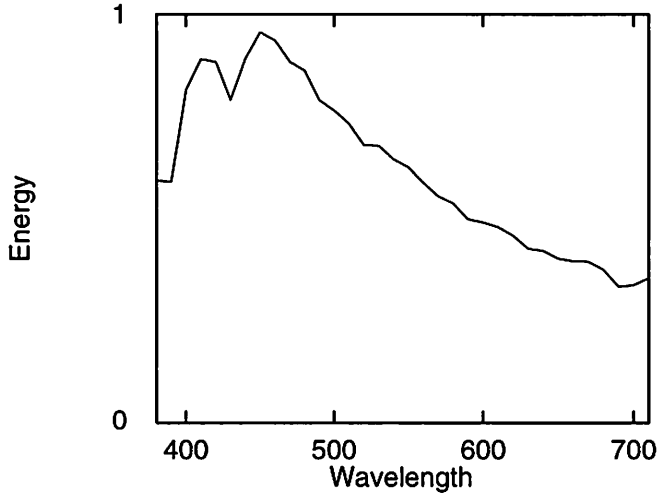

Figure 2.3. Sample spectral power distribution for daylight from a blue cloudless sky.

2.3 The effect of illumination

When light is incident upon a surface, the surface's *albedo* determines how much of the incident energy along each wavelength is reflected off the surface, and how much is absorbed. The resultant reflection, which is the product of the SPD of the incident light and the albedo, is also represented by an SPD. Figure 2.4 shows the albedo for two surfaces, blue and green, which are from the Munsell[8] color set (numbers 10Bv9c1, and 10Gv9c1, respectively) [48][55].

When white light is incident upon a surface, the SPD of the resultant reflection is the same as the albedo. However, if the incident light is colored (for instance, red), the resultant SPD is different from the albedo. If the incident light is a different color (blue, for instance), the resultant SPD can be significantly different from that under red light. In outdoor images, the color of the incident daylight is seldom white[9] and certainly not constant; it varies significantly, depending on the sun-angle, cloud cover, humidity, haze and atmospheric particulate matter [36][42]. Figure 2.5 shows the SPD for the color of daylight from "reddish" sunlight (at a low sun-angle) [66]; the SPD for this phase of daylight is quite different from the one shown in Figure 2.3.

Figure 2.6 and Figure 2.7 show the SPD's of the two surfaces from Figure 2.4 under the two phases of daylight described in Figure 2.3 and Figure 2.5. As the SPD's indicate, the reflections off the surfaces under different illuminating conditions are significantly different.

---

[8] The Munsell color chart is a standard set of colors that is often used by color scientists.
[9] The color of daylight is closest to white when the whole sky is covered by white clouds; even then, it can have a non-trivial blue component.

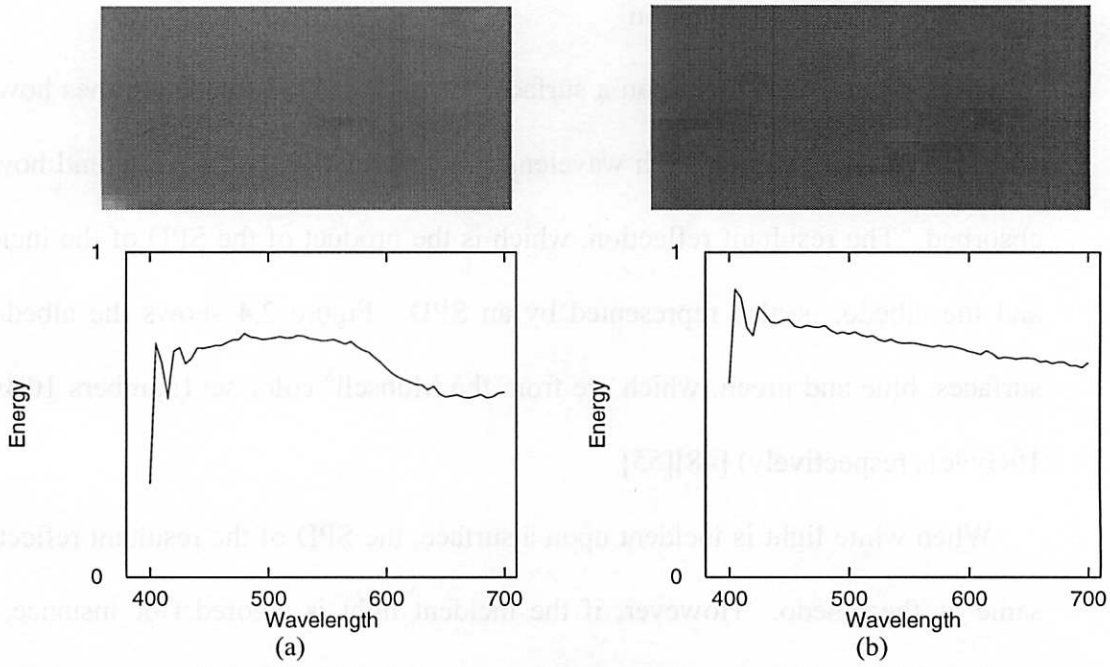

Figure 2.4. Normalized SPD's representing the albedos for two colors from the Munsell set: (a) green (Munsell 10Gv9c1), (b) blue (Munsell 10Bv9c1). Note that the SPD's for these surfaces are more complicated than the simple SPD's shown in Figure 2.2.

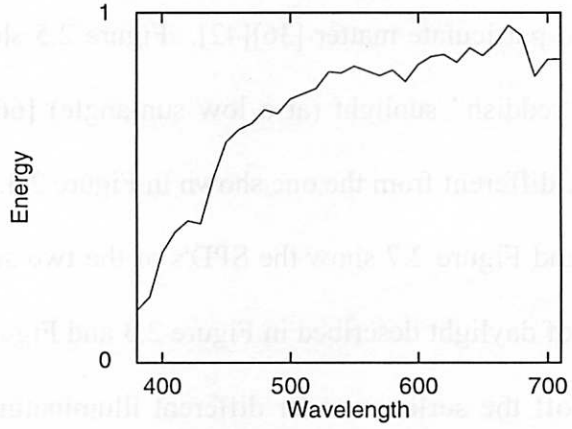

Figure 2.5. Sample spectral power distribution for daylight from "reddish" sunlight.

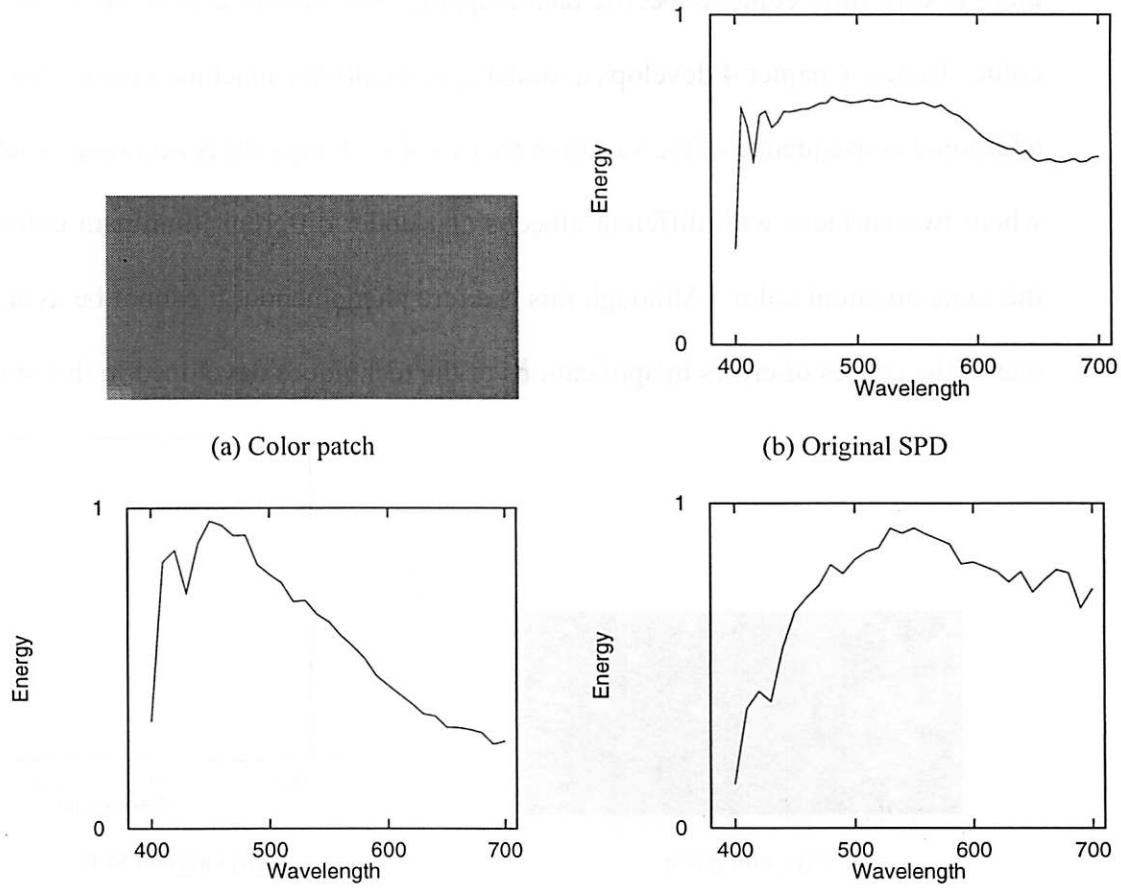

(a) Color patch (b) Original SPD

(c) SPD under blue sky (d) SPD under red sun

Figure 2.6. The Munsell green (number 10Gv9c1) patch (a), with the SPD representing its albedo (b). The SPD of the apparent color of the patch changes (c and d) as the illuminant changes from blue sky to red sun.

The variation in the color of daylight is caused by changes in the sun-angle, cloud cover, and other weather conditions. In addition, the presence of haze, dust and other particulate pollutants can also affect the color of daylight in localized areas [36]. The CIE model [42] has served as the standard for the variation of the color of daylight, and has empirically been shown to be accurate in *radiometric data*. However, as Chapter 4 shows, the model has three disadvantages when applied to *machine vision images*, namely that it does not account for the effect of ambient light or ground reflection, and

there is very little context-specific data mapping illumination conditions to incident light color. Hence, Chapter 4 develops a model specifically for machine vision. Note that one additional consequence of the variation in the color of daylight is illuminant metamerism, where two surfaces with different albedos and under different illuminant colors, map to the same apparent color. Although this is a rare phenomenon, it cannot be avoided and is one of the causes of errors in applications of the techniques developed in this study.

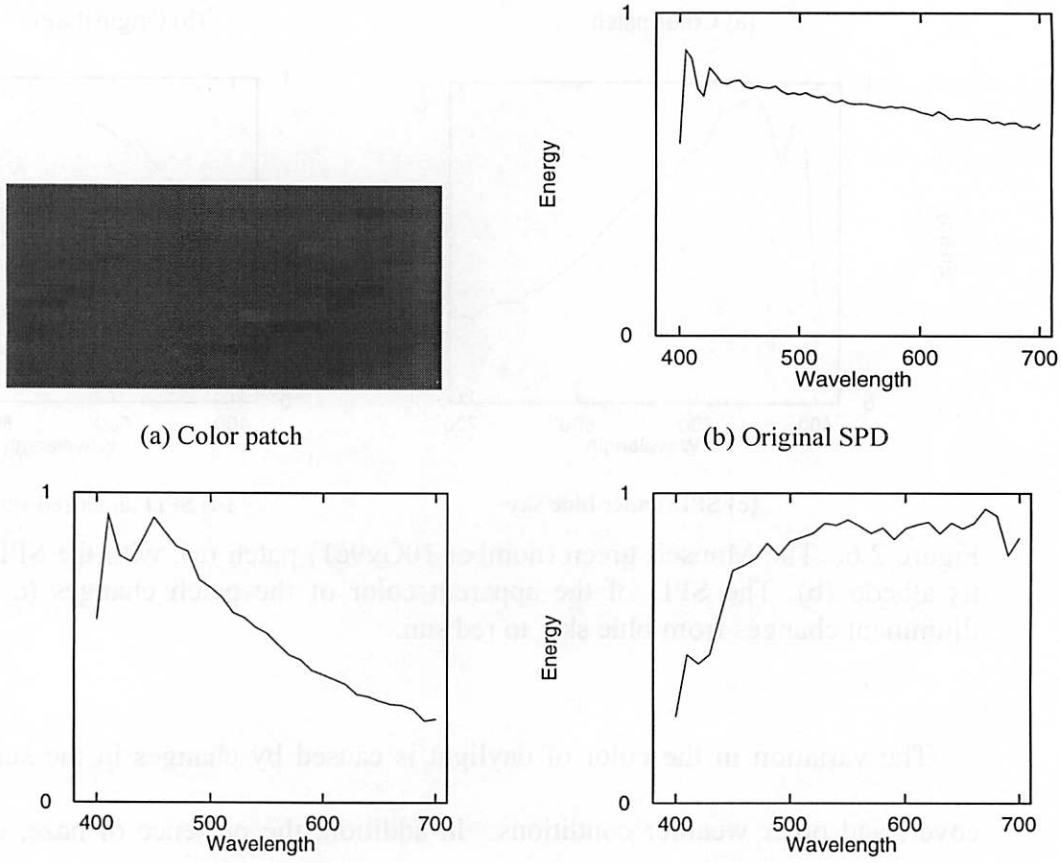

(a) Color patch

(b) Original SPD

(c) SPD under blue sky

(d) SPD under red sun

Figure 2.7. The Munsell blue (number 10Bv9c1) patch (a) with the SPD representing its albedo (b), and the SPD's under (a) blue sky, and (d) red sun.

2.4 The effect of surface orientation and reflectance

Illumination geometry, i.e., the orientation of the surface with respect to the sun, affects the composition of the light incident upon the surface. Daylight has two components, sunlight and ambient skylight, and the surface orientation determines how much light from each source is incident on the surface. For instance, a surface that faces the sun is illuminated mostly by sunlight, whereas one that faces away is illuminated entirely by the ambient skylight and light reflected off other surfaces in the scene. The reflectance properties of the surface determine the combined effect of illumination geometry and viewing geometry (i.e., its *relative* viewing geometry). Figure 2.8 explains some of the terminology related to surface orientation. The strength of the specular reflectance component of the surface, based on the combined geometry of illumination and viewing, affects the composition and amount of light reflected by the surface onto the camera (as shown earlier in Figure 1.3 and Figure 1.4). While physics-based reflectance models exist [46][56][70][80], they cannot be easily used with outdoor images because (i) they assume single-source illumination, (ii) they do not account for the effect of illuminant obscuration on the specular effect, and (iii) they rely on illuminant brightness, which cannot be easily estimated for daylight (shown in Chapter 5). Hence, Chapter 5 develops the Normalized Photometric Function, which can be applied to outdoor data and to the daylight model developed earlier in the same chapter.

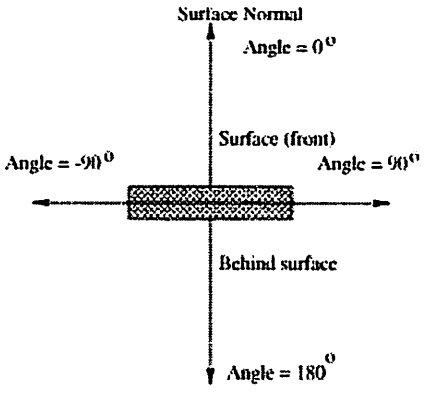

Figure 2.8. The geometry of illumination and viewing depends on the position of the illuminant and camera (respectively) with respect to the surface. Along the surface normal, the angle is 0°, and ranges from 90° to 90° on either side of the surface normal. The *relative viewing geometry* is the combination of the illumination and viewing geometries.

2.5 The effect of the sensor

Before a discussion of the effect of sensor (camera) characteristics, the following description of color spaces may be helpful. A color digital image represents scenes as two-dimensional arrays of pixels. Each pixel is a reduced representation of an SPD, where the reduction depends on the color space being used. One commonly used space is the three-dimensional *RGB* (Red-Green-Blue) space, which is derived from a set of (three) trichromatic filters [94]. While there are canonical "*RGB*" spaces, manufacturing inaccuracies cause each camera to, in effect, have its own unique *RGB* space. Hence, each camera should be calibrated to determine its unique response parameters; the calibration parameters for the camera used in this study are shown in Table 2.1. Figure 2.9(a) shows the spectral transmission curves for a set of three filters[10] used to derive a hypothetical *RGB*. For each pixel, the product of each of the trichromatic filters and the input SPD is integrated, and the resulting sum then becomes the value of the pixel along

[10] The filters shown in Figure 2.9 are the CIE color matching functions [94]. The *RGB* color space(s) used by most cameras are linear transforms of these functions [37].

the corresponding dimension. The *RGB* space represents the brightness (intensity) of a pixel along each dimension, ranging (usually) from 0 to 255. In such a framework, the color "black" is represented by the value [0,0,0], "white" by [255,255,255], a pure bright "red" by [255,0,0], "green" by [0,255,0], and "blue" by [0,0,255] (once again, the colors' names are in quotes because these are qualitative and perceptual associations rather than precise quantitative definitions.). One of the consequences of reducing the representation of color from the continuous SPD function to a three-dimensional value is that a number of physically different SPD's can be mapped to the same *RGB* value. This phenomenon is known as observer metamerism, and even humans perceive metamers as being similar; fortunately, this type of metamerism is not a common occurrence in practice.

The *RGB* space can be *normalized* over total brightness, such that $r=R/(R+G+B)$, $g=G/(R+G+B)$, and $b=B/(R+G+B)$. The normalized space, referred to hereafter as *rgb*, eliminates the effect of brightness, and the value along each of the dimensions (in the range 0-1) represents the pure color without brightness. Hence, black, white, and all the grays in between are mapped to the same value [0.33,0.33,0.33]. In *rgb*, $r+g+b = 1$; given the values along only two of the dimensions, the third can be determined. Therefore, *rgb* is a two-dimensional space.

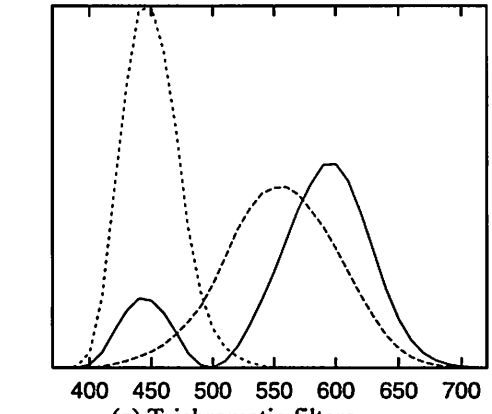

(a) Trichromatic filters

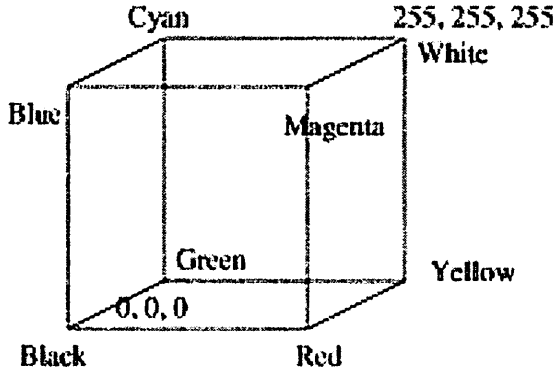

(b) *RGB* space

Figure 2.9. Trichromatic filters (a) used to reduce an SPD to the RGB color space (b). Of the three filters, the "red" filter peaks at about 440nm, "green" at about 550nm, and the "blue" filter has a large peak at about 600nm and a smaller one at about 440nm.

Factor	Model	Comments
Focal length	6.5mm (equivalent to 37mm on a 35mm camera)	
Color filters	Based on NTSC *RGB* standard primaries [76]	Calibration required
White point	[0.326, 0.341, 0.333]	Obtained with a calibrated white surface (Munsell N9/) under D65 illuminant
Gamma correction	$\gamma = 0.45$	f-stop adjusted to stay in the 50-75%, (approximately linear) output range
Aperture range	f/2.8 to f/16	Aperture adjusted with f-stop
Shutter speed	1/30 to 1/175 seconds	
Image resolution	756×504, 24-bit RGB	
Gain	2.0 e-/count	Fixed

Table 2.1. Parameters of the camera used in this study.

The response characteristics typical to digital cameras (or other imaging devices used for machine vision) can cause apparent surface color to shift in a number of ways. In the process of reducing the SPD's at individual pixels to *RGB* digital values, a number of other approximations and adjustments are made, some of which have a significant impact on the resultant pixel colors, while others have a relatively small effect. To begin with, wavelength-dependent displacement of light rays by the camera lens onto the image plane due to chromatic aberration can cause color mixing and blurring [5]. However, experiments in the literature [5] suggest that the effects of chromatic aberration will have a significant impact only on those methods that depend on a very fine level of detail. Observer metamerism, introduced in the previous section, occurs when different SPD's are mapped to the same *RGB* value [92]. Although this process does not shift or skew the apparent color of an object, it can cause ambiguity since two physically distinct colors (with respect to their respective SPD's) can have the same *RGB* value; in practice, as mentioned before, this does not occur very often. Many cameras perform pixel-level color interpolation on their CCD (Charge-Coupled Device) arrays, which convert the incident light energy at every pixel (photo-cell) to an electrical signal. On the photo-receptor array, each pixel contains only one of the three *RGB* filters, and the other two values are calculated from neighboring pixels at a later stage. Figure 2.10(a) shows the color filter array in the Kodak DC-40 digital camera. After the reduction of the SPD's to three separate electrical signals, the digitizer converts each input electrical signal to a digital value. Many digitizers use a nonlinear response function because the output of the camera is assumed to be a monitor or other display device (the phosphors for which are inherently nonlinear). The nonlinear response of the digitizer is meant to compensate for

the monitor nonlinearity; while this may help in displaying visually pleasing images, it can cause a problem for image analysis. The nonlinear response function is determined by a gamma-"correction" factor (shown in Figure 2.10(b)), which is 0.45 for many commonly used digital cameras [18]. On many cameras, gamma-correction can be disabled; on others it is possible to linearize the images through a calibration lookup table [60]. The dynamic range of brightness in outdoor scenes accentuates the possibility of clipping (photo-cell/pixel saturation) and blooming (draining of energy from one saturated photo-cell to a neighboring photo-cell) [60]. Although pixel clipping is easy to detect, there are no reliable software methods for correcting the problem. Blooming is difficult to even detect; while fully saturated pixels can easily be detected, the effect on photo-cells receiving excess energy from neighboring cells is more difficult to detect. Hence, blooming is not easily detectable or correctible [60].

The images used in this study were collected using a Kodak digital camera (customized DC-40), the relevant parameters for which are listed in Table 2.1. The automatic color balance on the camera was disabled, and the f-stop adjusted so that the output was always in the 50-75% (approximately linear) range; this avoided nonlinear response and pixel clipping. In addition, a color calibration matrix was obtained based on standard techniques [76], using a calibrated white surface (Munsell N9/) under a D65 illuminant. However, three other camera-related problems, namely blooming, chromatic aberration, and the mixed-pixel effect were considered either unavoidable or negligible, and not addressed specifically.

G	R	G	R	G	R	G
B	G	B	G	B	G	B
G	R	G	R	G	R	G
B	G	B	G	B	G	B
G	R	G	R	G	R	G
B	G	B	G	B	G	B

(a) Pixel interpolation

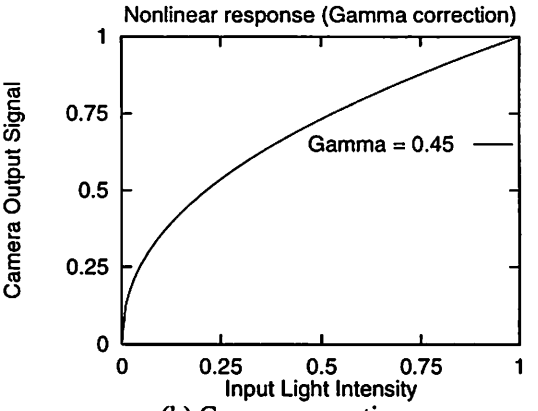

(b) Gamma-correction

Figure 2.10. Sources of color shifts in digital cameras: (a) pixel interpolation, (b) nonlinear response. With pixel interpolation each pixel (photo-cell) has only one color filter, and the other two color values are approximated from neighboring pixels. With gamma-"corrected" nonlinear response, the output signal is adjusted for display purposes according to the rule ($o = i^{\gamma}$), where o is the output signal, i is the input light intensity, and γ the correction factor.

2.6 Shadows and inter-reflections

Inter-reflections and shadows can cause a further variation in apparent color by adding indirect incident light or by restricting the effect of the existing light sources, thereby altering the color of the light incident upon the surface. Inter-reflections, for instance, cause light reflected off other surfaces in the scene to be incident upon the surface being examined. In fact, Chapter 4 shows that the color of daylight departs significantly from the CIE daylight model, due in part to light reflected off the ground. Beyond that, however, the effect of inter-reflections in complicated scenes can be hard to estimate [31]. Therefore, in this study, it is assumed that the scenes do not contain large, brightly colored objects near the target surface.

Shadowing can be of two types: self-shadowing and shadowing by another object. Chapter 4 shows that when the object is self-shadowed, the final effect is that the surface is illuminated both by skylight and by indirect sunlight reflected off the ground; this

effect is taken into account while determining the color of the incident light. On the other hand, if a surface is shadowed by a secondary object, the effects depend on the secondary object, and can cause all the effects of self-shadowing and additional inter-reflection off the secondary object. In this study, since it is assumed that there is no significant inter-reflection (other than off the ground), it is assumed that the effect of secondary shadowing is no different from that of self-shadowing.

Table 2.2 summarizes the various factors that contribute to the variation of apparent color in outdoor images, along with relevant models for those factors and the problems (if any) with those models. Note that many of these factors apply to indoor images as well.

The above discussion indicates that color images of outdoor scenes are complicated by phenomena that are either poorly modeled or inadequately described by models which add more parameters to an already complicated problem. As a result, problems such as apparent color prediction have been difficult and largely unsolved in unconstrained outdoor images. To that end, the contributions of this work include useful context-based models of daylight and reflectance that can be applied when either full or partial contextual information is available.

Factor	Models	Problems	Solutions
Daylight: Sun-angle & sky conditions	CIE [42]	• Little or no context-based information • Does not account for ambient or stray/indirect light	• Context-based model developed • Model accounts for moderate amounts of stray and incident light
Daylight: Haze, pollution	None	Difficult to model [36]	Ignored
Reflectance: Surface orientation (w.r.t., illuminant and camera)	Lambertian [38]; Dichromatic [80]; Hybrid [56]; Shading [70]	• Assumptions about single-source illuminant • Use of brightness values • Specular effect does not account for illuminant obscuration	• Models adapted for extended 2-source illuminant (daylight) • Brightness issues eliminated by normalization • Reflectance model explicitly accounts for illuminant obscuration
Camera: Nonlinear response	Supplied with camera	Nonlinear only near extremes of sensor range	f-stop adjusted: only middle, approximately linear range used
Camera: Chromatic aberration	Boult [5]	Affects mostly edge pixels	Ignored
Camera: Clipping	Novak [60]	Can be detected but not corrected	Pixels detected and eliminated
Camera: Blooming	Novak [60]	Cannot be easily detected or corrected	Ignored
Shadows	None [31]	Difficult to model	• Self-shadowing modeled as incident ambient light • Direct shadowing ignored
Inter-reflections	None [31]	Difficult to model	• Ground reflection modeled in daylight model • Other inter-reflections ignored

Table 2.2. Factors affecting the apparent color of objects in outdoor images, existing models and problems (if any) with those models, as well as ways in which this study addresses the problems.

CHAPTER 3

PREVIOUS WORK

3.1 Overview

This chapter discusses prevalent work in three areas: color prediction/recognition techniques (e.g., color constancy) in Section 3.2, models of daylight in Section 3.3, and surface reflectance models in Section 3.4. As Section 3.2 shows, research in color machine vision has a rich history; however, there has been little work exploring issues in outdoor images. The primarily physics-based models in Sections 3.3 and 3.4 that are related to the issues in this work make strong assumptions that may not hold in outdoor images.

3.2 Color machine vision

Research in color machine vision has a rich history, although relatively little of it explores issues in outdoor images. Existing work in relevant aspects of color vision can be divided into two categories: computational color constancy and physics-based modeling. In addition, there is a body of research related to color vision in the areas of parametric classification [16], machine learning techniques [10], color-based segmentation [51][64][79], application-driven approaches [16][73], and color indexing [28][82][85]. Finally, a number of other studies have been developed for particular applications or domains [12][13][41][54][67][71][84][88][91][96], but do not deal with issues related to outdoor color images.

3.2.1 Color constancy

Most of the work in computer vision related to the variation of apparent color has been in the area of color constancy, where the goal is to match object colors under varying, unknown illumination without knowing the surface reflectance function. An illuminant-invariant measure of surface reflectance is recovered by first determining the properties of the illuminant.

Depending on their assumptions and techniques, color constancy algorithms can be classified into six categories [26]: (1) those which make assumptions about the statistical distribution of surface colors in the scene, (2) those which make assumptions about the reflection and illumination spectral basis functions, (3) those that assume a limited range of illuminant colors or surface reflectances, (4) those which obtain an indirect measure of the illuminant, (5) those which require multiple illuminants, and (6) those which require the presence of surfaces of known reflectance in the scene. Among the algorithms that make assumptions about statistical distributions, von Kries and Buchsbaum assume that the average surface reflectance over the entire scene is gray (the gray-world assumption) [8][44]; Gershon [31] assumes that the average scene reflectance matches that of some other known color; Vrhel [89] assumes knowledge of the general covariance structure of the illuminant, given a small set of illuminants; and Freeman [25] assumes that the illumination and reflection follow known probability distributions. These methods are effective when their assumptions are valid. Unfortunately, as the examples in Chapter 1 (Figure 1.1, Figure 1.2, Figure 1.3, Figure 1.4) show, no general assumptions can be made about the distribution of surface colors without knowledge of the reflectance, even

if the distribution of daylight color is known. Consequently, these methods are too restrictive for all but very constrained scenes.

The second category of color constancy algorithms make assumptions about the dimensionality of spectral basis functions [81] required to accurately model illumination and surface reflectance. For instance, Maloney [49] and Yuille [95] assume that the linear combination of two basis functions is sufficient. It is not clear how such assumptions about the dimensionality of spectral basis functions in wavelength space apply to a reduced-dimension color space, such as the tristimulus *RGB* (Finlayson [22] discusses this issue in greater detail).

Among the algorithms that assume limits on the potential set of reflectances and colors in images is Forsyth's CRULE (coefficient rule) algorithm [24], which maps the gamut (continuum) of possible image colors to another gamut of colors that is known *a priori*, so that the number of possible mappings restricts the set of possible illuminants. In a variation of the CRULE algorithm, Finlayson [20] applies a spectral sharpening transform to the sensory data in order to relax the gamut constraints. This method can be applied to algorithms using linear basis functions [49][95] as well. CRULE represents a significant advance in color constancy, but its assumptions about gamut mapping restrict it to matte Mondrian surfaces or controlled illumination; this is largely because uncontrolled conditions (or even specularity) can result in the reflected color being outside the limits of the gamut map defined for each surface without the help of a model of daylight. Ohta [63] assumes a known gamut of illuminants (indoor lighting following the CIE model), and uses multi-image correspondence to determine the specific

illuminant from the known set. By restricting the illumination, this method can only be applied to synthetic or highly constrained indoor images.

Another class of algorithms uses indirect measures of illumination. For instance, Shafer [80] and Klinker [43] use surface specularities (Sato [77] uses a similar principle, but not for color constancy), and Funt [27] uses inter-reflections to measure the illuminant. These methods assume a single point-source illuminant, which limits their application in outdoor contexts, since daylight is a composite, extended light source.

In yet another approach, D'Zmura [97] and Finlayson [21] assume multiple illuminants incident upon multiple instances of a single surface. The problem with these approaches is that they require identification of the same surface in two different parts of the image (i.e., multiple instances of a given set of surface characteristics) that are subject to different illuminants. Once again, the approaches have been shown to be effective only on Mondrian or similarly restricted images. In a variation of this approach, Finlayson [23] shows good results on a set of synthetic and real images by correlating image colors with the colors that can occur under each set of possible illuminants.

The final group of algorithms assume the presence of surfaces of known reflectance in the scene and then determine the illuminant. For instance, Land's Retinex algorithm [45] and its many variations rely, for accurate estimation, on the presence of a surface of maximal (white) reflectance within the scene. Similarly, Novak's supervised color constancy algorithm [61] requires surfaces of other known reflectances.

Funt [26][29] discusses the various approaches to color constancy in greater detail. The assumptions made by the aforementioned algorithms limit their application to restricted images under constrained lighting; certainly, few such methods have been

applied to relatively unconstrained outdoor images. It therefore makes sense to develop models for outdoor illumination and surface reflectance under outdoor conditions.

3.2.2 Parametric classification

The emergence of road-following as a machine vision application has spawned several methods for utilizing color to enable autonomous vehicles drive without specific parametric models. Crisman's SCARF road-following algorithm [16] approximates an "average" road color from samples, models the variation of the color of the road under daylight as a Gaussian distribution about an "average" road color, and classifies pixels based on minimum-distance likelihood. This technique was successfully applied to road-following, but cannot be applied for general color recognition, because the variation of the color of daylight according to the CIE model [42] cannot be modeled as Gaussian noise. At the same time, the notion of an "average" color for the entire gamut under changes of illumination and scene geometry may not be constrained enough for classifying pixels under specific conditions. One of the contributions of this dissertation is a definition of underlying models of illumination and reflectance, so that apparent object color under specific conditions can be localized to a point in color space with an associated Gaussian noise model for maximum-likelihood classification.

3.2.3 Techniques based on machine-learning

Pomerleau's ALVINN road-follower [73] uses color images of road scenes along with user-generated steering signals to train a neural network to follow road/lane markers. However, the ALVINN algorithm made no attempt to explicitly recognize the apparent color of lanes or roads, or to model reflectance.

Buluswar [10] demonstrates the use of machine-learning techniques for non-parametric pixel classification as an approach to color "recognition". Multivariate decision trees and neural networks are trained on samples of target and non-target "background" surfaces to estimate distributions in color space that represent the different apparent colors of the target surface under varying conditions; thereafter, image pixels are classified as target and background. This approach was shown to be very effective for color pixel classification in several outdoor applications. The problem with such non-parametric techniques is that their performance is determined entirely by the training data: if there is training data for the set of encountered illumination and viewing conditions and for non-target surfaces that can be expected in the images, then such techniques can approximate discriminant boundaries around them. In the absence of such data, however, the performance of non-parametric classification techniques in the "untrained" portions of color space is unpredictable. Funt [30] also approaches color constancy as a machine learning problem; as with other learning-based approaches, a potential issue with this technique is that the training data needs to represent the gamut of possible conditions that can occur, without which it is difficult to expect accurate performance.

3.2.4 Color segmentation

In the problem of segmentation, the goal is to separate spatial regions of an image on the basis of similarity within each region and distinction between different regions. Approaches to color-based segmentation range from empirical evaluation of various color spaces [64], to clustering in feature space [79], to physics-based modeling [51]. The essential difference between color segmentation and color recognition is that the former

uses color to separate objects without *a priori* knowledge about specific surfaces, while the latter attempts to recognize colors of known color characteristics. Although the two problems are, in some sense, the inverse of each other, results from segmentation can be useful in recognition; for instance, Maxwell [51] shows the advantages of using normalized color and separating color from brightness.

3.2.5 Color indexing

Swain [82] introduced the concept of color histograms for indexing objects in image databases, proving that color can be exploited as a useful feature for rapid detection. Unfortunately, this method does not address the issue of varying illumination, and hence cannot be applied to general color recognition in outdoor scenes. Funt [28] uses ratios of colors from neighboring locations, so as to extend Swain's method to be insensitive to illumination changes; unfortunately this method requires histograms of all the objects in the whole scene to vary proportionally.

3.3 Models of daylight

As Chapter 4 discussed, the CIE model [42] has been used to define the color of a few specific phases of daylight, and to parametrically model the overall variation of daylight color. This radiometric model has been confirmed by a number of other radiometric studies in various parts of the world [19][35][58][66], and has been used by several machine vision researchers [21][63] in digital images. Chapter 4 shows—in detail—that the CIE radiometric model cannot be applied to machine vision images because it does not account for (i) ambient light from a sufficiently large portion of the sky, and (ii) the effect of light reflected off the ground. In addition, the lack of context-specific data

makes the CIE model difficult to use in a wide range of conditions where the specific color of the incident light is required.

While the CIE model has been the most widely applied model in the context of color images, Sato [77] develops an intensity-based model in which sunlight is characterized as a "narrow Gaussian distribution" [77]. However, the model requires bright sunlight without any clouds, and does not account for the effect of a cloud cover or sun-obscuration (partial or full). Hence the applicability of Sato's model for color images with unconstrained sky conditions is unclear.

3.4 Surface reflectance models

In general, surface reflectance can be modeled by a bidirectional reflection distribution function (BRDF) [17][38][59], which describes how light from a given direction is reflected from a surface at a given orientation. Depending on the composition of the incident light and the characteristics of the surface, different spectra of light may be reflected at different orientations, thereby making the BRDF very complex.

The simplest model of reflectance is the Lambertian model [38], which predicts that light incident upon a surface is scattered equally in all directions, such that the total amount of light reflected is a function of the angle of incidence. The Lambertian model—and modifications thereof [65][93]—are used to describe reflectances of matte surfaces.

However, for modeling surfaces which have a specular component, a number of researchers use a composite of the specular and Lambertian components [15][43][46][56][77][80][87][97]. For instance, Shafer [80] models surface reflectance as a linear combination of the diffuse and specular components, and determines the

weights of each component from a measure of specularity. Shafer's Dichromatic Reflectance Model shows that color variation in *RGB* lies within a parallelogram, the length and breadth of which are determined by the two reflectance components. Klinker [43] refines the Dichromatic model by showing that surface reflectance follows a "dog-legged" ("⊥"-shaped) distribution in *RGB*, and then fits a convex polygon to separate the reflectance components. In a variation of Shafer's approach, Sato [78] uses temporally separated images to model the surface components. Each of these methods depends on the presence of pure specular reflection from a point-source light. As Chapter 4 will show, daylight is a composite, extended light source, not a point-source; consequently, none of the aforementioned approaches have been applied to outdoor images. Lee [46] derives the Neutral Interface Reflectance model which also models surface reflectance as a linear combination of the two reflectance components and demonstrates the effectiveness of his model on spectral power distributions of surfaces. Unfortunately, Lee stops short of applying his methods to real digital images. Sato [77] applies the Neutral Interface model and approximates sunlight as a "narrow" Gaussian (with a low standard deviation) to recover the shape of surfaces in outdoor digital images. In another approach to determining shape from shading, Nayar [56] uses photometric sampling (a method of sampling reflectance under varying viewing geometry) to model surface reflectance. While the methods developed by Nayar and Sato have been used for shape-extraction, neither has been used to model reflectance in color space. None of the aforementioned models have been used in the context of estimating apparent color in outdoor images; some of the above bear particular relevance to the Normalized

Photometric Function model developed in Chapter 5, and will be analyzed in greater detail there.

As the preceding discussion indicates, there is almost no work that attempts to estimate apparent color in realistic outdoor images (the one exception, Buluswar [10], classifies pixels without explicitly modeling or estimating apparent surface color). The goal of this dissertation is to adapt (and simplify) existing physics-based models and thereby develop a method applicable to outdoor images.

CHAPTER 4

A MODEL OF OUTDOOR COLOR

4.1 Overview

The first major contribution of this work is a detailed discussion of daylight color. Even though a standard model for the variation of daylight color (the CIE model [42]) exists, this section shows that the CIE model has three disadvantages that reduce its applicability to machine vision. First, the CIE radiometric equipment has a very small field-of-view (e.g., 0.5° and 1.5° [66]), in order to sample a small portion of the sky. On the other hand, when daylight is incident upon a surface, the FOV of the surface can be up to 180°, which means that there can be a significant amount of incident ambient light; the CIE model does not account for this ambient light. Secondly, in typical machine vision images, a significant amount of light is reflected off the ground, thus changing the composition of the light incident upon surfaces close to the ground; the CIE model does not account for such indirect light. Finally, there is very little context-specific information in the CIE model [14], which means that it is difficult to use the model to predict the color of daylight under specific conditions. As a consequence of these three issues, the CIE model cannot be used to estimate the apparent color of a surface, even if the illuminating conditions are specified. In order to deal with these problems, Section 4.4 develops a context-based model of daylight color that makes it possible to predict the color of the incident light under specific conditions (sun angle and cloud cover); this prediction is then combined with a reflectance model developed in Chapter 5.

4.2 The CIE daylight model

The CIE daylight model [42] is based on 622 radiometric measurements of daylight collected separately over several months in the U.S.A., Canada, and England [9][14][35]. Such radiometric measurements are typically made by aiming a narrow tube [14] with a very small field-of-view (e.g., 0.5° and 1.5° [66]) at a selected portion of the sky. The light going through the collection tube falls on a planar surface covered with barium sulphate (or a similar "white" material), and the spectral power distribution of the surface is recorded. In the CIE studies, careful precautions were taken so as to eliminate the effect of stray light—for instance, the data was collected on roof-tops, and all nearby walls and floors, and even the collection tube, were covered by black light-absorbent material [14].

The parametric model was then obtained by mapping the spectral power distributions of each of the 622 samples into the CIE chromaticity space, and then fitting the following parabola to the points:

$$y = 2.8x - 3.0x^2 - 0.275 \tag{4.1}$$

where $0.25 \leq x \leq 0.38$. In the *rgb* space (which is a linear transform of the chromaticity space [37]), the model is:

$$g = 0.866r - 0.831r^2 + 0.134 \tag{4.2}$$

where $0.19 \leq r \leq 0.51$. Figure 4.1 plots the daylight model in *rgb*; the figure also plots the CIE daylight model in the color circle. The regions of the function representing (approximately) sunlight and skylight (Figure 4.1(b)) have been determined empirically, based on radiometric measurements made by Condit [14] and the measurements shown in Table 4.1 (which is discussed later in this section).

For mathematical simplicity, the experiments that follow in later sections will approximate the CIE parabola by the following straight line, also shown in Figure 4.1(c):

$$g = 0.227 + 0.284\, r \tag{4.3}$$

which was determined by fitting a line to discrete points along the locus of the CIE parabola in *rgb*. The RMS error introduced by the linear approximation (determined by point-wise squared error for g-values generated for discrete r-values in the range $0.19 \leq r \leq 0.51$ at increments of 0.005) is 0.007. Figure 4.1(c) compares the linear and quadratic models.

4.3 Daylight in machine vision images

The goal of the CIE studies was to obtain the precise color of daylight under some specific conditions (e.g., noon in a clear sky, etc.). One of the motivations behind the studies appears to be the design of artificial light sources [42]. Hence, some canonical illumination conditions (such as noon sunlight and "average" daylight [42] were used as models for artificial light sources. In order to assure the accuracy of the measurements, high-precision radiometric equipment was used, and precautions were taken to prevent stray light from entering the experimental apparatus. In addition, only small portions of the sky were sampled by using the narrow collection tube.

Although these restrictions were required for the purposes of the radiometric studies, such conditions are not typical in outdoor computer vision images. As explained in Chapter 2, machine vision images are subject to a number of factors that can cause shifts in the color of the incident light. We collected samples of daylight under varying conditions from 224 color images of a calibrated matte white surface (Munsell number *N9/*), where the apparent color of the white surface is the color of the light incident upon

it. Figure 4.2 shows the sampling apparatus, along with samples of the color of daylight obtained from the set of 224 images, plotted in *rgb*. The exact set of illumination conditions sampled in these images is described in Table 4.1.

Figure 4.2(a) shows a board with a number of matte surfaces of different colors, mounted on a tripod which has angular markings at every 5°, along with accompanying adjustments on a rotatable head-mount. The surface in the middle of the board is the Munsell White, and is used to sample the incident light. During data collection, the angular markings on the tripod were used to vary the viewing geometry in the azimuth; images were taken at every 10°. The viewing geometry with respect to pitch was (approximately) fixed by maintaining a constant distance between the camera and the surface, as well as a constant camera height. For the measurements at each sampled sun-angle, the illumination geometry was also fixed with respect to pitch, but varied in the azimuth using the tripod angular settings. Using this procedure, it was determined that for almost[11] the whole 180° range where the sun is directly shining on the surface, the color of the incident daylight does not change with respect to varying relative viewing geometry. Similarly, as long as the surface is facing away from the sun, the color of the incident light is that of the skylight incident upon the surface. A total of 224 samples of daylight were collected under the illuminating conditions described in Table 4.1. The conditions were chosen so as to capture the maximum possible variation in the color of the light each day. In order to reduce the effect of pixel-level noise, the color of the white surface was sampled as the average over a 20 pixel × 20 pixel area. Figure 4.2(b) shows the data collected using the apparatus in Figure 4.2 (a), plotted against the linear

[11] At the extreme angles (e.g., near the -90° and 90° viewing angles), too little of the surface is visible for any meaningful analysis.

approximation of the CIE model. The root-mean-squared error[12] between the linear CIE model and the observed data was only 0.006. However, the Cartesian spread of our data was 0.162, about 46% of the spread of the CIE model, which is 0.353. In other words, our data covers only a portion of the full range of daylight color predicted by the CIE model, even though both studies sampled a similar range of sky conditions. In order to determine why the spread in CIE data is more than twice that in our data, the observations are divided into two groups: (i) those with an r value less than 0.33 (which, as discussed in Figure 4.1, represent samples of daylight from the direction away from the sun), and (ii) those with an r value greater than 0.33 (which represent samples from the direction of the sun).

[12] For every r value from the observed data (all of which were within the r range of the CIE model), a g value was calculated using the CIE model in Equation 4.2, and then compared to the corresponding g value in the observed data. Thereafter, the root-mean-squared error between the two sets of g values was calculated.

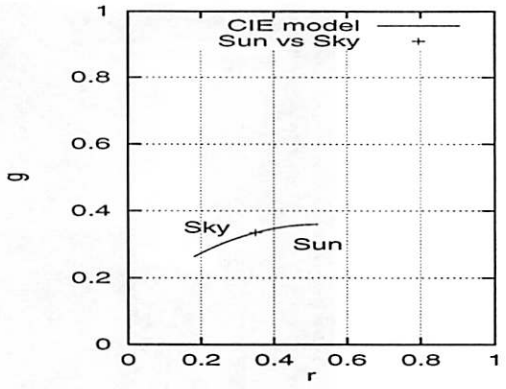

(a) rgb

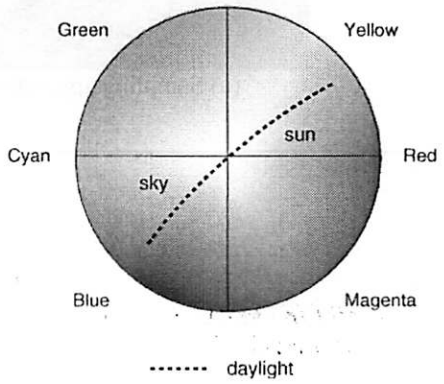

(b) Color circle

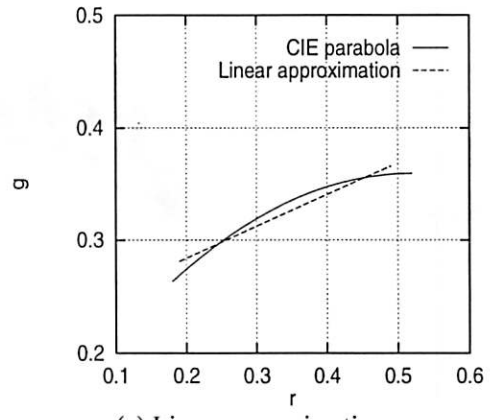

(c) Linear approximation

Figure 4.1. The CIE parametric model of daylight in (a) the *rgb* space and (b) the color circle. The sunlight and skylight components have been empirically determined to be on either side of the white point ([0.33, 0.33] in *rgb* and the center of the color circle). The CIE studies [42] describe the factors causing the variation. Figure (c) shows the linear approximation to the CIE parabola that this study uses for mathematical simplicity in later sections.

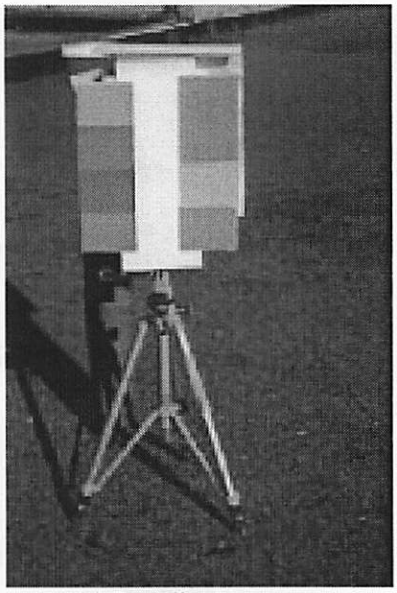

(a) Sampling apparatus

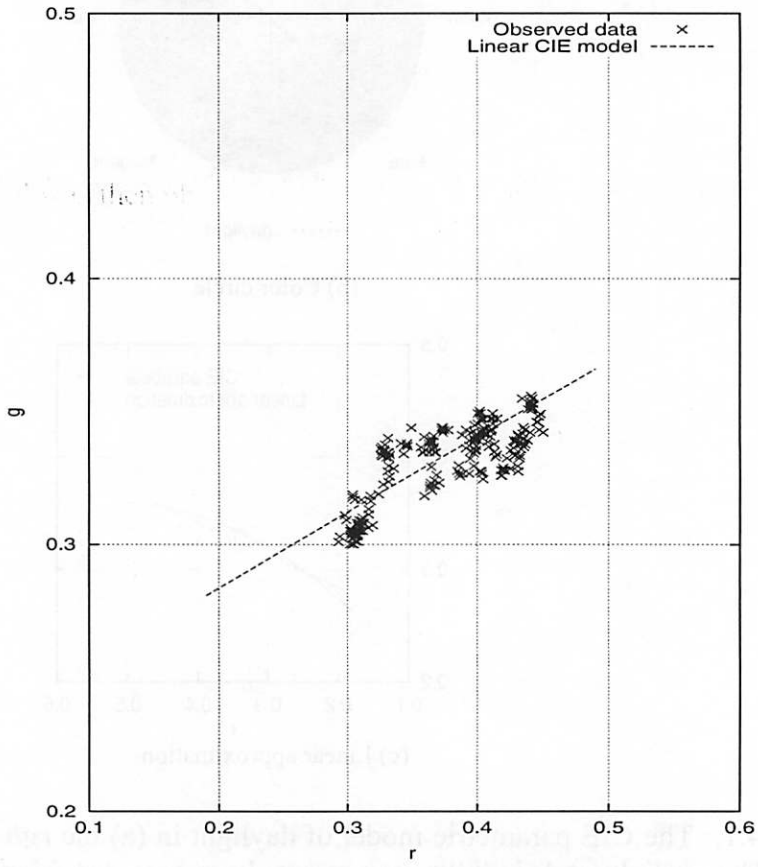

(b) Observed samples vs. CIE model

Figure 4.2. Samples of daylight color obtained from color images, compared to the CIE model. The white surface in the center of image in Figure (a) reflects the color of the incident light. These samples are plotted along with the linear approximation of the CIE model in Figure (b).

4.3.1 Incident light from the direction away from the sun

In the first group of samples, i.e., those with *r* values lower than 0.33, our samples (36 out of the 224 collected) stretched from [0.288, 0.302] to [0.326, 0.336], yielding a Cartesian spread of 0.051. On the other hand, the portion of the CIE function with *r* values below 0.33 stretches from [0.180, 0.264] to [0.320, 0.326], with a spread of 0.146. Since the spread is representative of the extent of variation in color, the data indicates that the variation in daylight according to our samples is about 35% of the variation according to the CIE model (for the samples with *r* values below 0.33). Perceptually, this means that the color of skylight is significantly "bluer" in the CIE model than in our data for the same range of sampled sky conditions [14].[13] The lowest *r* value according to the CIE function is 0.180, with a corresponding *g* value of 0.263. Since there is no documentation on the specific set of conditions that resulted in that particular sample in the CIE data, a comparable radiometric study [66] is used. That study recorded an *rgb* value of [0.180, 0.303] from a "cloudless sky at sunset" [66], from a portion of the sky in the opposite direction from the sun. For the same set of conditions, our data recorded an *rgb* value of [0.288, 0.302]. This discrepancy constitutes a Cartesian shift of 0.108 along the CIE linear function.

In addition to a clear sky with a setting sun, the color of the incident light from a direction away from the sun was sampled for two other conditions: a clear sky with the sun at 30°, and an overcast sky. For the clear sky, our data showed a value of [0.324, 0.334], whereas the CIE data [14] shows a value of [0.258, 0.313]; this corresponds to a

[13] Of all 622 CIE samples, the specific illumination conditions have been published for only 56 samples from Condit's study [14].

Cartesian shift of 0.069 along the CIE linear function. On the other hand, for the overcast sky, our measure was [0.357, 0.335], very close to the CIE measure of [0.360, 0.336].

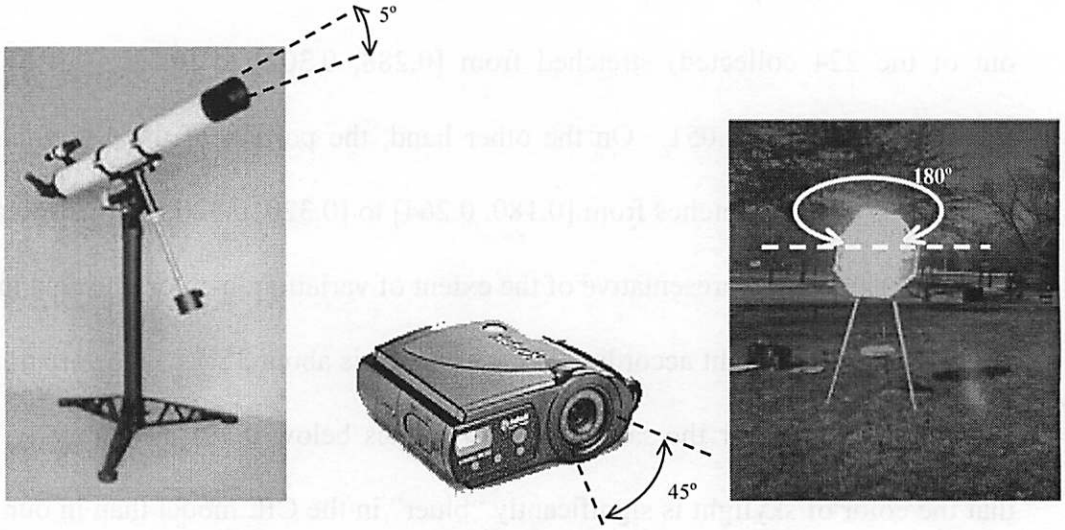

(a) Narrow FOV device (b) Wider FOV device (c) Planar surface with 180° FOV

Figure 4.3. Illustrative examples of devices/objects with different fields-of-view: (a) tube-like sensors/devices such as telescopes and photometers have narrow FOV's; (b) cameras have a wider FOV; (c) planar surfaces, on the other hand, have light incident from the full 180° "field-of-view". The implication of this phenomenon for outdoor images is that planar surfaces will have light incident upon it from a much larger portion of the sky than will the photo-receptor sensors of photometers (with collection tubes) or cameras.

The following discussion shows that when there is a discrepancy between the CIE model and our data, two factors account for the shift: (i) *ambient* skylight from *a large portion of the sky* (which is incident upon the surface because of the 180° FOV, and (ii) sunlight reflected off the ground. It is shown that the effect of ambient skylight accounts for about 75% of the shift, while the ground's reflection of sunlight accounts for about 20%. In the case of an overcast sky, there is very little variation in the color of the ambient skylight. At the same time, the sun is not visible, as a consequence of which the ground does not reflect the color of the sunlight.

4.3.1.1 The effect of ambient skylight

Figure 4.3 illustrates the significance of the field-of-view in outdoor images; the figure shows three objects: (a) a telescope (with dimensions representative of some photometeric tubes) with a narrow FOV (5°); (b) a camera with a wider FOV (45°), and (c) a planar surface, which has a 180° FOV. In the context of outdoor illumination, planar surfaces will have light incident upon it from a much larger portion of the sky. The field-of-view of the measuring devices used in the CIE radiometric studies was significantly smaller than that of the planar surfaces used for collecting our data; as a result, our samples include a greater effect of ambient light. For instance, in the radiometric study cited above [66], the field-of-view of the sampling device was 0.5° (horizontal) and 1.5° (vertical); on the other hand, the white sampling surface used in our apparatus has a field-of-view of practically 180°. The sampling surface is Lambertian, which means that its apparent color will be affected by light from every source in its field-of-view. As a consequence, while the radiometric equipment measures the color of light from a very small portion of the sky, our apparatus (which is far more representative of surfaces in machine vision images) measures the color of incident light from a very large portion of the sky—up to half the sky. This method is more suitable than the CIE apparatus for estimating the color of daylight incident upon flat surfaces.

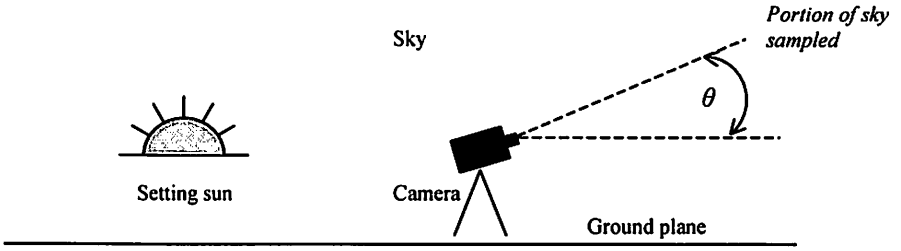

(a) Experimental setup for capturing direct images of the sky

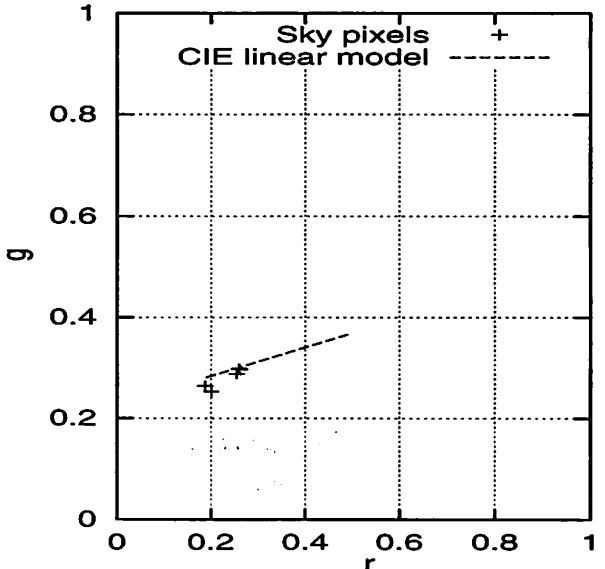

(b) Samples from different surface orientations

Figure 4.4. Samples of direct skylight color obtained from different portions of the sky: (a) experimental setup demonstrating how direct samples of the sky at different angles (with the camera facing away from the sun) were collected—samples were collected with the angle between the camera axis and the ground plane (θ) at 5°, 15°, 30°, 45° and 85°; (b) the samples plotted against the linearized CIE model. The data demonstrates that different portions of the sky can exhibit different colors.

The following discussion shows that different portions of the sky have different colors. To demonstrate this effect, we sampled five direct images of the sky using the setup illustrated in Figure 4.4(a). The images sampled direct skylight at five different angles (the angle θ between the camera axis and the ground plane): 5°, 15°, 30°, 45° and 85°. The samples were from the eastern portion of a clear sky, with the sun setting in the west—the same conditions reported in Parkkinen's radiometric study cited above [66].

From each image, pixels were extracted from 10×10 areas, and then averaged; Figure 4.4(b) shows the color of pixels from each of the five images, which were: [0.201, 0.253] at 5°, [0.188, 0.264] at 15°, [0.254, 0.288] at 30°, [0.261, 0.297] at 45°, and [0.259, 0.298] at 85°. Perceptually, the color of the sky was "bluest" at an angle of 15°, and less "blue" at lower and higher angles. In addition, the data shows that the color of the sky varies a great deal between 45° and 85°, which is the middle portion of the sky. The white surface was then sampled facing up, towards the sky (i.e., not vertical as shown in Figure 4.2(a), but *almost horizontal*, at an angle of approximately 5° in order to prevent direct incident sunlight). Since the surface is Lambertian, its apparent color will be a mixture of the light incident from all directions. The horizontal samples were taken on three different days under the aforementioned conditions. Each time, the *rgb* value of the surface was about [0.260, 0.299]. This means that when the surface faces up towards the sky (and there is no direct sunlight incident upon it) the color of the light incident upon it is dominated by the middle portion of the sky. Hence, it can be assumed that the "average" color of that half of the sky (under those conditions, i.e., clear sky with a setting sun), is [0.260, 0.299]. If this average is accepted as a better representative of the color of skylight than a sample from a small portion of the sky, then the color of skylight shifts along the CIE linear function by 0.08 (which is the distance between [0.260, 0.299] and [0.180, 0.303]). This shift is about 74% of the total discrepancy between our estimate of the color of the incident light and the radiometric measurement [66].

For the clear sky with the sun at 30°, the color of the incident light (with the surface standing vertically) was [0.324, 0.334], with the CIE measure for the same conditions being [0.258, 0.313]. Hence, the discrepancy was a Cartesian shift of 0.069 along the

CIE linear function. Direct measurements of the sky color (using pixels from a 10×10 area of the sky) were: [0.282, 0.303] at 5°, [0.256, 0.314] at 15°, [0.308, 0.326] at 30°, [0.311, 0.329] at 45°, and [0.310, 0.328] at 85°. The average color of the sky, as measured by the white surface facing up towards the sky (with no incident sunlight) was [0.309, 0.328]. The distance between the average color of the skylight and the CIE sample was 0.053. All three points lie on (or within two standard deviations of) the CIE linear function, meaning that the ambient light accounts for about 77% of the discrepancy between the CIE model and ours.

For the overcast sky, the color of the incident light (measured using the vertical sample) was [0.357, 0.335], very close the CIE measure of [0.360, 0.336]. This is because the color of the sky was uniform—direct measurements of the color of the sky were: [0.358, 0.336] at 5°; [0.354, 0.334] at 15°, [0.358, 0.335] at 30°, [0.355, 0.336] at 45°, and [0.357, 0.335] at 85°. The average color of the sky (from the surface facing up towards the sky) was [0.357, 0.335], which was, again, the color of the middle portion of the sky. The CIE estimate [14] was [0.360, 0.336], which is very similar to the average color of the sky. This is not surprising since there is very little variation across different portions of an overcast sky. Note that in this case, there is no sunlight reflected off the ground, either, which is another reason why there is no discrepancy between our data and the CIE data. Table 4.1 (which is discussed in detail later), lists the color of the incident light in the direction of the sun and away from the sun for a number of conditions. The color of the ambient skylight is listed for each of the conditions, and whenever the sky color is not overcast (i.e., when the sky is not uniformly colored), the ambient light accounts for about 75% of the discrepancy between the CIE data and ours.

4.3.1.2 The effect of ground reflection

While ambient skylight accounts for about 75% of the discrepancy between the radiometric studies and ours, another 20% is explained by the effect of reflectance off the ground. In our apparatus the white sampling surface is vertical, as a result of which the incident light is from the sky as well as from other objects in the scene. Of the scene objects, the one that is consistently the largest and closest to the sampling surface is the ground. Since the sampling surface is Lambertian, its apparent color will be a combination of light from all sources—in this case, the sky and the ground.

Figure 4.5(a) illustrates this phenomenon through four points:

1. The first sample (labeled "Skylight" in the figure) represents the average color of the sky (as measured by the surface oriented horizontally).
2. The second sample (labeled "Sunlight" in the figure) shows the color of the incident sunlight from the direction of the sun (as measured by the surface facing the sun).
3. The third sample (labeled "Ground" in the figure) shows the color of two types of concrete on which the apparatus rests. The color of these samples is the very similar to that of the incident sunlight, which is not surprising, since the concrete is gray and is illuminated by sunlight. The reader may recall that direct sunlight typically overcomes the effect of ambient light, as a result of which the color of the incident light is that of the incident sunlight.
4. Finally, the fourth sample (labeled "Incident light" in the figure) shows the color of the white surface oriented vertically. This sample represents the color of the effective incident light, and lies on the line connecting the two points representing

the color of the first point (i.e., the average color of the sky) and the second point (i.e., the color of the incident light from the direction of the sun).

The data suggests that the color of the light incident upon a vertical surface is a combination of the average skylight and the sunlight reflected off the ground. In order to account for the linear shift along the CIE linear function due to the effect of ground reflection, the three-dimensional world is modeled as a six-sided polyhedral box (see Figure 4.6). In this (admittedly crude) model, the white surface faces one side, with its back to another. When the surface faces away from the sun, the side of the box that is behind the surface represents the portion of the sky with the sun. Hence, light is incident upon the surface from five of the six sides. Of these five sides, four represent the sky and one side represents the ground. The linear shift is modeled as a weighted sum of the *brightness* of each side. The brightness of the ground depends on its own reflectivity, the brightness of the sunlight and the visibility of the sun (due to cloud cover, etc.). If the average brightness of the ground is represented by g, the ratio of ground brightness to sky brightness by G, and the sun visibility factor (which is described in Table 4.1 and Section 4.4) is represented by SV, then the effect of ground reflection can be determined from the expression: $(4\times G\times g + g\times SV)$ (which represents the distance between the average color of the sky and the color of the ground reflection).

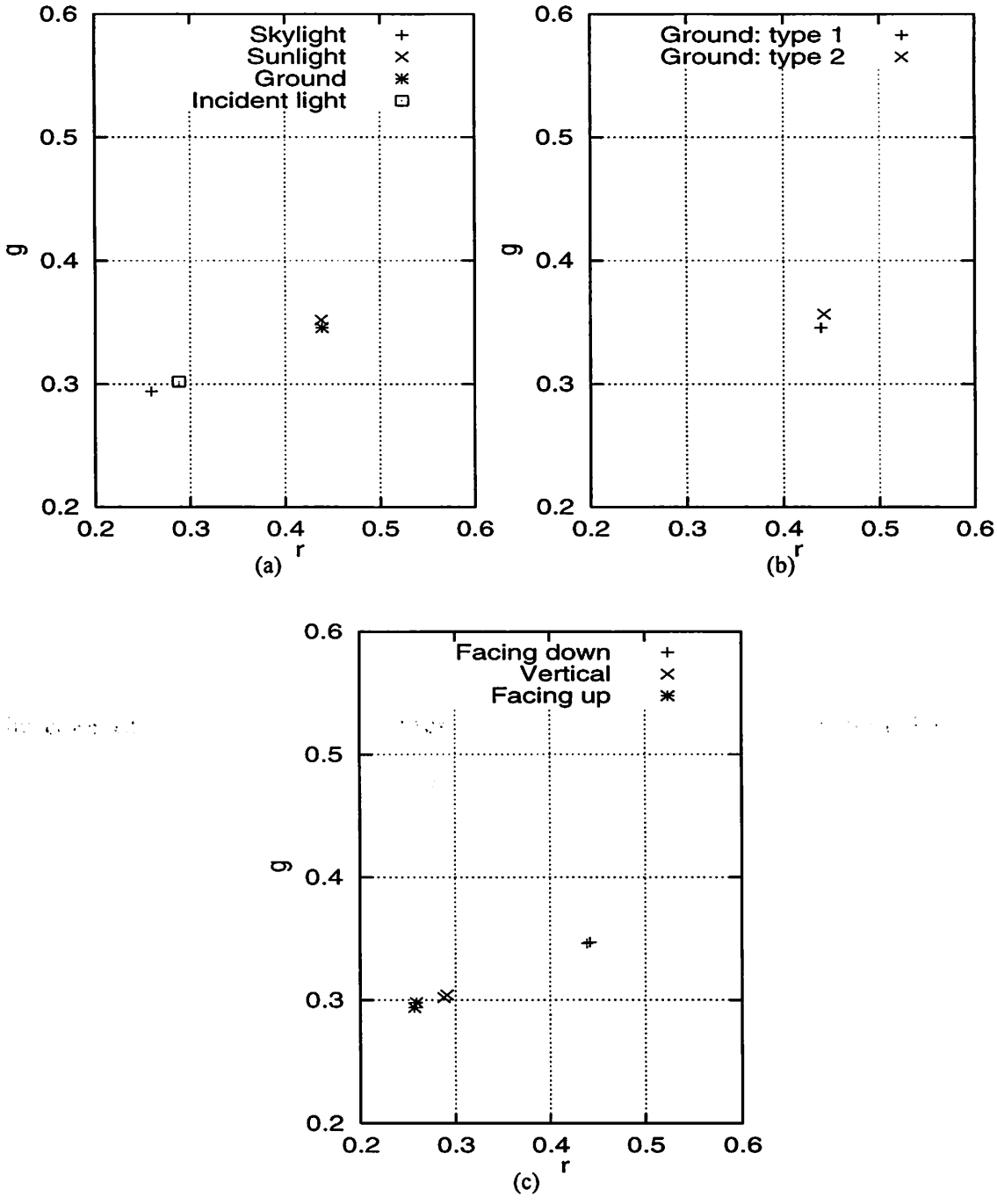

Figure 4.5. Samples of daylight color obtained from color images: (a) the color of skylight ("Skylight"), sunlight ("Sunlight"), the effective incident light ("Incident") measured using the white surface, along with a direct measurement of the "average" ground color ("Ground"); (b) direct samples of the "average" ground color (averaged over 30×30 regions), measured from two different locations; (c) samples of the white surface at different orientations (facing down, vertical, and facing up).

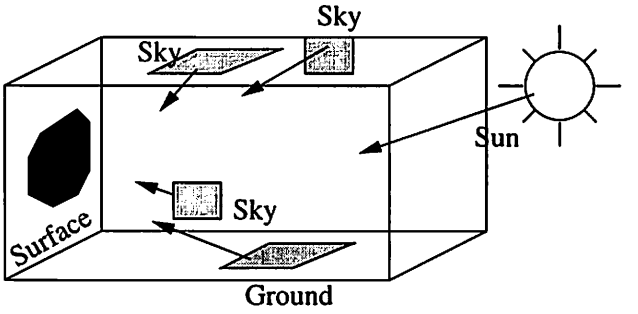

Figure 4.6. Six-sided polyhedral model showing light incident upon the surface from five directions: sunlight from one direction, ground reflection the bottom, and skylight from above and the sides.

In the samples described in Figure 4.4 and Figure 4.5 (i.e., with the setting sun in a clear sky), the sun visibility (SV) factor was 1, *average* brightness of the sky (measured over 30×30 portions of the image, as the average ((*R*+*G*+*B*)/3) was about 1.5 times the average brightness of the ground. Hence the polyhedral model evaluates to $(4\times1.5\times g + g\times1) = 7g$, meaning that the effect of ground reflection is $1/7^{th}$ of the effect of the skylight. Therefore, the linear shift is $1/7^{th}$ of the way between the color of the sky and the color of the ground. Using this method, the color of the incident light is estimated to be [0.284, 0.306]; as mentioned before, the observed color of the incident light (from the surface oriented vertically) was [0.288, 0.302]. The previous section showed that the effect of ambient skylight accounted for a shift of 0.08 along the CIE linear function, from [0.180, 0.303] to [0.260, 0.299], which was about 74% of the total discrepancy of 0.108. The effect of ground light accounts for a shift of 0.025 along the CIE linear function, which is about 23% of the total discrepancy. Therefore, the combined effects of ambient skylight and ground reflection—under this set of conditions—account for about 97% of the discrepancy between the CIE model and our observations.

Since ground reflectance affects the color of the incident light, the albedo of the ground must also be taken into account. The data collected in this study was on two types of ground surface: a concrete structure, and a lawn with dead, winter grass. The average (again, over a 30×30 region) color of the two types of ground were very similar, with both being the color of the incident light in the direction of the sun (see Figure 4.5(b)). Hence, a "gray-world" assumption about the ground was reasonable for our data, but may not be reasonable for all types of ground—for instance, if the images were taken in a field with bright green grass, the color of the ground reflection may be different. Another advantage of the polyhedral box model of the world is that it can accommodate the effect of miscellaneous scene objects on the color of the incident light, if their albedos and sizes are known.[14]

Finally, Figure 4.5(c) shows 7 samples of the white surface as its orientation changes from horizontal facing down to *almost*[15] horizontal facing up. The data shows that the apparent color of the surface (i.e., the color of the effective incident light) is one of three colors: (a) the 2 samples labeled "Facing down" represent the color of the sunlight (when the surface faces the ground, so that no skylight is incident upon it), (b) 3 more samples, labeled "Vertical" represent the combination of skylight and sunlight, taken with the surface oriented such that both skylight and ground-reflection are incident (with surface orientation at 60°, 90° and 120° with respect to the ground plane), and (c) the remaining 2 samples (labeled "Facing up") represent the apparent color of the surface when only skylight, but no ground-reflection is incident (in other words, these last 2 samples represent the color of skylight). This means that even if a surface is not exactly vertical,

[14] For instance, Gershon's approach [31] can take advantage of this model.
[15] Again, the surface is *almost* horizontal so that there is no sunlight incident upon it.

its effective incident light is the same combination of ambient skylight and ground reflection for a wide range of angles, as long as both sources are in the field-of-view of the surface.

The reader may recall that earlier discussions (in Section 4.3.1.1) explaining the discrepancy between the linear CIE model and our data were based on samples under a clear sky with the sun at 30°. Under those conditions, it was determined that the ground color (sampled by the white surface facing down) was [0.372, 0.335]. Applying the polyhedral box model of daylight to 9 of our samples, the estimated linear shift due to ground reflection was determined to be about 0.013, which is about 19% of the total discrepancy (which, as shown earlier, was 0.69).

For the overcast sky, there was no statistically significant discrepancy between the CIE model and our data. In the previous section, it was shown that the color of the ambient skylight under those conditions was uniform. Since the sun was completely occluded by clouds, the ground reflection was the color of the ambient light—[0.358, 0.335]. Note that since the sun visibility factor for an overcast sky is 0, the polyhedral model suggests that there will be no shift from the average color of the sky (in other words, the incident light will be the color of the sky, unaffected by ground reflection).

4.3.2 Incident light in the direction of the sun

The color of the incident light in the direction of the sun is not affected by ambient skylight or ground reflectance. When the white surface is sampled at various orientations between vertical and horizontal (facing the sky), the *rgb* color of the surface is exactly the same ([0.436, 0.349]). The reason the color of the incident sunlight is not "diluted" is that sunlight is significantly (about 4 or 5 times, as observed in the data) brighter than the

ambient skylight. Consequently, the effect of ambient skylight is negligible. This hypothesis is also supported by the fact that only about 1% of the CIE samples have an *r* value greater than the samples in our study—meaning that in the direction of the sun, our data is very consistent with the CIE data[16].

As a model of incident light color, with respect to specific sun-angle and sky conditions, the CIE data does not account for ground reflection or the effect of ambient light from a large portion of the sky. Any object in machine vision images will be affected by one or both of these phenomena, which means that the color of the incident light in vision images is likely to be significantly different from the predictions of the CIE model. Hence, the CIE model may lead to incorrect estimations of apparent color, and may therefore be inappropriate for vision applications.

4.4 Daylight color indexed by context

As stated previously, the color of the incident daylight depends on the sun-angle, sun visibility, cloud cover, miscellaneous atmospheric particulate matter, and illumination geometry. Hence, this study develops a context-based table of daylight color, in the direction of the sun and away from the sun, indexed by the sun-angle (elevation), cloud cover and sun visibility. The source data is the same as that shown in the distribution in Figure 4.2. The sun-angle is the vertical rise of the sun, and can be calculated from a standard astronomical equation, given the location (latitude and longitude) and time-of-day [53]. In addition to using the equation, the sun-angle was confirmed through

[16] The reader may recall (from Section 4.3.1) that the CIE samples in the direction away from the sun were perceptually "bluer" than ours. Since higher *r* values occur in samples facing *towards* the sun, the negligible discrepancy (between the CIE data and ours) among the samples with high *r* values suggests that the CIE measurements of light in the direction of the sun are perceptually *not* "redder" than ours.

physical measurements with a protractor on the ground plane. The cloud cover is an approximate measure of the percentage of the sky covered by clouds. The sun-visibility factor, scaled from 0 to 1 is an approximate measure of the clarity of the sun. For instance, if the sun is completely covered by a dark cloud, the visibility factor is 0; similarly, if the sun is completely visible, the factor is 1, and if the sun is behind a thin cloud but still perceptible, the factor may be about 0.5. Another way of determining the sun-visibility factor is from the sharpness of shadows—the sharper the shadows, the higher the visibility factor[17].

The table lists, for varying values of each of these conditions, the average *rgb* and brightness from the direction of the sun rgb_{sun} and V_{sun}, and away from the sun (rgb_{away} and V_{away}).[18] The standard deviations for each of these measurements are also shown (in the columns marked σ), along with the number of samples (#) taken. Note that the standard deviations for the brightness values are too high to accurately predict the brightness of daylight under a given set of conditions. Finally, the last column of the table lists the average sky color (rgb_{sky}, measured with the white surface facing up towards the sky; the standard deviation of rgb_{sky} across all the samples was about 0.004. The data in Table 4.1 was collected at three locations in the U.S.—rural Massachusetts, suburban Detroit, and suburban Chicago—in 1995, 1996 and 1997, respectively. Each of the years, at each of the locations, the data was collected over six months: September through February. Hence, this data does not account for possible variations due to

[17] The sun-visibility factor affects the nature of the incident light in two ways: (1) It affects the color of the incident sunlight; (2) It affects specular reflectance—this effect is described later. It may be possible to measure the sharpness of shadows by gradient-detection techniques.

[18] The measurement of brightness values in digital cameras depends on the gain-setting. For the data in these samples, the CCD gain was fixed at 2.0 e-/count. Details of the effect of the gain control can be found in camera users' manuals or other reference books [40].

seasonal factors (such as summer haze, etc.). In addition, the effect of smog is uncertain, and the applicability of the model to areas with significantly different levels of smog or haze is not clear [36].

It is difficult to compare the data in this table to the (small amount of) context-based information in the Condit's data [14], because the radiometric measurements appear to have a much greater variance among entries representing similar conditions. For example, at a sun-angle of 30° on a clear day, the standard deviation in Condit's measurements of incident light in the direction of the sun is about 0.020 in *rgb* (corresponding to an 800°K difference in color temperature); the standard deviation for the same conditions in Table 4.1 is 0.008. Although there are no explicitly stated reasons for the variation in the radiometric measurements,[19] it presumably stems from the fact that the radiometric studies are (by design) sensitive to small changes in many of the factors described in Chapter 2. Our data, on the other hand, is insensitive to small variations in the scene, largely due to the larger field-of-view of the sampling white surface.

[19] In fact Condit refers to these variations as being "surprising" [14].

Sun Angle	Cloud %	Sun visibility	rgb_{sun}	$\sigma_{r\text{-}sun}$	V_{sun}	$\sigma_{v\text{-}sun}$	rgb_{away}	$\sigma_{r\text{-}away}$	V_{away}	$\sigma_{v\text{-}away}$	#	rgb_{sky}
0-5	0-20	1	.436 .349	.006	195	24	.288 .302	.009	53	29	8	.260 .299
0-5	21-50	1	.436 .349	.006	186	31	.296 .312	.012	48	33	9	.277 .302
0-5	51-70	0.5	.406 .344	.008	158	36	.319 .315	.009	56	38	11	.349 .331
0-5	71-100	0	.352 .335	.005	41	22	.352 .335	.008	41	26	10	.355 .336
6-15	0-20	1	.394 .330	.008	206	31	.288 .302	.010	58	34	6	.274 .305
6-15	21-50	1	.394 .340	.009	198	38	.296 .312	.009	41	40	6	.296 .314
6-15	51-70	0.5	.368 .334	.010	167	29	.319 .315	.012	41	32	7	.331 .330
6-15	71-100	0	.352 .335	.008	44	21	.352 .335	.007	36	24	6	.352 .338
16-25	0-20	1	.385 .337	.008	221	28	.323 .334	.008	51	34	11	.301 .313
16-25	21-50	1	.385 .337	.007	215	26	.323 .334	.013	51	26	7	.334 .323
16-25	51-70	0.5	.376 .337	.011	188	30	.326 .336	.012	58	32	4	.337 .329
16-25	71-100	0	.352 .335	.008	50	21	.352 .335	.009	48	25	4	.357 .335
26-50	0-20	1	.370 .332	.008	224	33	.323 .334	.009	56	35	9	.309 .328
26-50	21-50	1	.370 .332	.007	220	29	.323 .334	.011	69	35	8	.333 .332
26-50	51-70	0.5	.359 .337	.006	176	28	.326 .336	.010	51	31	4	.347 .334
26-50	71-100	0	.352 .335	.008	64	24	.352 .335	.008	68	29	9	.354 .336
51-70	0-20	1	.350 .335	.007	249	36	.323 .334	.010	71	38	3	.312 .330
51-70	21-50	1	.350 .335	.009	249	35	.323 .334	.013	60	37	5	.333 .332
51-70	51-70	0.5	.359 .332	.010	170	37	.326 .336	.010	43	37	9	.341 .332
51-70	71-100	0	.352 .335	.008	52	22	.352 .335	.008	51	25	8	.352 .335

Table 4.1. Context-based illumination model, showing and the *rgb* and brightness (*V*) values for the incident light in the direction of the sun (rgb_{sun}, V_{sun}) and away from the sun (rgb_{away}, $V_a\ rgb_{away}$), for various conditions, along with the corresponding standard deviations and the number of samples (#). The conditions are indexed by the sun angle, the cloud cover (*Cloud %*) and the sun visibility factor. The last column shows the average color of the sky (rgb_{sky}), measured with the white surface facing up, towards the sky.

CHAPTER 5

A SURFACE REFLECTANCE MODEL: THE NPF

5.1 Overview

The second model developed in this study is the Normalized Photometric Function, a reflectance model that is a simplified form of existing models [80] for use in outdoor color images, and in particular with the daylight model from the previous chapter. Several physics-based reflectance models exist, most notably Shafer's Dichromatic model [80], Nayar's hybrid reflectance model [56], and Phong's shading model [70], but these models make three assumptions that are not suitable for outdoor images. First, they assume single-source illumination, whereas daylight is a composite illuminant; second, they require brightness values, and the previous sections showed that the brightness of daylight is difficult to model; finally, the three models assume that specular surfaces always demonstrate the characteristic specular effect (the "spike"), which may not be true if the illuminant is an extended source. This chapter discusses the existing models, and then derives the Normalized Photometric Function (NPF) through modifications and simplifications to the existing models, for use in outdoor images. A photometric function typically plots the *brightness* of the light reflected off a surface as a function of the viewing angle; the NPF, however, plots the *relative change in normalized color* of a surface as the viewing angle changes.

5.2 Existing physics-based models

The Dichromatic Reflectance Model [43][80] represents the intensity of reflected light (radiance) L, at wavelength λ for a surface at incident angle i, viewing angle e, and phase angle g as:

$$L(\lambda,i,e,g) = m_s(i,e,g)\, c_s(\lambda) + m_b(i,e,g)\, c_b(\lambda) \tag{5.1}$$

where $c_s(\lambda)$ and $c_b(\lambda)$ are the albedos at wavelength λ for the specular and Lambertian components, respectively; c_s and c_b are constant for a given surface, and are dependent only on wavelength—not the illumination or viewing angles. The illumination and viewing angles determine the geometric scale factors $m_s(i,e,g)$ and $m_b(i,e,g)$, such that $(0 \le m_s,\ m_b \le 1)$. The Dichromatic model shows that most of the (i, e, g) combinations will result in reflectance that is dominated by the Lambertian component, i.e., $m_s = 0$, and $m_b = 1$. For the remaining angles, depending on the specularity of the surface, $(0 \le m_s,\ m_b \le 1)$. The points from each of the two components are represented as two linear clusters in a spectral histogram, which together form a skewed "⊥" in a parallelogram representing the dichromatic plane in *RGB* space (see Figure 5.1).

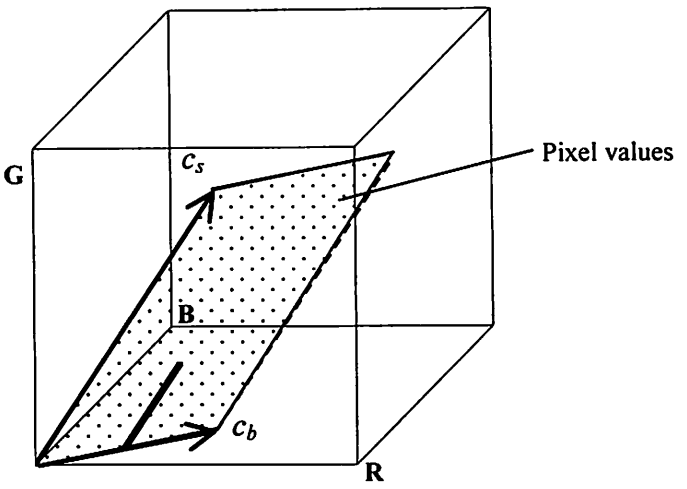

Figure 5.1. The Dichromatic Model [43][80] describes reflectance in RGB space as a skewed "⊥"-shaped cluster within a parallelogram that represents the dichromatic plane.

According to the Phong shading model [70] (adapted for computer vision by Horn [39]), the brightness of reflectance (L) at incidence angle i, viewing angle e, and relative viewing angle n (the angle between the directions of viewing and maximal specular reflection) is:

$$L(i,e,n) = t\frac{n+1}{2}\cos^{\alpha}(n) + (1-t)\cos(i) \qquad (5.2)$$

where t and α are parameters of the material; t represents the total amount of light reflected by the specular component, and α represents the clustering of reflection of the specular component about the angle of reflection. In this model the falloff in the brightness of specular reflection is a function of $\cos^{\alpha}(n)$, and the weights for the two components are t and $(1-t)$. The value of α is determined empirically for a given surface, and varies from 1 (for matte surfaces) to 200 (for highly specular surfaces). At (n= 0), the brightness is maximal (i.e., 1), and falls off as the surface is rotated, to the minimum (i.e., 0) at –90° and 90°.

Finally, according to Nayar's hybrid reflectance model [56], the total intensity I at a given point on the surface is modeled by:

$$I = A\cos(\theta_s - \theta_n) + B\,\delta\,(\theta_s - 2\theta_n) \tag{5.3}$$

where A and B are the weights of the Lambertian and specular components, respectively, and θ_s and θ_n are the angle of incidence and the direction of the surface normal.

The three models have three characteristics in common:

1. They model reflectance as a weighted linear combination of the Lambertian and specular components.
2. The Lambertian component (also called "body reflection') is modeled according to Lambert's Law [38].
3. All three models deal with the brightness values across the visual spectrum, which can then be represented in RGB as the brightness along each of the three dimensions.

The NPF similarly models reflectance as a linear combination of the Lambertian and specular components, also using Lambert's law. On the other hand, the NPF models reflectance in normalized color space (*rgb*) for compatibility with the daylight model in Table 4.1, which is accurate only for *rgb* values. In addition, the incidence angle changes across non-planar surfaces, thereby creating a variation in the brightness of the Lambertian component at different portions of a surface [38]; however, the *rgb* color of the Lambertian component surface does not vary due to a change in the incidence angle

(as long as the illuminant color does not change).[20] As a result, the NPF model can easily be applied to non-planar surfaces.

There are also three notable differences between the three models:

- The Phong model assumes that the weights of the two components are dependent (t and $(1-t)$); as described by Horn [39], this is because if an amount t of the incident light in reflected by the specular component of the surface, the remainder of the light (which is $(1-t)$) penetrates to the "body" of the surface[21] and exhibits Lambertian reflectance. On the other hand, Shafer and Nayar do not explicitly assume dependency between the coefficients of the two components.
- The brightness falloff models for the specular component are different: Nayar uses the delta function [57], Phong uses $cos^{\alpha}n$, and Shafer does not specify the specular falloff function.
- Phong and Nayar, unlike Shafer, develop a photometric function.

Because it predicts reflectance in normalized color space, the NPF assumes that the sum of the weights of the two components is 1. It is then shown that based on a simplification of the Dichromatic model, the composite falloff function, i.e., the transition between the color of the Lambertian component and the color of the specular component (as the surface orientation changes) is along a straight line in *rgb* color space. Based on the straight line, a piecewise-linear photometric function is empirically derived, mapping

[20] Note that the NPF ignores the effect of intensity, separating surface intensity from normalized color; however, one of the pixel classification techniques described in Chapter 6 explicitly uses intensity constraints.

[21] Phong describes specularity as light reflecting off a thin, smooth outer layer of a surface, and Lambertian reflection as resulting from penetration of light through the outer layer to the rougher "body" of the surface.

the relative viewing angle (which is the angle between the directions of viewing and maximal specular reflection) to the relative change in the weights of the two components.

As described earlier, there are three reasons the aforementioned three physics-based models are difficult to use—in their current form—for color recognition in outdoor images. First, all three models assume a single-source illuminant (either point or extended).[22] The second reason is with regard to m_s (to use the terminology of the Dichromatic Model), the scale factor of the specular component. In the physics-based models, m_s is modeled either as an impulse function of i and e [46][56] or as a power of $cos(n)$ [70]. Intuitively, this means that all surfaces with $(c_s(\lambda) > 0)$ (i.e., all surfaces with a specular component) will exhibit the specular "spike", which is modeled by $m_s(i,e,g)$. Under daylight, the specular effect is apparent only under bright sunlight, but is diminished or absent under only skylight or under an overcast sky. Hence, the effect of the illuminant (i.e., the presence, obscuration of, or absence of the sun) on the specular component must also be taken into account. The third reason the existing models need to be modified is that all three reflectance models deal with *intensity* values, which are independently calculated for each of the R, G, and B primaries when applied to color. The CIE daylight model and the model in Table 4.1 explicitly avoid intensity-based modeling, because the intensity of incident daylight is difficult to precisely model. In addition, as mentioned before, the brightness of the Lambertian component varies over the area of non-planar surfaces; this means that using a non-normalized space would

[22] Sato [77] adapts a general weighted linear reflectance model for shape recovery under daylight, and applies it to shape recovery by modeling sunlight as a "narrow Gaussian distribution". In that model, $L_{sun}(\theta_i-\theta_s) = A\ exp\ (-(\theta_i-\theta_s)^2/(\sigma^2))$, where L_{sun} is the intensity of sunlight with incidence angle θ_i and reflecting angle s. The term σ represents the standard deviation of the distribution, and A is an empirical parameter. However, the model requires bright sunlight without any clouds, and does not account for the effect of a cloud cover or sun-obscuration (partial or full).

require knowledge of the surface normal at every point on the surface. On the other hand, he normalized *rgb* color does not change due to a change in the incidence angle under a given illuminant. Hence, although these reflectance models have been used successfully for problems such as shape-from-shading (Nayar) and estimation of reflectance and illumination parameters (Shafer), and for rendering synthetic images (Phong), they have to be modified for use in outdoor images with a model of daylight.

5.3 Derivation of the NPF

As mentioned earlier, the NPF combines aspects of the three physics-based models, so that it can be applied to a model of daylight such as the one in Table 4.1. To begin with, the NPF separates the effect of intensity from that of normalized color. The NPF can be derived from the Dichromatic Model, which does not explicitly assume that the coefficients of the two components are dependent. In the Dichromatic Model, the condition ($0 \leq m_s, m_b \leq 1$) is true, but the condition ($m_s + m_b = 1$) is *not* assumed to be true; in other words, the model assumes that the scale factors of the two components are mutually independent. With the exception of some surfaces (such as fluorescent paints and certain metals [32]), specular surfaces typically reflect back the color of the illuminant, with a uniform albedo; hence, $c_s(\lambda) = 1$.

In addition, it can be shown that for normalized color, the condition ($m_s + m_b = 1$) is valid.[23] According to the weighted-combination reflectance models, in *RGB*, $R_a = W_l R_l + W_s R_s$, $G_a = W_l G_l + W_s G_s$, and $B_a = W_l B_l + W_s B_s$, where R_a, G_a and B_a are the apparent colors of the surface, R_l is the albedo of the red component Lambertian, W_l the weight of

[23] Note that this assumption is made in the intensity-based models derived by Phong [70] and Horn [39].

the Lambertian component, and so on. In *rgb*, $r = R/(R+G+B)$. Hence, $r_a = W_l \frac{R_l}{R_l + G_l + B_l} + W_s \frac{R_s}{R_s + G_s + B_s}$. If the two weighted components are multiplied by some constant A (representing intensity), then R, G and B all become multiples of A, thus leaving the ratio $[R:G:B]$ unchanged. Hence, multiplying the components by a constant does not alter r_a, g_a, or b_a. Since the constants do not affect the apparent normalized color, the ratio of the weights are what matter, not their absolute values. This means that the weights are not independent. Hence, if both components were multiplied by the expression $(1/W_l)$, W_l would be replaced by 1, and W_s by (W_l/W_s). By the same token, the sum of the weights, W_l+W_s, can be set to a constant; when that constant represents maximal reflectance, the constant can be set to 1, with sub-maximal reflectance represented by fractions between 0 and 1. Hence, it can be assumed that the condition $(W_l + W_s = 1)$ is valid.

Physically, if the specular component reflects the color of the illuminant, then a pure specular surface with m_s=1 and m_b=0 will be the color of the illuminant. As the weight of Lambertian component increases (with a change in the viewing angle), the apparent color of the surface tends away from the color of the illuminant towards the color of the Lambertian component. Hence, m_s decreases as m_b increases. In the extreme, if the surface is Lambertian, m_s=0 and m_b=1, and the apparent color of the surface is the apparent color of the Lambertian component. This observation, also made by Horn [39], makes $(m_s + m_b = 1)$.

Therefore, in *rgb* the Dichromatic Model can be simplified to:

$$L(\lambda,i,e,g) = (1-m_b(i,e,g)) + m_b(i,e,g)\, c_b(\lambda)$$

Note that (as explained earlier in this section) the expression $c_s(\lambda)$ is eliminated from the model because the specular component reflects back the color of the illuminant, meaning that $c_s(\lambda) = 1$. Further, the Dichromatic Model uses the phase angle g as a third angular parameter, in addition to the incidence angle i and the viewing angle e. According to the Lambertian model [38], the brightness—not the normalized color—is a function of the phase angle. Hence, g can be simplified as the sum of i and e. Finally, by expressing the combination of i and e as the relative viewing angle n, i.e., the difference between the viewing angle and the angle of maximal specularity (as in the Phong model), the Dichromatic Model can be normalized to:

$$L(\lambda,n) = (1-m_b(n)) + m_b(n)\, c_b(\lambda) \tag{5.4}$$

In Equation 5.4 the Lambertian component is defined in the wavelength space. According to the Lambertian model, the energy reflected at a given wavelength λ is measured as the product of the incident light and the surface albedo [38]:

$$\rho(\lambda) = \iota(\lambda)\, cos(\theta_i)\, \sigma(\lambda) \tag{5.5}$$

where $\rho(\lambda)$ and $\iota(\lambda)$ denote the intensity of the reflected and incident light at wavelength λ, respectively, θ_i is the angle of incidence, and $\sigma(\lambda)$ is the surface albedo for light at wavelength λ. In a normalized color space, the brightness component of the Lambertian model is eliminated. Hence, the cosine factor in Equation 5.5 is dropped:

$$\rho(\lambda) = \iota(\lambda)\, \sigma(\lambda) \tag{5.6}$$

Equation 5.6, which uses the continuous wavelength space, can be reduced to the three-dimensional *rgb* space by using a set of three camera/digitizer filters (which, the reader may recall, are linear transforms of the CIE tristimulus functions [32], but need to be calibrated for each individual camera), and then normalizing over intensity, to get:

$$r = \int E(\lambda)\bar{r}(\lambda)d\lambda$$
$$g = \int E(\lambda)\bar{g}(\lambda)d\lambda$$
$$b = \int E(\lambda)\bar{b}(\lambda)d\lambda \qquad (5.7)$$

where r, g and b are the normalized color values derived from applying the filters $\bar{r}$, $\bar{g}$ and $\bar{b}$ to the spectral power distribution of the incident light (E) at wavelength λ. Equation 5.8 shows a discrete (three-dimensional) approximation of a continuous function (in wavelength space). By applying this approximation to the wavelength-space model from Equation 5.7, the Lambertian color-coefficient model [68] is derived as:

$$r = r_i * W_{rr} + g_i * W_{rg} + b_i * W_{rb}$$
$$g = r_i * W_{gr} + g_i * W_{gg} + b_i * W_{gb}$$
$$b = r_i * W_{br} + g_i * W_{bg} + b_i * W_{bb} \qquad (5.8)$$

where r_i, g_i and b_i represent the color of the incident light, and W_{rr}, W_{rg} and W_{rb} are the color coefficients (albedo) of the red component of the surface under the red, green and blue bands of the illuminant, respectively; the expressions associated g and b are analogous. According to this model, the apparent color of a Lambertian surface (or the Lambertian component of a surface) constitutes a linear transform of the incident light, the coefficients of which are determined by the spectral reflectance of the surface. The nine weights can be determined from a total of three images each under different illuminating conditions (the three images constitute a total of nine equations for determining the coefficients, three each of r, g, and b). Note that the off-diagonal terms in the matrix are non-zero due to the overlap in the tristimulus functions [32].[24] The color-coefficient model makes the assumption that camera response is linear, i.e., that the response along each of the three bands remains the same for all brightness values. As

[24] Finlayson [22] shows that in some special cases, the off-diagonal terms are zero.

discussed in Chapter 2, the response function for cameras can be nonlinear, and is a function of the gamma-correction (γ) factor. For each of the bands, the output signal o is determined by ($o = i^{\gamma}$), where i is the strength of the input signal on the digitizer, and γ, the gamma-correction factor. Fortunately, it is not difficult to linearize the response [60] (for some cameras, it is possible to simply disable the gamma-correction). For the data collected for this study, the camera f-stop was adjusted so as to restrict the response to a very small range in the middle, approximately linear portion of the response function.

In matrix notation, the color-coefficient model is represented as:

$$\begin{bmatrix} r \\ g \\ b \end{bmatrix} = \begin{bmatrix} W_{rr} & W_{rg} & W_{rb} \\ W_{gr} & W_{gg} & W_{gb} \\ W_{br} & W_{gb} & W_{bb} \end{bmatrix} \begin{bmatrix} r_i \\ g_i \\ b_i \end{bmatrix} \tag{5.9}$$

Earlier, in Equation 5.4, the Lambertian component was represented by $m_b(n)c_b(\gamma)$, which is the wavelength form of the color-coefficient model shown in Equation 5.9, above. In the normalized *rgb* space, the apparent color of this component is a single point determined by applying the color-coefficient matrix to the normalized color of the illuminant. The specular component, represented in Equation 5.4 simply as $(1\text{-}m_b(n))$, is an offset from the point (in the direction of the illuminant *rgb* color) that represents the apparent normalized color of the Lambertian component; Figure 5.2 shows this phenomenon.

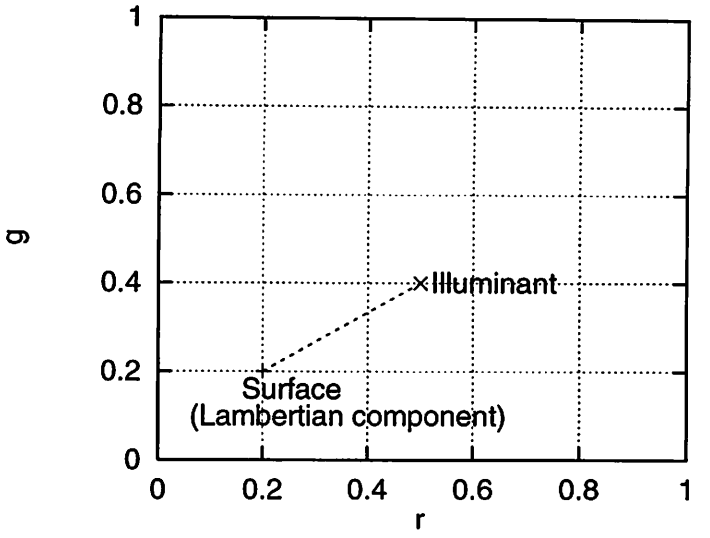

Figure 5.2. The Dichromatic Reflectance model in normalized color space. The apparent color of the surface is a point on the line between the points representing the colors of the illuminant and the Lambertian component of the surface under that illuminant.

This means that in *rgb* (as in the *RGB* and wavelength spaces), surface reflectance can be modeled as a weighted combination of the Lambertian and specular components. In *rgb*, however, the two reflectance components are represented by two points, rather than the two lines of the skewed "⊥" in the Dichromatic model (see Figure 5.1); one of these two points represents the illuminant, and the other represents the apparent color of the Lambertian component under that illuminant. Note that the illuminant point also represents the apparent color of the pure specular component, because under pure specular reflectance, the apparent normalized color of the surface is that of the illuminant. The variation in apparent color of a surface due to varying orientation is represented by the line connecting the two points. The apparent color of a surface for a particular combination of illumination geometry and viewing geometry (i.e., the relative viewing geometry) depends on the relative strengths of the specular and Lambertian components, and is represented by a point along the line connecting the two "pure" points (Figure 5.2). This observation is supported in radiometric studies done by Lee [46], which show that in

the CIE chromaticity space, the reflectance of various surfaces form straight lines which converge at the point representing the illuminant.

Applying Equation 5.4 to the tristimulus functions shown in Equation 5.7 and to the color-coefficient model in Equations 5.8 and 5.9:

$$A(n) = C + [I\text{-}C]*\rho \tag{5.10}$$

where A is the apparent *rgb* color (vector) of a surface at a relative viewing angle n, under illuminant color (vector) I, with a Lambertian component vector C, at relative distance ρ between C and I.

5.4 The photometric function

A photometric function typically profiles the change in surface reflectance intensity as the viewing angle changes, where the vertical axis represents the range between minimal and maximal intensity. Since the normalized *rgb* color of a surface is constrained to be on the line between the color of its Lambertian component and the color of the illuminant (i.e., the normalized dichromatic line shown in Figure 5.2), the NPF relates the viewing angle to the point on this line. Hence, the vertical axis of the NPF represents the relative change in normalized color between the color of the illuminant and the color of the Lambertian component of the surface. Equation 5.10 is the basis for the Normalized Photometric Function, which maps the weights of the two reflectance components (i.e., the relative distance along the dichromatic line) as a function of the relative viewing angle. Hence, the horizontal axis represents the relative viewing angle (the term n from Equation 5.10), which ranges from -90° and 90°. At $n = 0°$, the viewing angle equals the angle of maximal specularity. The vertical axis, scaled from 0 to 1,

represents the relative distance (the term ρ from Equation 5.10) between the color of an illuminant and the apparent color of the Lambertian component of the surface under that illuminant.

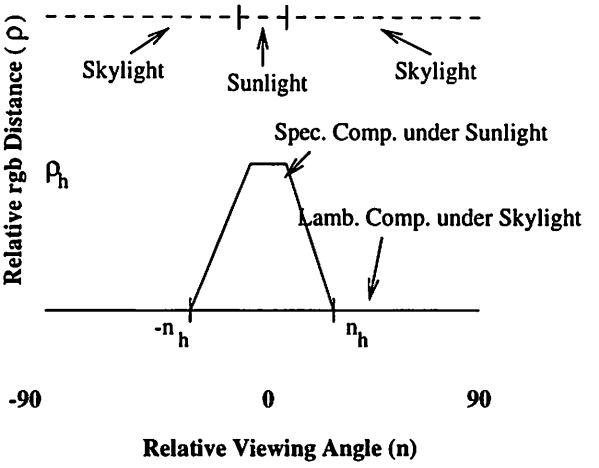

Figure 5.3. The theoretical NPF for a surface with both Lambertian and specular components, under daylight while facing the sun. The distance between the upper and lower lines (ρ) represents the relative distance between the normalized colors of the illuminant and the Lambertian component of the surface under that illuminant. As the relative viewing angle approaches 0°, the apparent color of the surfaces with a specular component approaches the color of the illuminant. The height of the NPF peak depends on the specularity of the surface and the visibility of the sun. The width of the peak can be different at its apex and base: the width of the peak apex depends on the angle subtended by the sun, and is assumed constant at 0.5° for all surfaces with a specular component. The width of the peak base depends on the surface roughness; it is about 0.5° for a perfectly smooth specular surface (same as the peak apex), and wider for rougher specular surfaces.

5.4.1 Empirically obtaining the NPF for particular surfaces

This section describes the process of empirically obtaining the NPF for given surfaces, including determining the width and height of the specular peak. It is shown in Chapter 6 that every pixel in the image is at a different viewing angle with respect to the surface normal; hence, the relative viewing angle and consequently the apparent color of a surface changes over image pixels. Hence, if a surface is large enough (and depending

on the camera field-of-view), its NPF can be estimated from a single image with the surface facing the sun (i.e., with an incident angle of 0°). However, if the surface is not large enough, multiple images are required, so that the entire -90° to 90° range can be measured.

For a given image, the color of the illuminant is determined from the daylight table, based on which the apparent color of the Lambertian component is estimated using the color-coefficient model. The portion of the row of pixels on the surface passing through the centroid, is then selected, and for each pixel, the value of ρ (i.e., the relative position of the pixel's *rgb*, between the Lambertian and illuminant *rgb* points) is mapped against the relative viewing angle at that pixel, based on the surface's *rgb* value at that pixel. Depending on the relative strengths of the Lambertian and specular components of a surface, three cases are possible:

- If the Lambertian component is dominant for all viewing angles, there is no change in the apparent color of the surface, even as the relative viewing angle (n) changes from -90° to 0°, and eventually to 90°; the color is always that of the Lambertian component under that illuminant. The scale factor m_b from Equation 5.4 equals 1, and $m_s = 0$. Hence the value of ρ for the NPF stays at 0 for the whole range of viewing angles.
- If both reflectance components are strong (as shown in Figure 5.3), when n is -90° $m_b = 1$, and the apparent color of the surface is the apparent color of the Lambertian component under the illuminant. It stays that way until n approaches 0°, at which point m_b decreases to some fraction (say, ρ_h) such that ($0 \leq \rho_h \leq 1$), and m_s undergoes a corresponding increase to ($1-\rho_h$). The precise value of ρ_h will

depend on the specularity of the surface and on the sun-visibility factor from Table 4.1 (this phenomenon is discussed shortly). Notice that ρ changes to ρ_h at some point ($-n_h < 0°$), rather than at ($n_h = 0°$). This is because the sun is an area-source illuminant, not a point-source;[25] for ($n \geq n_h$), $\rho = 0$. The width of the peak is also a function of the surface roughness; this phenomenon is also described shortly.

- For surfaces with a dominant specular component, the only difference is that for ($-n_h > n > n_h$), $\rho = 1$, since $m_s = 1$ and $m_b = 0$. In the special case where ($c_b(\lambda) = 0$), which happens for perfect mirrors, at all ($n \geq (-n_h)$ and ($n \leq n_h$), no light is reflected from the surface.

The NPF peak under daylight is a plateau, where the width of the apex of the peak is different from the width of the base. In other words, the bottom of the peak starts at $-n_h$ and the plateau (the flat top of the peak) may start at some point $-n_p$, such that the condition ($-n_h < -n_p < 0$) is true. The width of the apex depends on the angle subtended by the sun, which is assumed constant at 0.5° [98]. Hence the NPF's for all surfaces with a specular component have a peak apex range of 0.5°. The width of the base of the NPF peak (i.e., the range ($-n_h$ to n_h)) depends of the surface roughness, and is similar to the α factor in the Phong model. As in the Phong model, this factor is empirically derived for the NPF of each surface. For a perfectly smooth specular surface, the width of the peak base is the same as the width of the peak apex, which is 0.5°. For an imperfectly smooth surface such as a traffic sign, the base of the peak was empirically found to span a range

[25] In the case of a point-source illuminant, ($\rho = 0$) for all ($-90° \leq n < 0°$) and for ($n > 0°$); at ($n = 0°$), ρ equals ρ_h.

of about 4.5°. For imperfectly specular surfaces (i.e., with some roughness, such as a slightly worn shiny plastic surface), the base width was found to be about 7.2°.

Note that the width of the NPF peak is not just a property of the surface, but specifically of the surface reflectance under daylight. In other words, the width may be different under a different illuminant. The slope of the NPF peak (i.e., $\rho_h/(n_h-n_p)$) depends on the relative widths of the peak's apex and base, and hence is also a property of the surface and its reflectance under the illuminant. The slope of the peak also depends on another characteristic of the illuminant—the color gradient between the sunlight and skylight. Intuitively, the sharper the color gradient, the sharper the slope. For instance, if the boundary between the sun and sky is "blurred" (due to sun obscuration), the slope is "gradual"; if the boundary is sharp, the slope is "steep". A formal method for determining the slope of the peak is not presented because the NPF for a given surface is derived empirically from samples of daylight and the target surface. In addition, one problem with measuring and estimating the slope of the peak is that the pixels representing the gradient can be affected by color-mixing due to pixel interpolation by the camera, and hence may not be reliable.

Hence, the NPF of a surface has eleven free parameters: nine are the Lambertian weights from the color coefficient matrix, and the other two are the height of the apex and the width of the base. Note that the width of the apex will always be 0.5° under daylight. It was mentioned earlier that the nine weights are derived from three images; the following discussion describes the process for empirically estimating apex and base widths.

Figure 5.4 and Figure 5.5 show the NPF's for five surfaces under daylight facing the sun: matte paper, two traffic signs, a concrete slab, and a slab of road asphalt. The NPF for each surface was determined from three images of which the first image had a relative viewing angle of 0° with respect to the surface normal at the centroid of the surface. Depending on the size of the surface, this encompassed a range of viewing angles between -10° and 10° for the largest surface (the "Stop" sign), and between -5° and 5° for the smallest (the matte paper). The NPF was determined—as described before—by selecting a row of pixels passing through the centroid of the surface and measuring the *rgb* values of the pixels on the surface. Thereafter, the data is plotted as a two-dimensional function, with the relative viewing angle on the horizontal axis and the distance between the *rgb* colors of the illuminant and the Lambertian component under that illuminant along the vertical axis. In order to reduce the effect of pixel-level noise, the value at each pixel is taken as the average over a 3×3 neighborhood. None of the five surfaces are large enough to encompass a range of viewing angles larger than -10° to 10°; hence, to measure the apparent color of the surfaces outside the range available from a single image, the viewing angle was changed so as to incorporate the entire -90° to 90° range.

An NPF is fitted to the data according to the one of two conditions:

1. If a single straight line at $\rho = 0$ can be fitted to *all* the points (with a statistically significant goodness-of-fit or R^2, based on the noise model described in Chapter 6), that line defines the NPF for the surface. This means that the surface has a negligible specular component.

2. Otherwise, it is concluded that the surface has a specular component, and that the NPF should have a peak. As described earlier, the width of the apex of the peak is constant for all surfaces under sunlight, and the width of the base of the peak is empirically determined. The samples of the surface are then used to determine the height of the peak: A single straight line at $\rho = 0$ is fitted to points in a range of angles ($-90^\circ \geq \theta \geq -n_h$), and a second straight line is fitted to the two points at $\theta = n_h$ and $\theta = 0.5^\circ$. Then, if this set of two lines can be symmetrically fit across the $\theta = 0^\circ$ axis to the remaining points, the symmetric piecewise linear function defines the NPF for the surface.

The above process was applied to each of the surfaces in shown Figure 5.4 and Figure **5.5** (matte paper, "Stop" sign, "No Parking" sign, concrete slab and road asphalt), the average RMS errors from using the above procedure to fit the NPF's were 0.007, 0.013, 0.081, 0.108, and 0.113, respectively. For each surface, the NPF fit was calculated over 17 points at various relative viewing angles. The errors from fitting the sampled data to the NPF model are greater for the slab of concrete and asphalt and the "No Parking" sign, than for the other two surfaces. This is because the concrete, asphalt and the "No Parking" sign are neutral-colored (grey and white, respectively) which means that their apparent color is always close to the color of the illuminant. Since the points representing the illuminant and the Lambertian component under the illuminant are very close to each other in *rgb* space, even small errors in *rgb* appear magnified relative to the total distance between the two points.

The height of the NPF in outdoor images also depends on two other factors: the illumination geometry and the visibility of the sun (as defined in Table 4.1). When the

surface faces away from the sun, the conditions causing the specular peak do not exist, and there is no specular peak. On the other hand, if the surface faces the sun, but the sun is behind a cloud, the specular peak either completely disappears, or is reduced in height, depending on the thickness of the cloud. Hence, it is necessary to scale the NPF based on the illumination. Although it is difficult to predict the precise effect of the sunlight on the specular peak, an approximate estimate is made using the sun-visibility factor. The scaling is done by multiplying the height of the NPF peak by the sun-visibility factor. The data in Figure 5.6 was collected from images of the two traffic signs under a cloudy sky, with the sun-angle at 27^{o} and a sun-visibility factor of 0.5 (see Table 4.1 for more information about those conditions). Figure 5.6(a) shows *rgb* color of the "No Parking" sign, plotted relative to the distance from the illuminant color; the figure also shows an NPF, scaled by the sun-visibility factor of 0.5. Figure 5.6(b) shows the sampled data and the NPF scaled at 0.5 for the "Stop" sign. The RMS errors between the sampled data and the scaled NPF's for the two surfaces were 0.144 and 0.073, respectively. Note that the NPF's for only those surfaces with a specular peak (when a single straight line cannot be fitted to the photometric data) need illuminant-based scaling.

Note that the ability of an illuminant to cause a specular *peak* should not be confused with the ability to cause specular *reflection.* A specular surface will always exhibit specular reflection—the specular *peak* associated with that reflectance will be visible only under a single-source illuminant (point or otherwise), or under daylight when sunlight is incident. Under an ambient illuminant (such as skylight), there will be specular reflection at *every* viewing angle and hence there will be no single peak.

The NPF model is used to first determine the apparent color of the Lambertian component (using the color-coefficient matrix), and the offset in the direction of the illuminant. It was mentioned earlier that the color-coefficient matrix can be estimated from three sample images. In order to determine the width of the NPF peak (given the size of the surface and the surface-camera distance), and the maximum height of the NPF peak (which can then be scaled based on the sun visibility), a fourth sample image is required, under conditions resulting in maximal specularity for the surface (i.e., at a relative viewing angle of 0^{o}, facing the sun with a visibility factor of 1). For each of the surfaces in Figure 5.4 and Figure 5.5, the NPF's are estimated from four images. In Chapter 6 these NPF's are combined with the daylight model for estimating the apparent color of the five surfaces under various conditions, and the estimates are used for classifying image pixels.

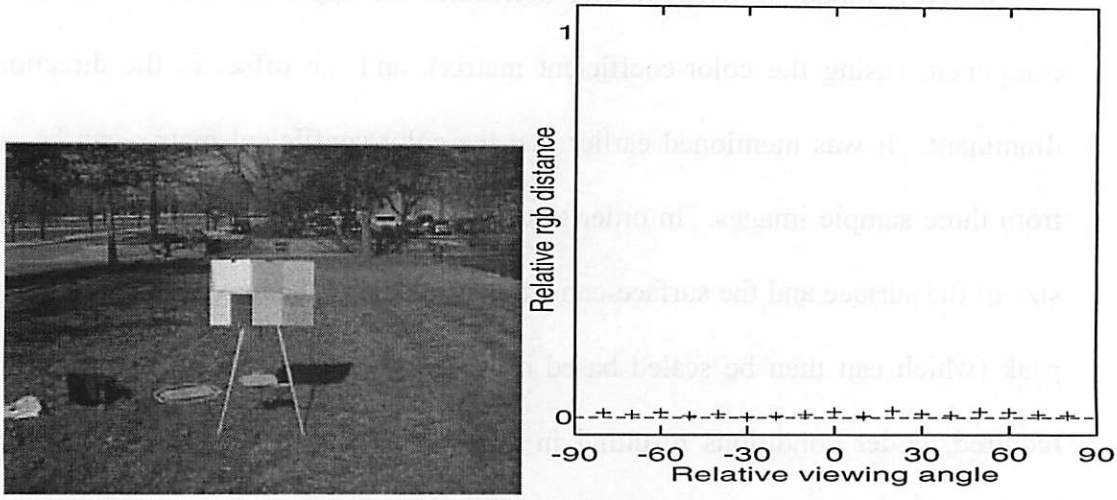

(a) Matte paper

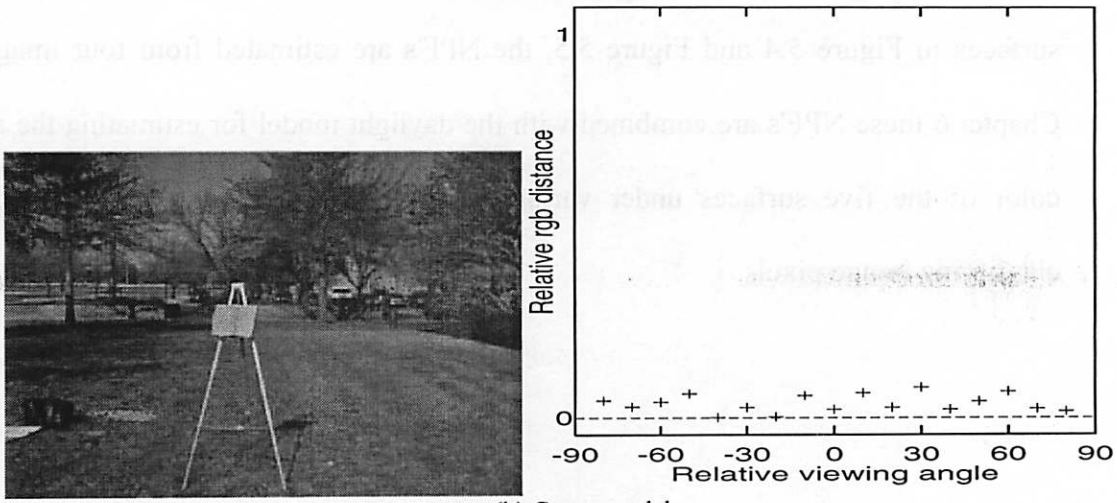

(b) Concrete slab

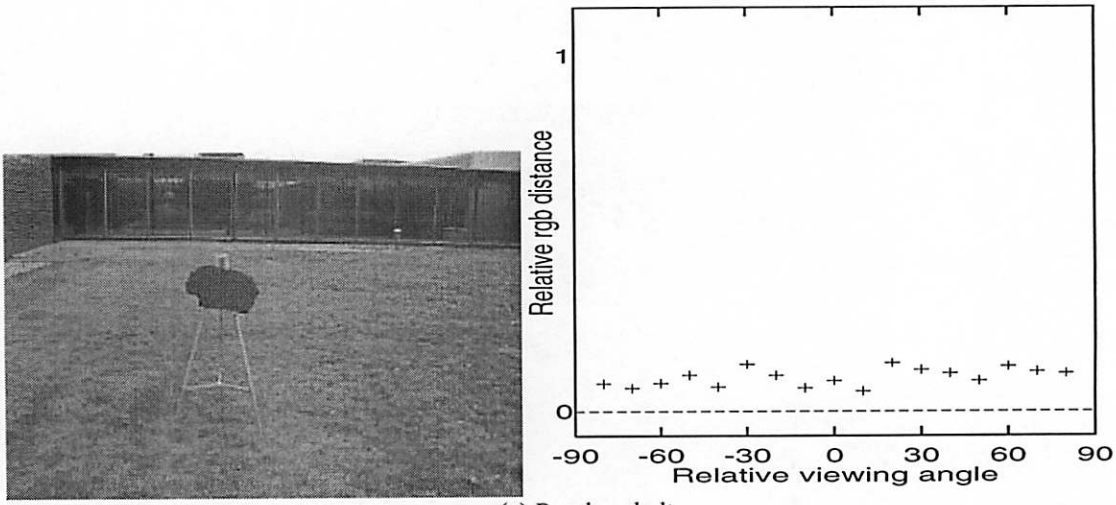

(c) Road asphalt

Figure 5.4. Normalized Photometric Functions for three of the five sample surfaces (under daylight, facing a bright sun): (a) matter paper, (b) concrete slab, (c) road asphalt.

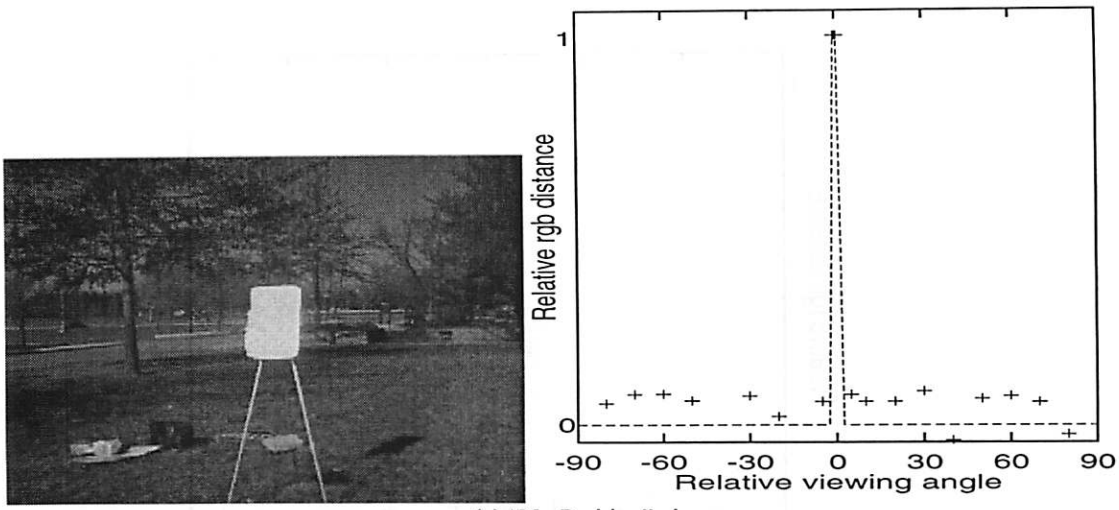

(a) "No Parking" sign

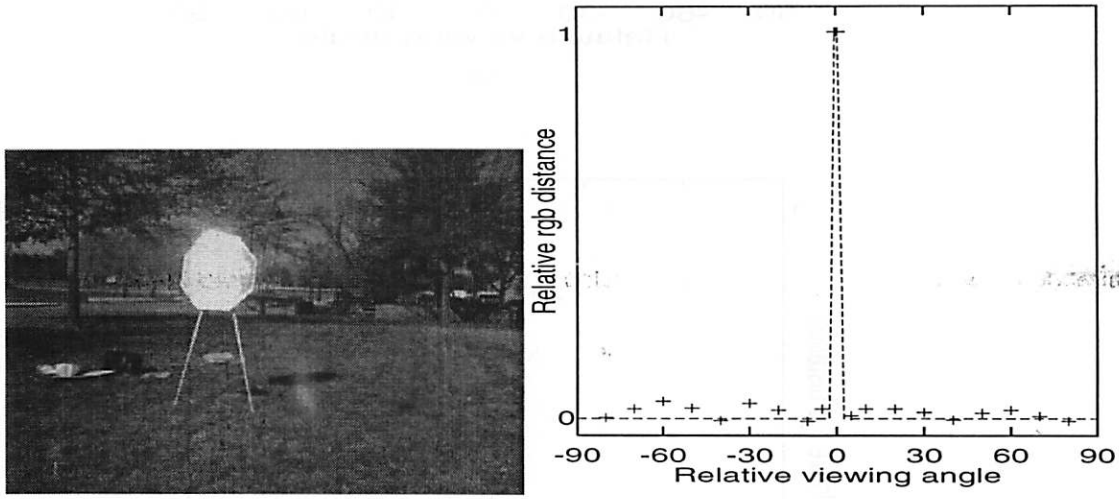

(b) "Stop" sign

Figure 5.5. Normalized Photometric Functions for the remaining two of the five sample surfaces (under daylight, facing a bright sun): (a) "No Parking" sign, (b) "Stop" sign.

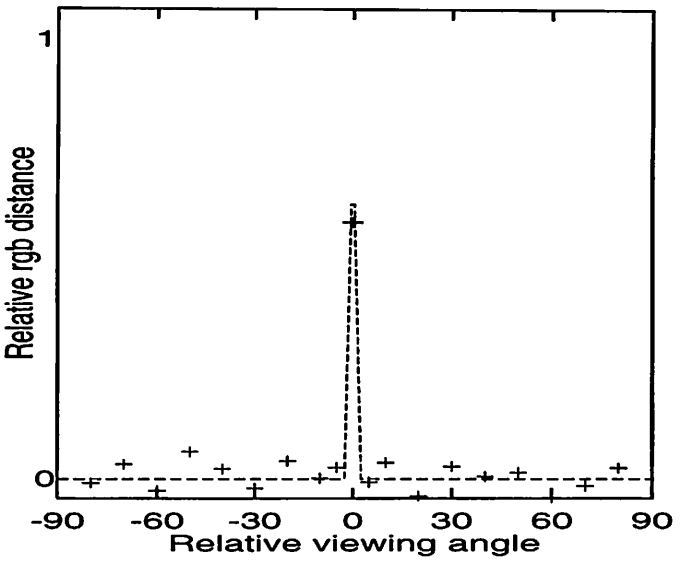

(a)

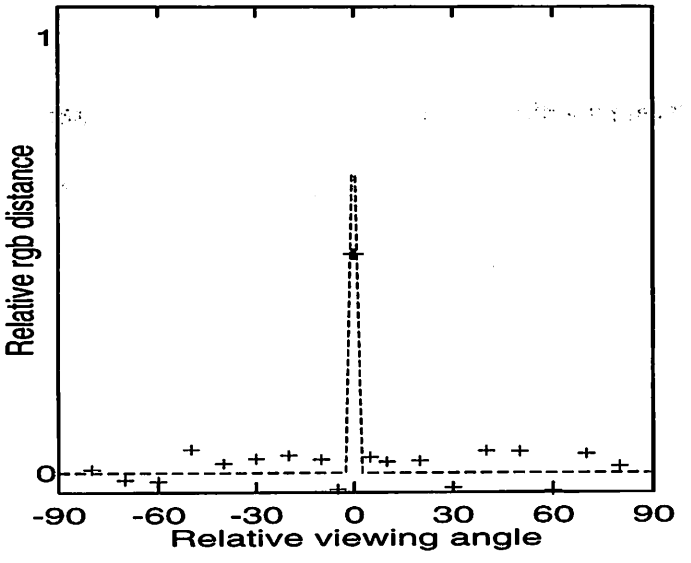

(b)

Figure 5.6. NPF's for the traffic signs facing the sun under partly cloudy sky: (a) "No Parking" sign, (b) "Stop" sign.

CHAPTER 6

ESTIMATING APPARENT NORMALIZED COLOR

6.1 Overview

As mentioned earlier, one motivation for developing models of daylight color and surface reflectance is to predict apparent surface color in outdoor images. While the previous two chapters introduced a model of daylight color and a surface reflectance model represented by an NPF, this chapter describes the process of combining the two models to estimate apparent color.

Note that the NPF uses the relative viewing angle, which, as the reader may recall, combines the illumination and viewing angles; however, these angles may not always be known. Hence, this section develops methods for estimating apparent color under two scenarios: when the relative viewing angle is known (Section 6.2) and when it is unknown (Section 6.3). Section 6.4 develops a method for classifying image pixels based on the estimated apparent color, and the probability that a given image pixel is the same color as the estimate, within the constraints of the noise model. A total of 90 images under different conditions are used to test the methods; these conditions are described (along with the results) in the sections discussing each of the sample surfaces.

6.2 Estimating apparent color when the relative viewing angle is known

When the relative viewing angle (in addition to the daylight conditions and surface reflectance) is known, it is possible to use the daylight table (Table 4.1), along with the color-coefficient and NPF models to estimate the apparent color. In the absence of noise or other sources of error, this prediction is an *rgb* point on the normalized dichromatic

line. In practice, however, there are three sources of error: the models of daylight and surface reflectance, and the relative viewing angle. Since the color of the incident light is estimated from the empirical measurements in Table 4.1 (which have non-zero errors), the error associated with this estimation is approximated as a Gaussian distribution, the standard deviation of which equals that of the measurements shown in Table 4.1. The error in estimating the NPF for each surface is also modeled as a Gaussian, the standard deviation of which is derived empirically using the method described in the next section. Finally, because the relative viewing angle is provided by a user or an external system (not estimated from data), the user must provide an estimate of its accuracy. An error in the estimate of the relative viewing angle changes the estimate of the apparent color from a point on the dichromatic line to a segment of the dichromatic line; the magnitude of the error determines the length of the line-segment. Note that if the NPF function is flat around the estimated relative viewing angle,[26] then the prediction will be a point in *rgb*, and the error model reduces to a Gaussian distribution around a point; this, however, is a special case. In the general case, the error model for predicting apparent color is a Gaussian distribution that combines the errors associated with the estimates of the illuminant color and the surface reflectance models, centered around a line of possible apparent colors generated by the uncertainty in the relative viewing angle. In other words, it is a Gaussian distribution centered around a segment of the normalized dichromatic line.

[26] This can happen due to three reasons: (a) because the surface is Lambertian, (b) because the sun is not visible, or (c) because the relative viewing angle is outside the specular range.

6.2.1 Deriving the Gaussian noise model

The probability distribution representing the composite error from the three sources is derived by convolving the individual errors from each source. The error from the daylight model for the gamut of conditions was shown in Table 4.1 to be about 0.007 (and assumed symmetric along *r* and *g*). The second source of noise is the NPF, the error from which was determined in a test over the five target surfaces. For each surface, the color-coefficient matrix and NPF were estimated and then used to predict the apparent color of the surfaces under three different conditions with known illuminant color (for a total of 15 tests). Note that while estimating the average error of the reflectance, the color of the incident light was measured directly by placing the white surface in the image, *not* from Table 4.1. This was done in order to separate the errors due to the reflectance model from errors in the daylight model. When the Gaussians representing the errors from the daylight and reflectance models are convolved, the result is another Gaussian representing the composite error from the two sources. This composite Gaussian represents the overall error model around an *rgb* point (the Lambertian point on the dichromatic line) when the NPF at the relative viewing angle is flat (as discussed above). If the NPF has a peak, the apparent color of the surface is a point on the dichromatic line, and the error model is a Gaussian distribution around a segment the dichromatic line. The error associated with the relative viewing angle is a one-dimensional Gaussian, which is incorporated into the composite error model by convolution with the two-dimensional Gaussian (representing the errors from the reflectance and daylight models). The probability distribution representing the composite of these two Gaussians is estimated by separating the two-dimensional Gaussian into the

two orthogonal dimensions, one along the dichromatic line and the other along the normal to the dichromatic line. Thereafter, the one-dimensional Gaussian from the relative viewing angle error is convolved with one-dimensional Gaussian along the dichromatic line, resulting in a composite one-dimensional Gaussian. Finally, this Gaussian is convolved with the one-dimensional Gaussian orthogonal to the dichromatic line, resulting in a composite two-dimensional asymmetric probability distribution which represents the error associated with the combination of the three sources. In the examples to follow, the error in estimating the viewing angle is assumed to be 1°, based on multiple measurements and the resultant average errors.

6.2.2 The viewing angle at each pixel

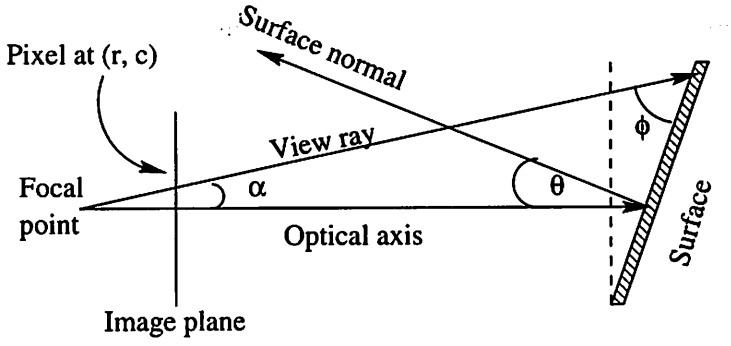

Figure 6.1. Viewing geometry for image pixels: The viewing angle(φ) for a pixel at position [r,c] equals (90 + α - θ), where θ is the angle between the optical axis and the surface normal, and α is the angle of the viewing ray at pixel [r,c], which is determined the field-of-view of the camera.

The next step in estimating the apparent color of the surface is determining the viewing angle at each pixel in the image. Different image pixels will have different relative viewing angles (the angle between the surface normal and the viewing ray). Since the viewing angle for specular surfaces determines the relative strengths of the reflectance components, it is possible for some pixels on the surface to exhibit

specularity, while other pixels on the surface do not. Figure 6.1 describes the geometry used for estimating the viewing angle at individual pixels. In this figure, θ represents the angle between the surface normal and the optical axis. All viewing rays not parallel to the optical axis will have different angles with respect to the surface normal; this angle is a function of the position of the pixel (row and column) and the field-of-view of the camera. For the camera used in this study, the field-of-view (horizontal) was 45°, with the image being 504 pixels wide; hence it was assumed that the optical axis goes through the 252nd column[27], and a ray going through a pixel in column c will be at a $\left|\frac{252-c}{252}\times 22.5\right|$ degree angle with respect to the optical axis. In addition to θ, Figure 6.1 shows two other angles: α is the angle between the optical axis and the viewing ray at a pixel $[r,c]$, and φ is the angle between the ray and the surface, if the two intersect. In other words, if the ray going through $[r,c]$ intersects the surface, the viewing angle for $[r,c]$ will be φ; if the ray does not intersect the surface, the question of an angle between the ray and the surface does not arise. Geometrically, $\varphi = 90 + \alpha - \theta$. The relative viewing angle is the difference between the angle of incidence and the viewing angle.

The relative viewing angle at each pixel in the image is determined, and the target surface's NPF is used to estimate the apparent *rgb* color that the surface would be, if it were at that particular pixel. Thereafter, the estimated *rgb* value at a given pixel is compared to the actual *rgb* value of that pixel; if the pixel is on the target surface, the accuracy of the estimation is measured by several performance metrics. If, on the other

[27] This assumes that the camera is properly aligned, with no spherical distortion. In practice the true optical center may range from one pixel left or right (or up or down) for scientific quality cameras (with a small possible error in estimating the angle), to potentially more for lower quality cameras. Calibration will help reduce the effect of such distortions.

hand, the pixel is not on the surface, the question of evaluating the estimation accuracy does not arise.

6.2.3 Results

The tests over 90 images of the five surfaces can be grouped according to performance into two categories: the results for the matte paper, the "No Parking" sign and the "Stop" sign showed a high level of accuracy, while those for the concrete and asphalt slabs were not as accurate. The following is a discussion of the tests and an analysis of the results. In the discussion, the accuracy of the estimate is measured by the number of observed samples found to be within the confidence interval of the estimate. In addition, the certainty of the estimation is measured by the area of *rgb* space within the 2σ confidence interval; in other words, the smaller the area of the interval is, the tighter—and more useful—the constraint imposed by the confidence interval will be.

6.2.3.1 Matte paper

For the matte paper, tests were conducted on 20 images over 4 sets of conditions (Table 6.1). Since the surface does not have a specular component, each set of conditions has a single estimated *rgb* color, which is the apparent color of the Lambertian component. For each of the 20 images, the actual color of the surface was determined by averaging a 20×20 region of the image. All 20 observed values were within the 2σ confidence interval of the estimates under the corresponding conditions. On average, the estimated *rgb* was 0.005 away from the observed *rgb*. Figure 6.2 shows the confidence interval about the estimate under each of the four sets of conditions, along with the

observed *rgb* values for all the images under each set.[28] The area within the interval (i.e., the certainty of the estimate) was about 0.0002 square units (where the confidence interval is a circle with a radius of about 0.008). One reason for the accuracy of the estimate is that the surface is Lambertian, as a result of which the errors due to the NPF and the viewing angle are eliminated.

[28] Section 6.4 discusses the appropriate confidence intervals to be used in the context of pixel classification.

Sun angle	Illumination angle	Viewing angle	% Cloud cover	Sun visibility factor	# Samples	% Observations within CI	Average error
10	0	0	0	1	5	100%	0.004
35	10	0	0	1	4	100%	0.006
50	0	50	80	0	6	100%	0.004
60	180	80	20	1	5	100%	0.005

Table 6.1. Results of apparent color estimation (with known relative viewing angle) for the matte paper. Four sets of conditions were sampled, with each row describing the sun angle, illumination angle, viewing angle, approximate cloud cover, and the sun visibility factor for the corresponding set of conditions. For each set of conditions, the number of samples are shown, along with the percentage of observations that fell within the estimated confidence interval, and the average error from the estimate.

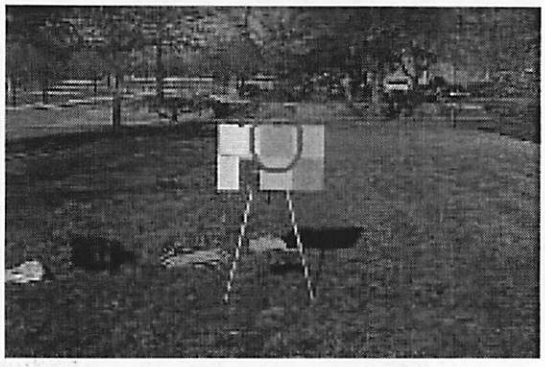

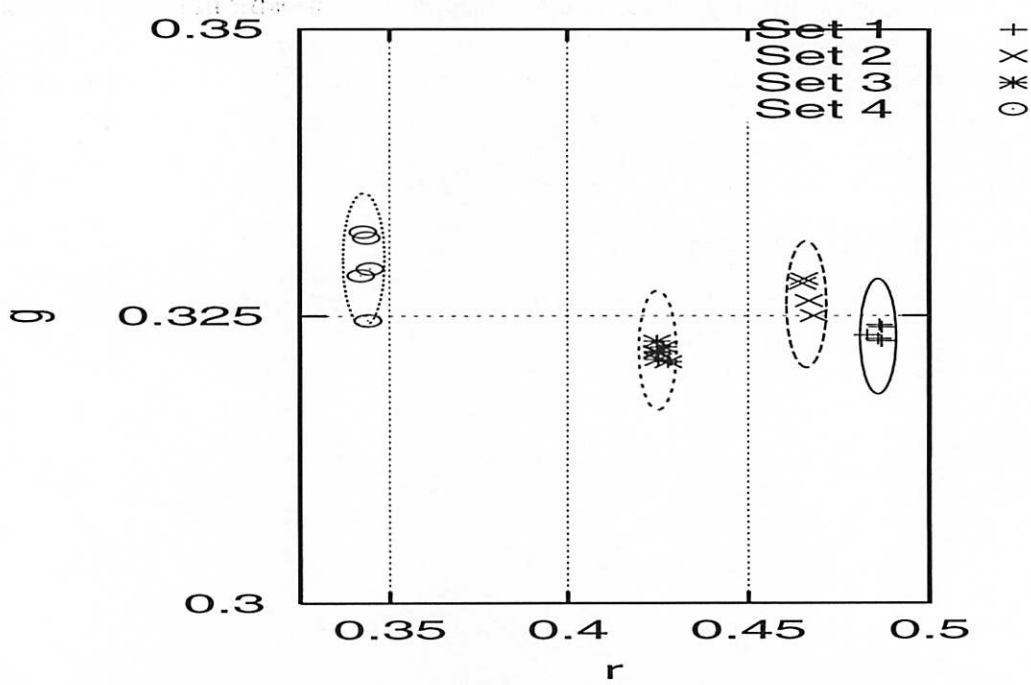

Figure 6.2. Estimates of the apparent color of the matte paper under four sets of conditions are represented by the corresponding confidence intervals. As the figure shows, 100% of the actual observed colors are within the estimated confidence intervals.

6.2.3.2 "No Parking" sign

Sun angle	Illumination angle	Viewing angle	% Cloud cover	Sun visibility factor	Effect	# Samples	% Observations within CI	Average error
10	0	0	0	1	L	4	100%	0.006
35	20	20	0	1	L	4	100%	0.003
35	20	40	0	1	L	2	100%	0.004
60	0	0	50	0.5	L	4	100%	0.004
60	180	-30	20	1	L	5	100%	0.005
10	0	0	0	1	S	4	100%	0.009
35	20	20	0	1	S	4	100%	0.005
60	0	0	50	0.5	S	4	100%	0.004
10	0	0	0	1	T	4	100%	0.009
35	20	20	0	1	T	4	75%	0.015
60	0	0	50	0.5	T	4	100%	0.010

Table 6.2. Results of apparent color estimation (with known relative viewing angle) for the "No Parking" sign over five sets of conditions: Overall, 19 images were sampled out of which 12 exhibited Lambertian, specular and transition effects (shown as L, S and T in the 6th column); the remaining 7 samples exhibited only the Lambertian effect. Note that for the conditions which resulted in all three effects, the results for each effect are in a separate row.

For the "No Parking" sign, the "white" portion of the surface is considered the target, not the "red" lettering. The "No Parking" sign was tested on 19 images under five sets of conditions (Table 6.2). Because the surface is specular, three cases may arise, depending on the sun visibility and the viewing angle: (a) the pure Lambertian case, which will be a single *rgb* point resulting from the base of the NPF (or when the sun is not visible), (b) the pure specular case, which is also a single *rgb* point resulting from the top of the NPF peak, and (c) the transition pixels along the dichromatic line, from the slope of the NPF. In the first two cases, estimates of the *rgb* points representing the actual colors are sampled over the largest possible uniformly colored region of the image. However, the portion of the image representing the transition pixels is not uniformly colored; hence multiple sample pixels are extracted, each possibly representing a different *rgb* color. Of the 19 samples, 12 faced the sun (and hence exhibited specularity); however, since the

surface area of the "No Parking" sign is large enough, a portion of the surface does not reflect sunlight (even when the surface faces the sun). Hence, these 12 samples exhibited the specular, Lambertian and transition effects. The remaining 7 samples faced away from the sun, and hence exhibited only the Lambertian effect. In other words, all 19 samples had Lambertian pixels, whereas only 12 had specular and transition pixels. Table 6.2 separates the results from each set of conditions into each of the three (Lambertian, specular and transition) cases.

Out of the 19 images, all 19 Lambertian samples were within the 2σ confidence interval of the corresponding estimates, with an average error of 0.004 and a confidence interval area of 0.0003. Out of the 12 samples that exhibited specularity, all 12 pure specular pixel samples were within the confidence interval, with an average error of 0.006 and a confidence interval area of 0.0003.[29] Out of the 12 transition pixel samples (one example shown in Figure 6.3), 11 were within the confidence interval, with an average error (measured as the perpendicular distance to the estimated dichromatic line segment) of 0.011. The area of the ellipse representing the confidence interval was about 0.0006 square units. As with the matte paper, the errors for the "No parking" sign are small, and the observed value is within the confidence interval of the estimate. The "No Parking" sign is specular; hence, errors due to the NPF and the relative viewing angle are possible. However, because the albedo of the surface is neutral (near-white), the apparent color of its Lambertian component is very close to its apparent color under specularity—the same as (or very close to, in the non-specular case) the illuminant color. Hence, the length of the dichromatic line is very small. Consequently, errors due the viewing angle

[29] As described in Chapter 2, the f-stop of the camera was restricted to 50-75% of the output, thereby avoiding pixel saturation. In general, however, saturated pixels can be easily detected from their high *RGB* values, and eliminated from consideration.

or the NPF do not make a significant difference, and the primary sources of error are the estimates of the color of daylight and the color-coefficients.

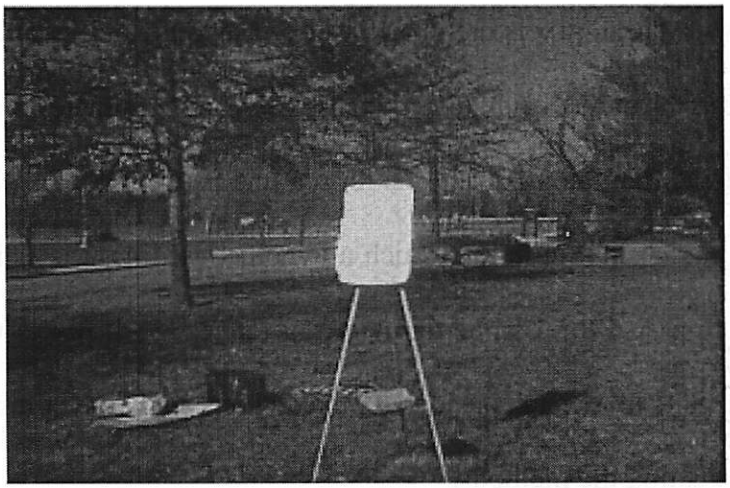

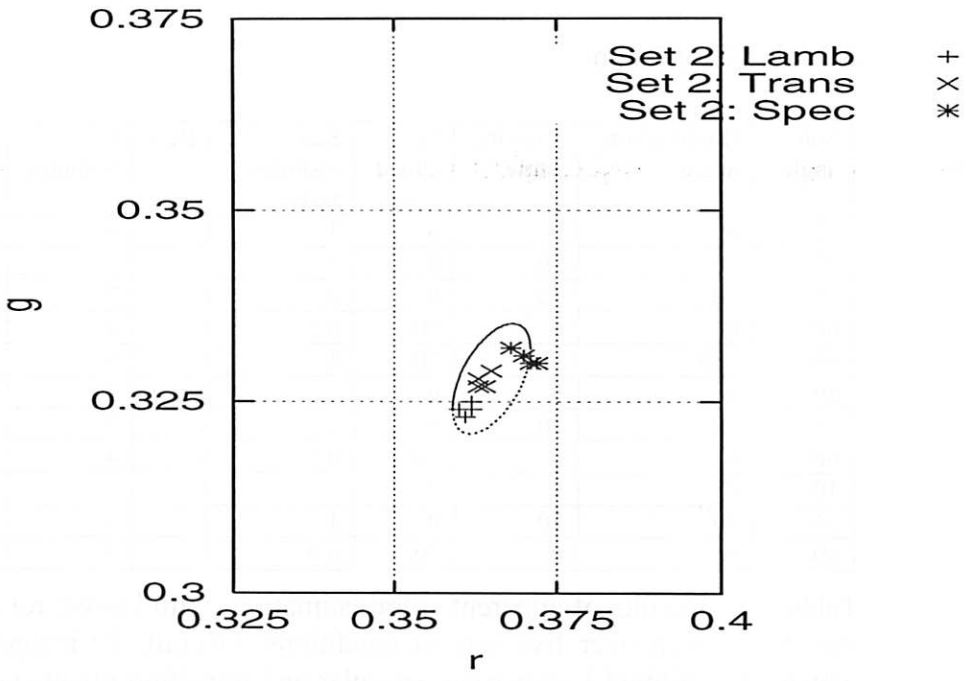

Figure 6.3. Estimated apparent color (confidence interval) of the "No Parking" sign from one set of conditions ("Set 2", the second entry in Table 6.2). The figure shows observed pixel values from the pure Lambertian ("Lamb"), pure specular ("Spec") and the transition ("Trans") cases. In this example, all observed pixels except one transition pixel are within the CI.

Another issue with the "No Parking" sign (and the "Stop" sign, to be discussed shortly) is that of mixed pixels, which are the pixels on or near the edge between the

lettering and the rest of the sign. Due to pixel interpolation (discussed in Chapter 2), these pixels are neither the "white" of the sign nor the "red" of the lettering, but a mixture of the two. These pixels are not considered targets, and would result in larger errors if they were. In order to identify mixed pixels and eliminate them from consideration, it was assumed that the mixed pixels form a line between the pixels on the ("white") target area and the ("red") lettering. Such a hypothetical line was estimated for the target and lettering pixels in the Lambertian viewing range.[30] All pixels within the 2σ confidence interval of this line were considered mixed pixels and were eliminated from consideration while evaluating the methods.

6.2.3.3 "Stop" sign

Sun angle	Illumination angle	Viewing angle	% Cloud cover	Sun visibility factor	Effect	# Samples	% Observations within CI	Average error
10	0	0	0	1	L	5	100%	0.007
35	30	30	0	1	L	3	100%	0.004
35	20	40	0	1	L	2	100%	0.005
60	0	0	50	0.5	L	4	100%	0.005
60	180	-30	20	1	L	5	80%	0.004
10	0	0	0	1	S	5	100%	0.010
35	30	30	0	1	S	3	100%	0.005
60	0	0	50	0.5	S	4	100%	0.004
10	0	0	0	1	T	5	60%	0.022
35	30	30	0	1	T	3	67%	0.015
60	0	0	50	0.5	T	4	100%	0.011

Table 6.3. Results of apparent color estimation (with known relative viewing angle) for the "Stop" sign over five sets of conditions: Overall, 19 images were sampled out of which 12 exhibited Lambertian, specular and transition effects (shown as L, S and T in the 6th column); the remaining 7 samples exhibited only the Lambertian effect. Note that for the conditions which resulted in all three effects, the results for each effect are in a separate row.

[30] Note that the specular range was not used because the target and lettering areas are both specular and would look identical under specular conditions.

For the "Stop" sign, the "red" portion of the surface is considered the target area, and the white lettering and border is considered background. As with the "No Parking" sign, three cases occur: the pure Lambertian, the pure specular, and the transition pixels. Out of 19 sampled images over 5 sets of conditions (see Table 6.3), 12 exhibited specularity (and hence had pixels with Lambertian, specular and transition effects), while the remaining 7 exhibited only the Lambertian effect. For the Lambertian cases, 18 of 19 estimates were within the 2σ confidence interval, with an average error of about 0.005; the area of the confidence interval was about 0.0004 square units. For the pure specular cases, all 12 were within the interval, with an average error of 0.006; the area of the confidence interval in this case was 0.0005. For the transition cases, 9 out of the 12 samples were within the interval, with an average error of 0.017, and a confidence interval of area 0.001 square units. Figure 6.4 shows one set of samples, with 2 pixel values outside the estimated confidence interval, and the rest inside. One reason the failure rate is higher for the "Stop" sign than for the "No Parking" sign is that the dichromatic line for the "Stop" sign is long; as a consequence, a small error in the orientation of the estimating dichromatic line can cause larger errors towards the extremities of the line.

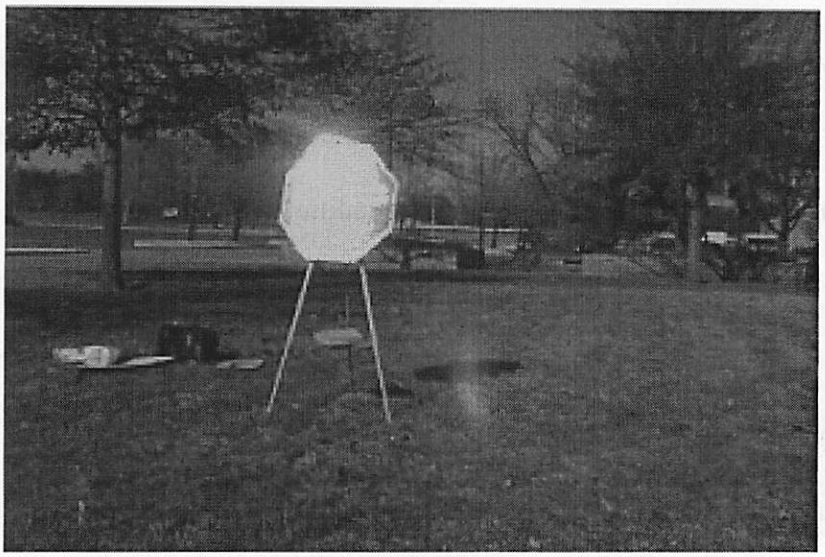

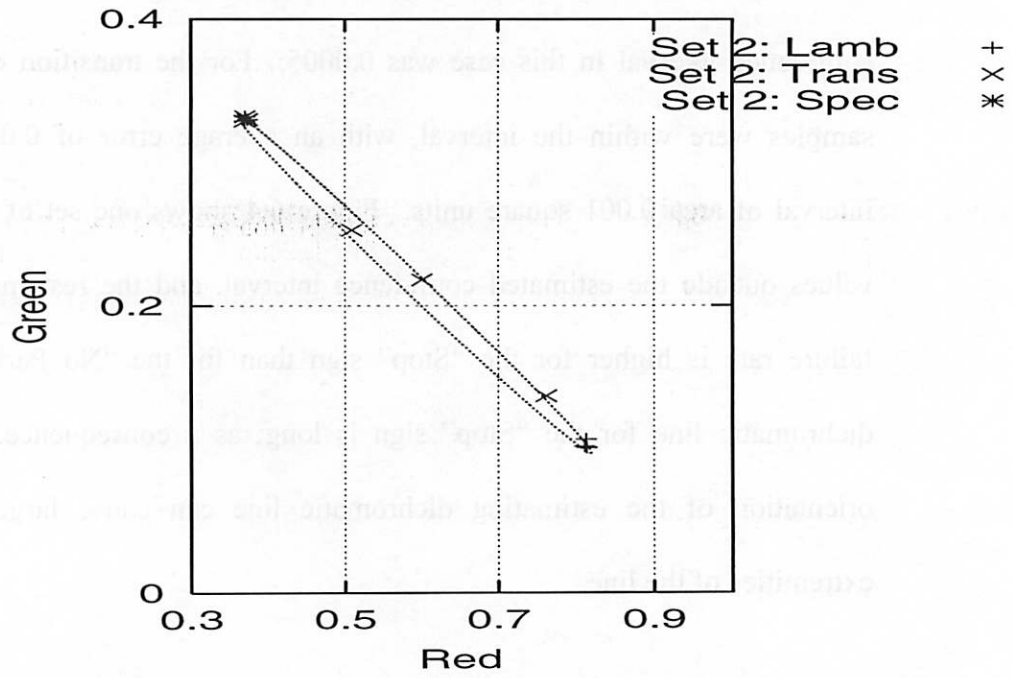

Figure 6.4. Estimated apparent color (confidence interval) of the "Stop" sign from one set of conditions ("Set 2", the second entry in Table 6.3). The figure shows observed pixel values from the pure Lambertian ("Lamb"), pure specular ("Spec") and transition ("Trans") cases. In this example, the observed values of one transition and one Lambertian pixel are outside the CI, and all others are inside.

6.2.3.4 Concrete slab

For the concrete surface, tests were conducted on 16 images under 4 conditions (see Table 6.4). The concrete slab in the figure is not uniformly colored, as a consequence of which the standard deviation of the *rgb* colors over the surface is 0.009, which is significantly higher than that of the matte surface and the Lambertian samples of the traffic signs. This, in turn, has two consequences: first, that the area within the confidence interval is large, and second, that samples not included in the original estimate of the standard deviation can be outside the confidence interval. Out of 16 observed values, 14 were within the 2σ confidence interval of the corresponding estimates. The average error between estimated and observed values was about 0.011. On average, the area within the interval was about 0.001 square units. Figure 6.5 shows the confidence interval about the estimate under each of the four sets of conditions, along with the observed *rgb* values for all the images under each set. Noticeable in figure is that the confidence intervals are significantly wider than the Lambertian cases of the previously discussed surfaces.

6.2.3.5 Road asphalt

For the concrete surface, tests were also conducted on 16 images under 4 conditions (see Table 6.5). The results from the slab of road asphalt were worse than those for the concrete slab—the average error between the estimated and observed *rgb* values was 0.011, with only 13 out of the 16 samples within the confidence interval. The reason for the poor performance is a more extreme case of the same factor affecting the concrete slab: the road surface is not uniformly colored, with a standard deviation of 0.012, and a

confidence interval with an area of about 0.002 square units. Figure 6.6 shows the observed values compared to the confidence intervals around each estimate, along with the observations under those conditions.

Sun angle	Illumination angle	Viewing angle	% Cloud cover	Sun visibility factor	# Samples	% Observations within CI	Average error
10	0	0	0	1	4	75%	0.015
35	10	0	0	1	4	100%	0.007
50	0	50	80	0	4	100%	0.008
60	180	80	20	1	4	75%	0.014

Table 6.4. Results of apparent color estimation (with known relative viewing angle) for the concrete slab. Four sets of conditions were sampled over 16 images.

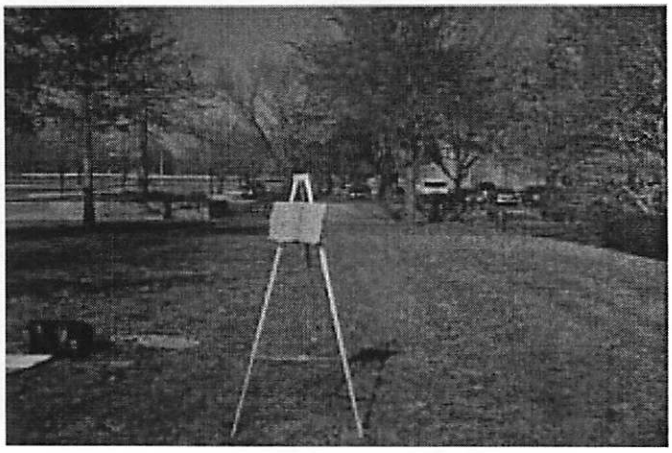

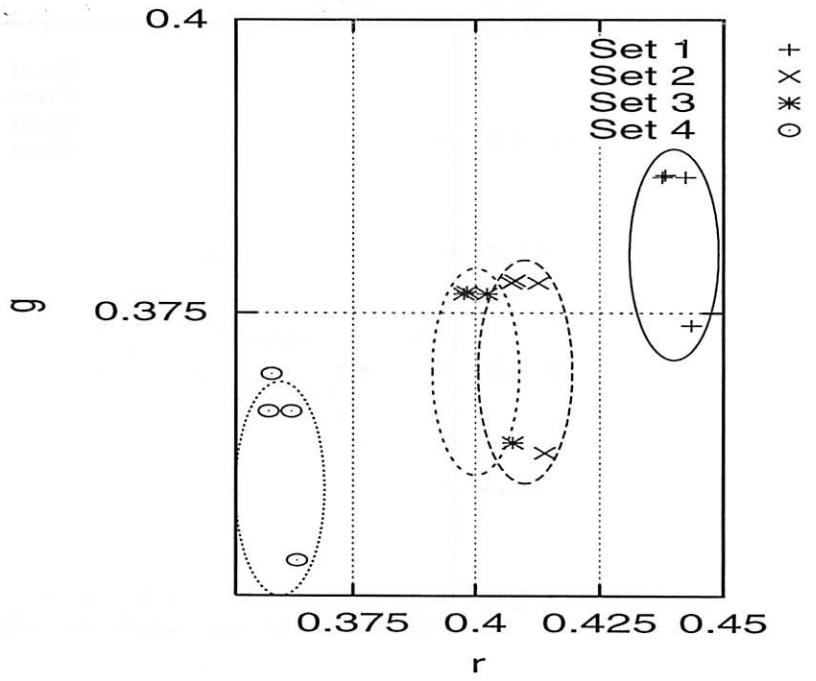

Figure 6.5. Estimates of the apparent color of the concrete slabs under four sets (results labeled "Set 1", "Set 2", and so on, corresponding to respective entries in Table 6.4) of conditions—represented by corresponding confidence intervals—under a sample set of conditions. The figure shows that 14 observations out of 16 lie within the respective confidence intervals.

Sun angle	Illumination angle	Viewing angle	% Cloud cover	Sun visibility factor	# Samples	% Observations within CI	Average error
10	0	0	0	1	4	75%	0.015
35	10	0	0	1	4	100%	0.007
50	0	50	80	0	4	100%	0.008
60	180	80	20	1	4	75%	0.014

Table 6.5. Results of apparent color estimation (with known relative viewing angle) for the slab of road asphalt. Four sets of conditions were sampled over 16 images.

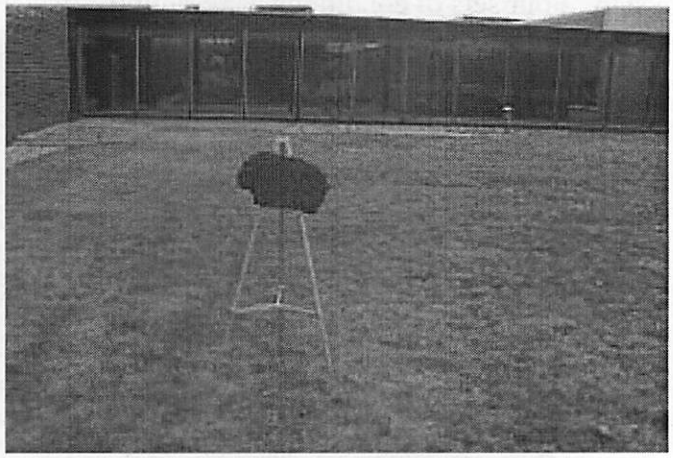

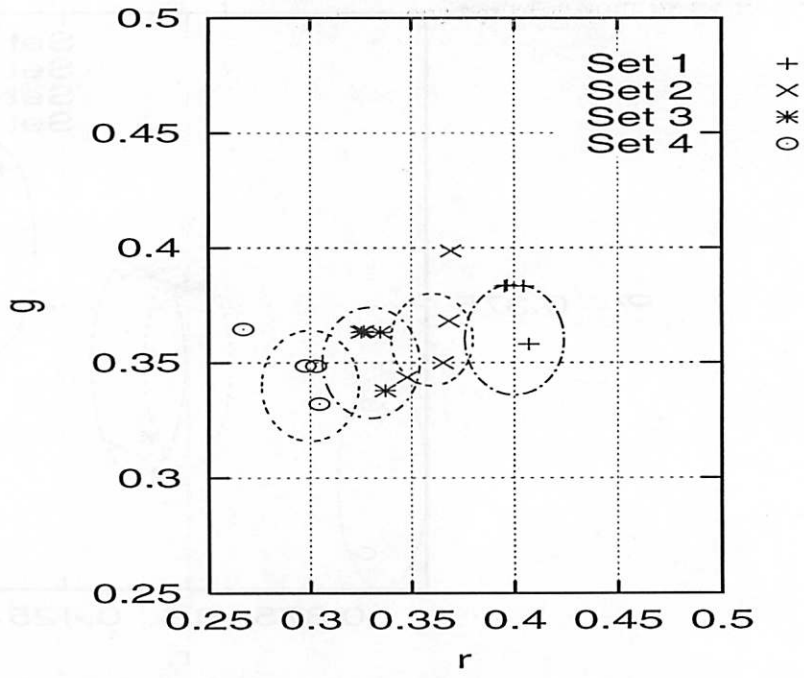

Figure 6.6. Estimates of the apparent color of the slab of road asphalt under four sets (results labeled "Set 1", "Set 2", and so on, corresponding to respective entries in Table 6.5) of conditions—represented by corresponding confidence intervals—under a sample set of conditions. The figure shows that 13 observations out of 16 lie within the respective confidence intervals.

6.3 Estimating apparent color when the viewing angle is unknown

The difference between estimating apparent color with and without knowledge of the relative viewing angle is that the latter case has an uncertainty in the viewing angle of 180°. The apparent color is predicted to lie anywhere along the dichromatic line, leading to less precise predictions. Note that the only surfaces to which the relative viewing angle applies are those with a peaked NPF (i.e., specular surfaces with sunlight incident upon them).

Just as Section 6.2.1 derived a noise model for estimating apparent color with known relative viewing angle, the following discussion derives the noise model when the relative viewing angle is not known. There are only two sources of noise in this method of estimation: the error associated with the linear daylight function (Equation 4.3) and the color-coefficient model. The error for the linear daylight function was discussed in the previous section, and that for the coefficient model was determined in a test similar to that used to derive the NPF error. When the two Gaussians are convolved, the composite error model (for each surface) is a Gaussian centered about the dichromatic line for the surface.

For the "No Parking" sign, the average error, measured as the perpendicular Cartesian distance to the dichromatic line to the observed *rgb* point, was 0.006, and 18 out of 19 samples were within the confidence intervals which had an average area of about 0.0007 square units. For the "Stop" sign, the average error was 0.018, with 17 of 19 points being within the confidence intervals which had an average area of about 0.006 square units. When compared to the results when the viewing angle is known, the major difference is that the confidence intervals tend to be larger when the viewing angle is not known,

because the estimate is a line segment instead of a point. Hence, even though error margins appear similar, they are being measured differently: in the earlier case, the error was being measured as a distance to a point; in this case the error is the perpendicular distance to a line. Broader implications of this difference will become evident in the following section, where image pixels are classified on the basis of the estimated apparent color—larger confidence intervals will result in less accurate pixel classification.

6.4 Pixel classification

After the apparent color is estimated for the specified conditions, image pixels can be classified as either target or background. This section uses a classification method that is based on the probability of a pixel being within the 2σ confidence interval of its estimated apparent color. Classification results on the 90 images described in the following sections for cases when the relative viewing angle is knows, and for those when it is not. The classification results are evaluated in terms of two measures: the true positive rate and the false positive rate. The true positive rate is the percentage of on-target pixels that are correctly classified as targets, and the false positive rate represents the percentage of background pixels that have been mis-classified as target.

6.4.1 Gaussian noise model for classification

The previous section discussed the noise models used for accounting for errors due to the various empirical parameters. In order to determine the discriminant between target and background pixels, this section examines Receiver-Operator Characteristic (ROC) curves for each of the five target surfaces and the corresponding Gaussian distributions.

The curves, based on 30 images of each surface, are shown in Figure 6.7 and Figure 6.8 plotting the true positive probability against the false positive probability for confidence intervals of σ, 2σ, 3σ and 4σ. Note that the slope of all five curves is greater than or equal to 45° at the 4σ, 3σ and 2σ, levels, but fall below 45° beyond the 2σ level. While the optimal confidence interval for each surface depends on the particular application and the tolerance for false positives and false negatives, a 2σ interval is assumed for all the five surfaces based on the ROC curves.

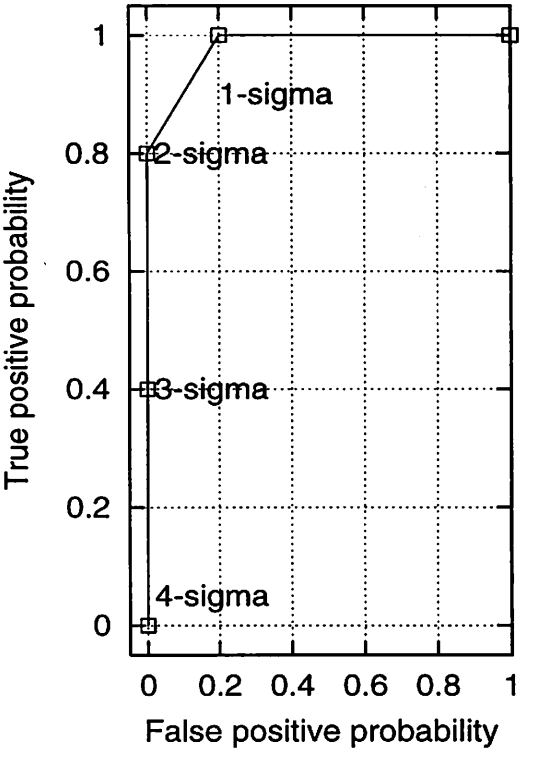

Figure 6.7. ROC curve for the matte surface. The curves plot the probability of a true positive against the probability of a false positive for confidence intervals of σ, 2σ, 3σ and 4σ. Based on the above curve, a 2σ confidence interval was chosen for classification.

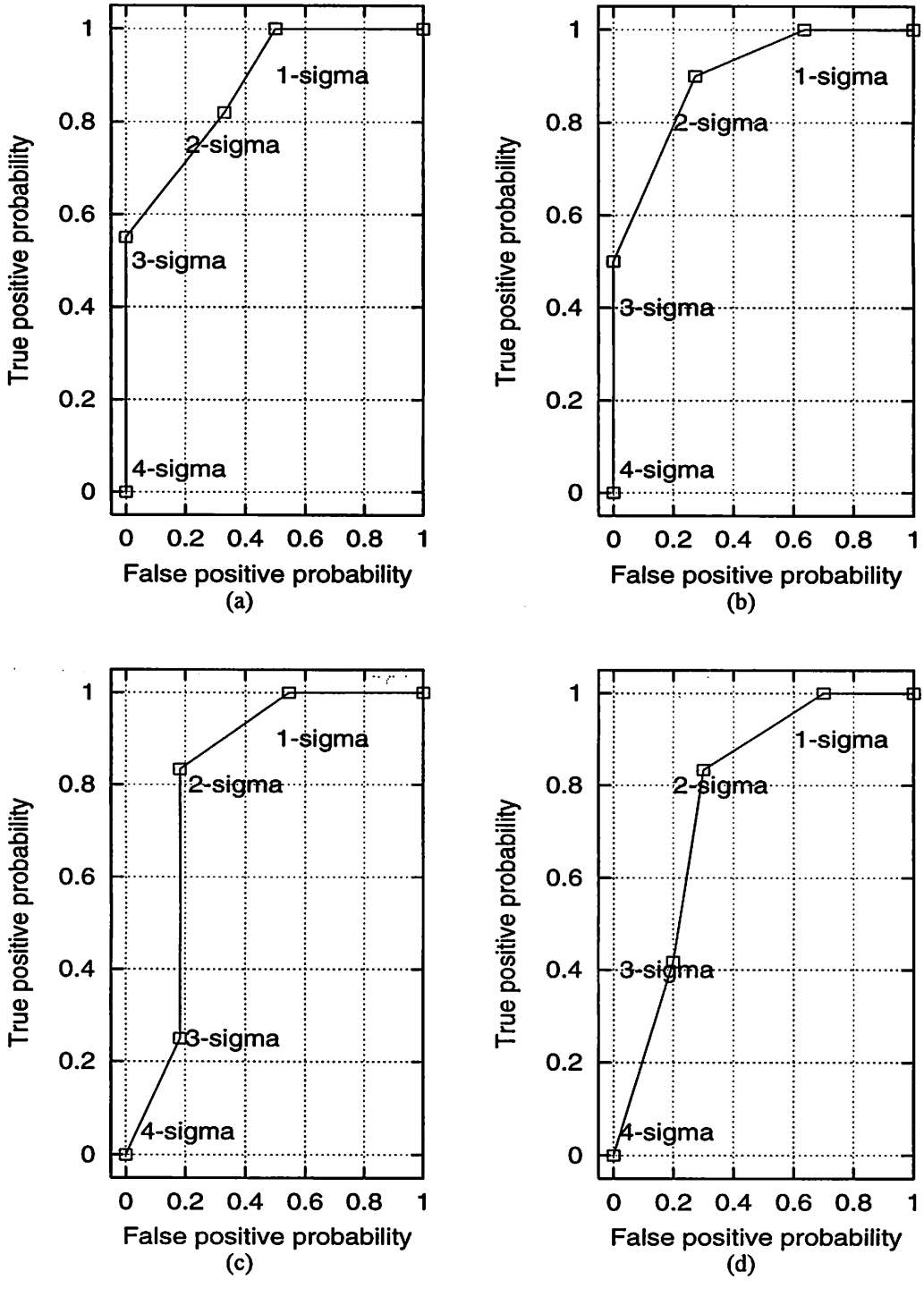

Figure 6.8. ROC curves for the (a) "Stop" sign, (b) "No Parking" sign, (c) concrete slab, and (d) road asphalt. The curves plot the probability of a true positive against the probability of a false positive for confidence intervals of σ, 2σ, 3σ and 4σ. Based on the above curves, a 2σ confidence interval was chosen for all four surfaces.

6.4.2 Brightness constraints

While the benefits of separating effects on brightness from those on normalized color were discussed earlier in the context of the daylight and reflectance models, this section develops a method for utilizing brightness as an additional constraint for classification after the *rgb* color has been estimated. One of the disadvantages of using the *rgb* space is that there is no distinction between surfaces with different brightness values but the same normalized color. For example, in *rgb*, there is no difference between white, black and all grays in between, even though a black (Lambertian) surface will never look white,[31] and a white surface will not look black as long as there is a measurable amount of incident light. Each point in *rgb* corresponds to a line in *RGB*, such that all the points on the line have the same [*R*:*G*:*B*] ratio. Given that under a specific set of illumination and viewing conditions, the apparent color of a surface is a *point* in *RGB* (rather than a *line*), an *rgb* point classified as a target will also represent some points on the corresponding *RGB* line that are *not* from targets. Since all the points along an *RGB* line collapse to a single *rgb* point, these points cannot be differentiated in *rgb*, leading to false positives. Hence, estimates of surface brightness are used as a constraint on the possible *RGB* values of target pixels, after the initial classification in *rgb*. The constraints are based on brightness values from Table 4.1, the Lambertian model, and more samples than are required to derive the NPF. Note that the brightness constraint can be applied only when the local surface orientation is known for the entire surface. While the orientation of a planar surface may be a reasonable input parameter for this method, the entire map of local surface normals for a non-planar surface is not. Hence, the brightness constraint

[31] . . . unless the surface has a strong specular component and is illuminated by "white" light.

can be applied only to planar surfaces. In the case of non-planar surfaces, classification is done in *rgb*, without the brightness constraint.[32] The method is as follows:

1. The brightness entries from Table 4.1 are used, so as to include the mean and standard deviation (V_I and σ_{V_I}, respectively) of the brightness of the incident light under each set of conditions. It is assumed that changes in the brightness of the white surface used for the deriving the daylight model are proportional to corresponding changes in the brightness of the illuminant.

2. In Chapter 5, four samples were used to derive the NPF for the surface. The modified procedure requires an additional 2 samples—one at a relative viewing angle (n) of 0° and the other at one of the non-specular viewing angles (such as 30°). Both of these samples should be under illumination of different brightness from the ones used for estimating the NPF. Hence, at each n, there is one pair of samples of the target surface and a corresponding pair of samples of the white surface. For the pair of samples at $n = 0$, if the brightness values of the target are denoted by V_0 and U_0, and the corresponding values for the white surface denoted by W_0 and Y_0, a brightness reflectance ratio (β_s) for the specular component can be defined as $\frac{V_0 - U_0}{W_0 - Y_0}$. Similarly, from the samples at 30°, the brightness reflectance ratio of the Lambertian component is estimated by $\beta_l = \frac{V_{30} - U_{30}}{W_{30} - Y_{30}}$. Please note that the 7 samples used in our experiments represent the minimum required for the model; while in general it is better to select a larger number of points, we used the minimum required in order to demonstrate that the 7 samples are sufficient.

[32] Although this section does not discuss results of classification for non-planar surfaces, Chapter 6 does.

3. The apparent target color is estimated in *rgb* for the given set of illumination and viewing conditions, based on the method to be described above.

4. Under a given illuminant (with accompanying values of V_I and σ_{V_I}), the brightness of the surface V_s is estimated by ($V_s = V_I \times \beta_s$) if $n = 0$, and ($V_s = V_I \times \beta_l$) if n is in the non-specular range.

5. If the angle of incidence (i) is 0^o, then no brightness falloff function is required, because the brightness of the surface is at its maximum. For all other values of i, the brightness is scaled by the Lambertian falloff function $cos(i)$, resulting in the expected apparent brightness of the surface, V_a.

6. Based on the standard deviation of the illuminant brightness (σ_{V_I}), the confidence interval for V_a is $[V_a - 2\sigma_d\beta_s,\ V_a + 2\sigma_d\beta_s]$ for the specular range, and $[V_a - 2\sigma_d\beta_l,\ V_a + 2\sigma_d\beta_l]$ for the non-specular range.

6.4.3 Results: when the relative viewing angle is known

The above method was tested on the 90 images described earlier in Section 6.2, and the following sections describe the detailed results for each surface. Overall, the average true positives rates were 96.3%, 95.2%, 95.8%, 75.9% and 61.8%, for the matte paper, the "No Parking" sign, the "Stop" sign, the concrete slab and the slab of asphalt, respectively. The corresponding false positive rates were 1.2%, 3.6%, 4.4%, 12.1% and 20.8%. An analysis of the results pertaining to each surface follows.

6.4.3.1 Matte surface

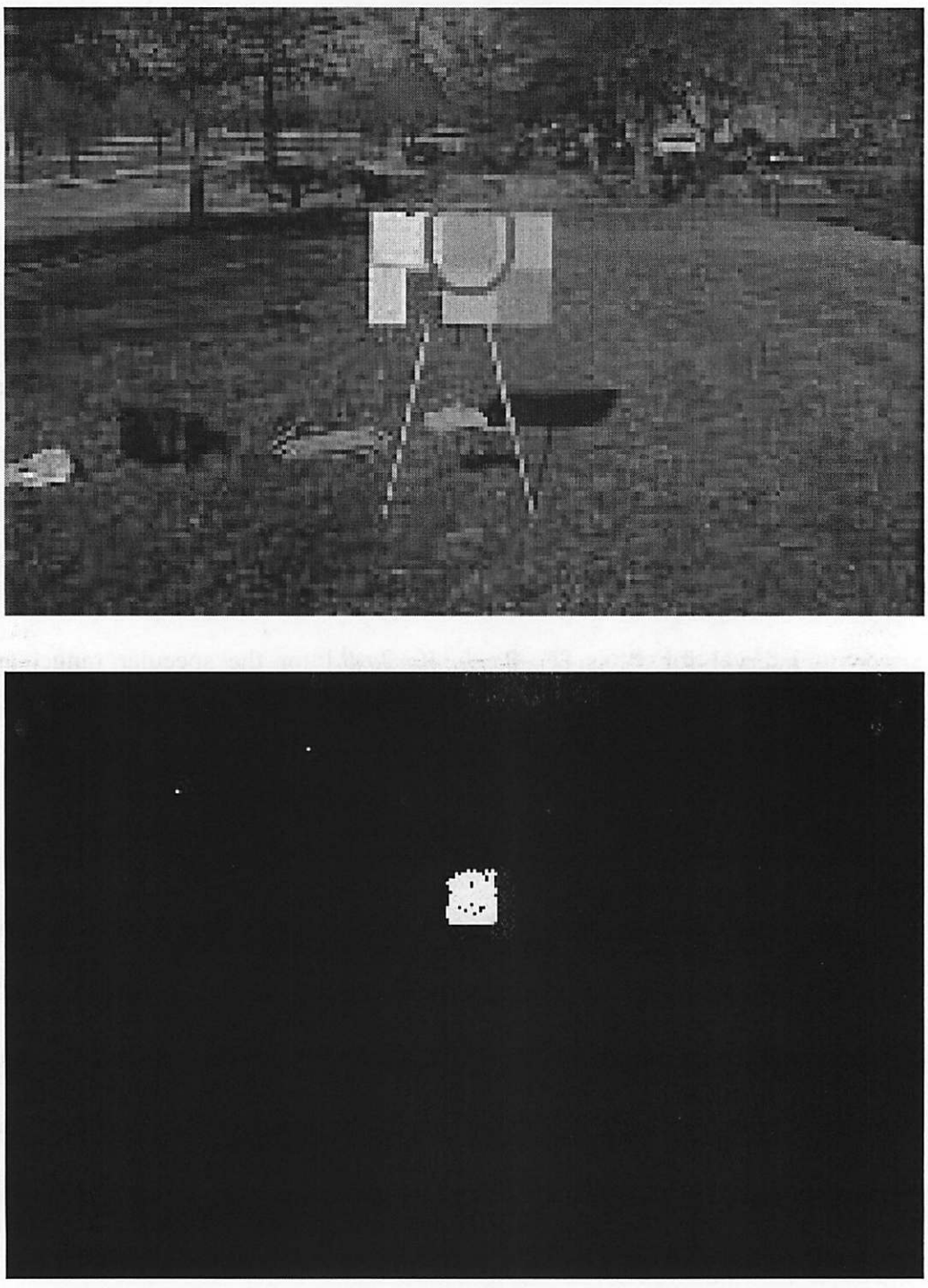

Figure 6.9. Sample results of probability-based classification with a known viewing angle for the matte paper: the true and false positive rates were 96.3% and 1.2%, respectively.

Sun angle	Illumination angle	Viewing angle	% Cloud cover	Sun visibility factor	# Samples	True positive rate	False positive rate
10	0	0	0	1	5	96.5%	1.0%
35	10	0	0	1	4	97.0%	1.4%
50	0	50	80	0	6	96.1%	1.1%
60	180	80	20	1	5	97.4%	4.7%

Table 6.6. Results of probability-based classification for the matte paper, with known relative viewing angle. Four sets of conditions were sampled, with each row describing the sun angle, illumination angle, viewing angle, approximate cloud cover, and the sun visibility factor for the corresponding set of conditions. For each set of conditions, the number of samples are shown, along with the percentage of observations that fell within the estimated confidence interval, and the average error from the estimate.

For the matte surface, tests were conducted on 20 images over 4 sets of conditions (Table 6.6). The true positive classification rate was about 96.3%, with a false positive rate of 1.2% (see Figure 6.9 for a representative sample). The reason for the high true positive classification rate is the low error in estimating the apparent color, and the fact that the Cartesian distance between the observed *rgb* of the surface and that of the other objects in the scene (0.01 for the grass, 0.82 for the leaves and 0.45 the surface in the scene with the closest color) is well outside the 2σ confidence interval. In addition, the surface is matte and its NPF is a straight line. This eliminates dependence on one variable from the problem, namely the relative viewing angle, making the task of estimation easier.

6.4.3.2 "No Parking" sign

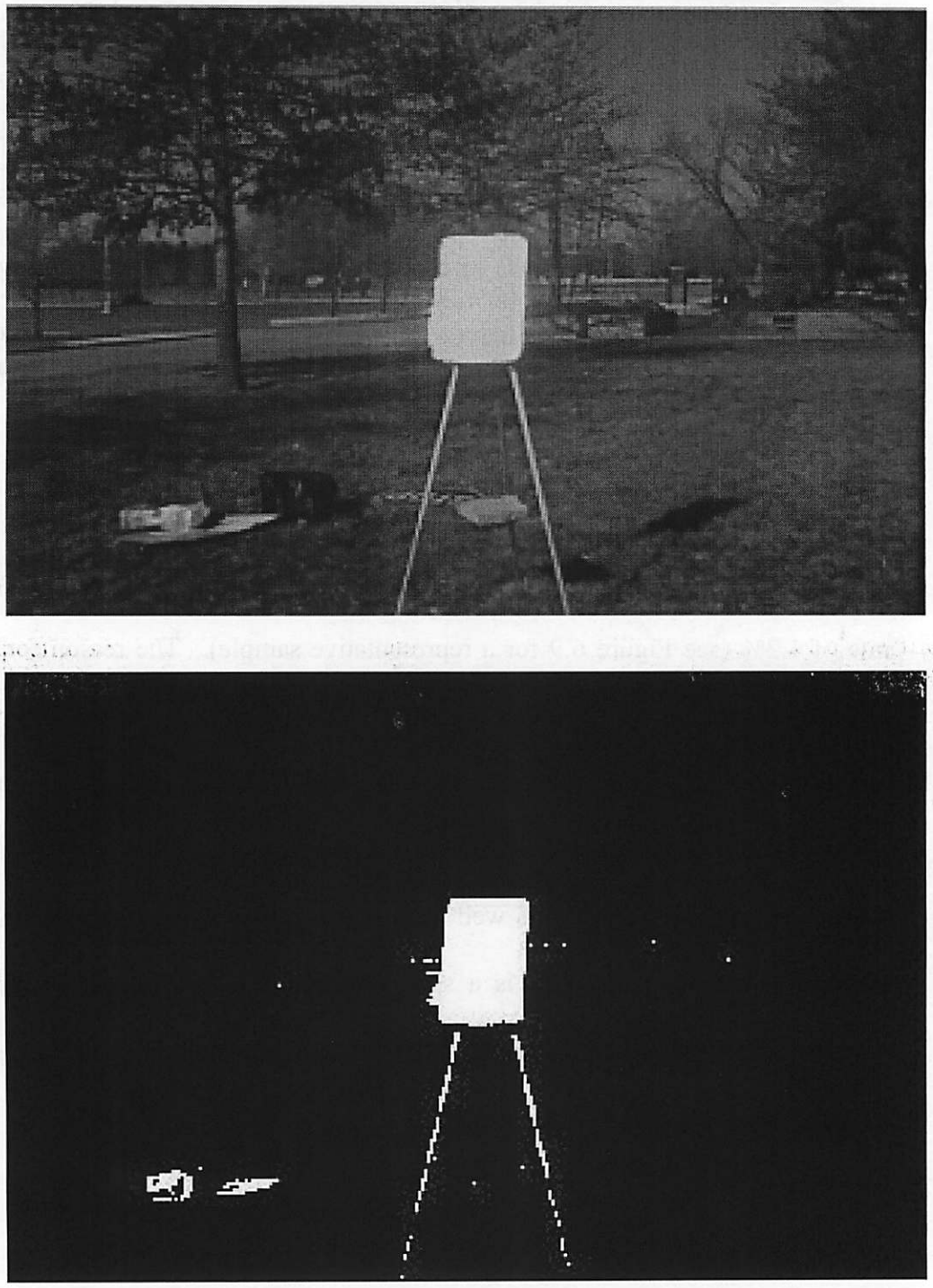

Figure 6.10. Sample results of probability-based classification with a known viewing angle for the "No Parking" sign (specular case): the average true and false positive rates across all samples of the surface were 95.8% and 4.4%, respectively.

Sun angle	Illumination angle	Viewing angle	% Cloud cover	Sun visibility factor	Effect	# Samples	True positive rate	False positive rate
10	0	0	0	1	L	4	92.3%	4.1%
35	20	20	0	1	L	4	91.9%	3.8%
35	20	40	0	1	L	2	91.6%	3.2%
60	0	0	50	0.5	L	4	91.0%	3.6%
60	180	-30	20	1	L	5	92.1%	3.5%
10	0	0	0	1	S	4	97.4%	4.7%
35	20	20	0	1	S	4	90.4%	4.1%
60	0	0	50	0.5	S	4	97.0%	5.6%
10	0	0	0	1	T	4	94.3%	6.2%
35	20	20	0	1	T	4	96.2%	6.8%
60	0	0	50	0.5	T	4	95.3%	5.9%

Table 6.7. Results of probability-based classification for the "No Parking" sign—with known relative viewing angle—over five sets of conditions. Overall, 19 images were sampled out of which 12 exhibited Lambertian, specular and transition effects (shown as L, S and T in the 6th column); the remaining 7 samples exhibited only the Lambertian effect. Note that for the conditions which resulted in all three effects, the results for each effect are in a separate row.

For the "No Parking" sign, the "white" portion of the surface is the considered the target and the lettering is considered background. In tests conducted on 19 images over 5 sets of conditions (Table 6.7), about 97.1% of the target pixels were detected, with a false positive rate of about 5.1% (See Figure 6.10 and Figure 6.11 for sample results). The "No Parking" sign has a strong specular component; hence, two cases arise, depending on the surface orientation. In the first case, the relative viewing angle is in the specular range (entries marked with "S" pixels in Table 6.7, and Figure 6.10). Because of specular effect, almost the entire surface of the sign, including the lettering, is the color of the illuminant. Hence, the target color is the color of the illuminant, which includes pixels from all surfaces exhibiting the specular effect, as well as pixels on surfaces with a neutral albedo (whites and grays). The high true positive classification rate was due to the estimation accuracy. The results in Figure 6.10 also show small clusters of pixels from background objects (e.g., to the left of the easel) that are classified as target pixels.

This is because these objects have neutral albedos and hence also reflect the color of the illuminant. The 2σ confidence interval around the estimated *rgb* value of the target has a small overlap with those for a few neutrally colored surfaces in the scene, thereby causing the false positives. In the second scenario with the "No Parking" sign (represented by the "L" pixel entries in Table 6.7, with a representative sample in Figure **6.11**) a different set of phenomena occur. To begin with, because the relative viewing angle is 20°, there is no specular effect, and the target area of the sign is the color of the Lambertian component. Under those conditions about 91.2% of the pixels defined as targets were within the confidence interval estimated *rgb* value, with a false positive rate was about 3.6%. However, as Figure 6.11 shows, only about half of the actual sign is classified as target. Specifically, there are two portions of the "No Parking" sign that are classified as background: the lettering, and the pixels in the immediate neighborhood of the lettering. The lettering, clearly, is background, and should be classified as such. However, it is less obvious why the pixels neighboring the lettering are classified as background. This occurs due to the mixed-pixel effect that is a consequence of the pixel interpolation process that was discussed in Chapter 2. Because of the pixel interpolation, the color of mixed pixels is somewhere in between the color of the lettering and that of the target area. The mixed pixels were not considered part of the target; if they were, the true positive rate would drop from 91.8% to 83.4% for the non-specular conditions. Even without the specular effect, the albedo of the "No Parking" sign is almost neutral (i.e., white). As with the previous example, some pixels from background concrete and other neutral colored objects are classified as targets.

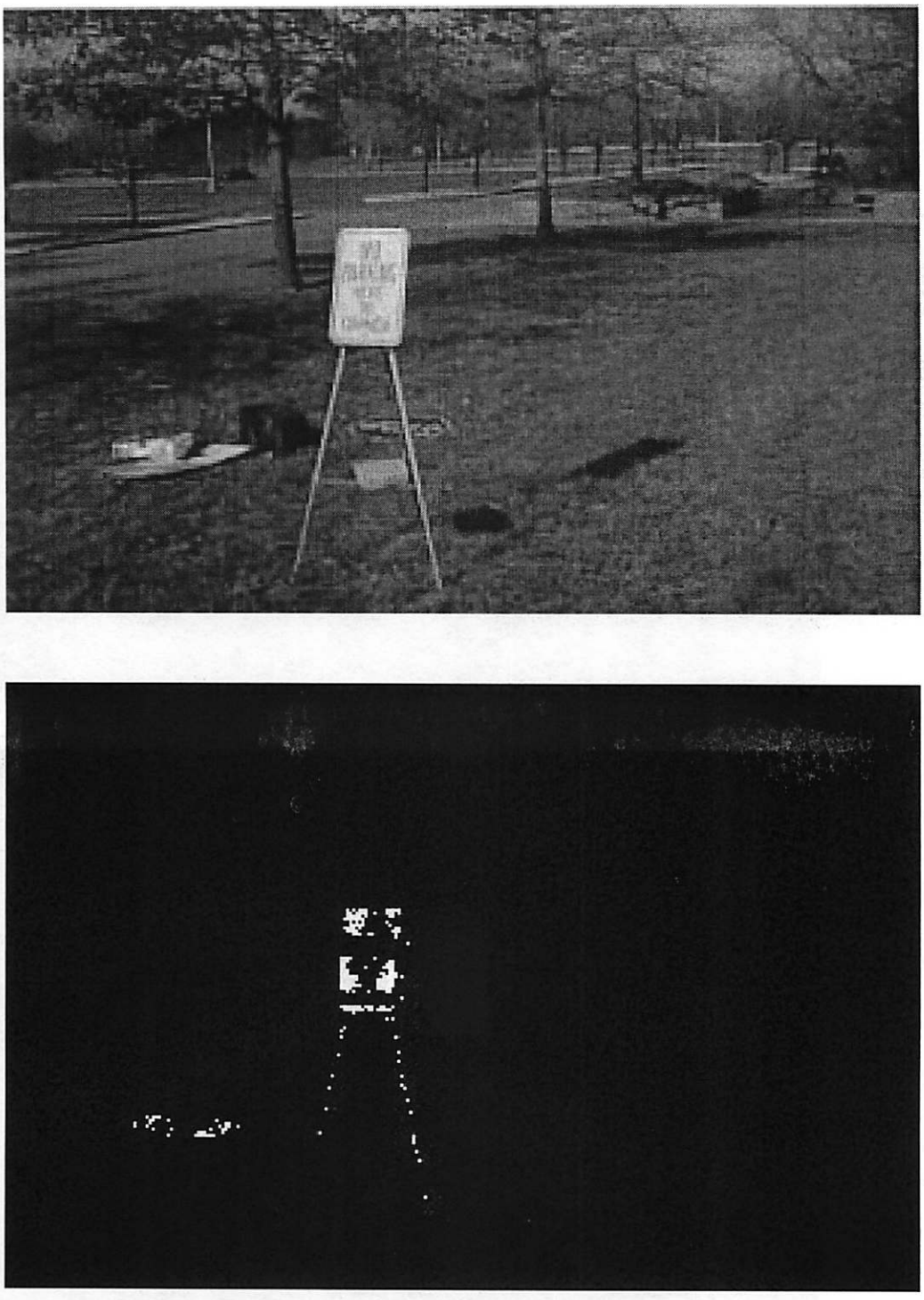

Figure 6.11. Sample results of probability-based classification with a known viewing angle for the "No Parking" sign (non-specular case): the true and false positive rates were 95.8% and 4.4%, respectively.

6.4.3.3 "Stop" sign

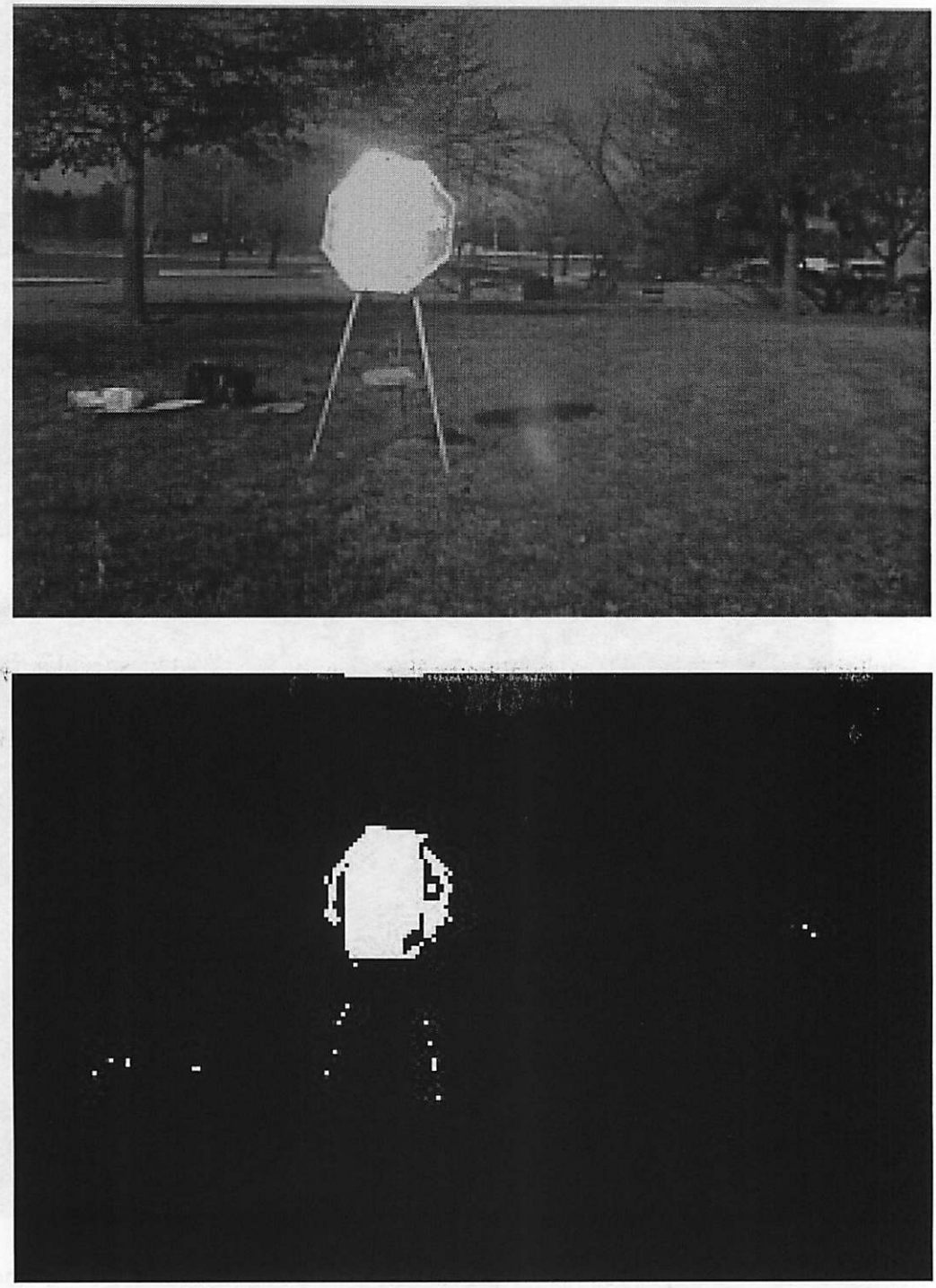

Figure 6.12. Sample results of probability-based classification with a known viewing angle for the "Stop" sign: the true and false positive rates were 95.2% and 3.6%, respectively.

For the "Stop" sign, the "red" portion of the surface is considered the target area, and the white lettering and border are considered background; as with the "No Parking" sign, the "Stop" sign is also specular. In tests conducted on 19 images of the "Stop" sign, about 95.8% of the target pixels were correctly classified, with a false positive rate of about 4.4% (See Table 6.8). The false negatives occur because of two reasons: the first is the mixed pixel effect described above, which accounts for about 20% of the false negatives. The second reason is the classification method assumes that if one target pixel in a given column is in the specular range, then all other target pixels in that column will also be in the specular range (refer to Section 6.2.2); this assumption does not account for the fact that the sun is (for all practical purposes) round, and hence the region on the target representing the specular peak will be circular. This means that just as changes in column numbers affects whether or not a pixel will be in the specular range, so will changes in the row number; this phenomenon is not accounted for by the NPF-based classifier. Most of the false positives, as in the case of the "No Parking" sign, occurred in images with the specular effect, from areas with neutral albedos (such as concrete and the white lettering and border). One noticeable phenomenon in the results for the "Stop" sign from Figure 6.12 is that only the middle portion of the target surface reflects the color of the illuminant, while the rest is the characteristic "red". The "red" of the Lambertian component was distinct in that there was no overlap between the confidence interval around its estimated *rgb*; as a result, the true positive rate was high and the false positive rate was low for that portion of the surface. At the same time, there were very few neutral-colored or specular surfaces in the same range of columns as the specular portion of the "Stop" sign, which also contributed to the low false positive rate.

However, there were some false negatives from the portion of the surface at the transition between the regions representing the specular peak and the Lambertian component. This was partially due to the mixed pixel effect.

Sun angle	Illumination angle	Viewing angle	% Cloud cover	Sun visibility factor	Effect	# Samples	True positive rate	False positive rate
10	0	0	0	1	L	5	94.5%	4.9%
35	30	30	0	1	L	3	93.8%	5.0%
35	20	40	0	1	L	2	96.7%	5.1%
60	0	0	50	0.5	L	4	95.2%	5.6%
60	180	-30	20	1	L	5	95.4%	4.7%
10	0	0	0	1	S	5	81.6%	8.4%
35	30	30	0	1	S	3	97.1%	4.2%
60	0	0	50	0.5	S	4	84.0%	5.1%
10	0	0	0	1	T	5	85.2%	4.8%
35	30	30	0	1	T	3	87.1%	5.2%
60	0	0	50	0.5	T	4	89.6%	4.9%

Table 6.8. Results of probability-based classification for the "Stop" sign—with known relative viewing angle—over five sets of conditions. Overall, 19 images were sampled out of which 12 exhibited Lambertian, specular and transition effects (shown as L, S and T in the 6th column); the remaining 7 samples exhibited only the Lambertian effect. Note that for the conditions which resulted in all three effects, the results for each effect are in a separate row.

6.4.3.4 Concrete slab

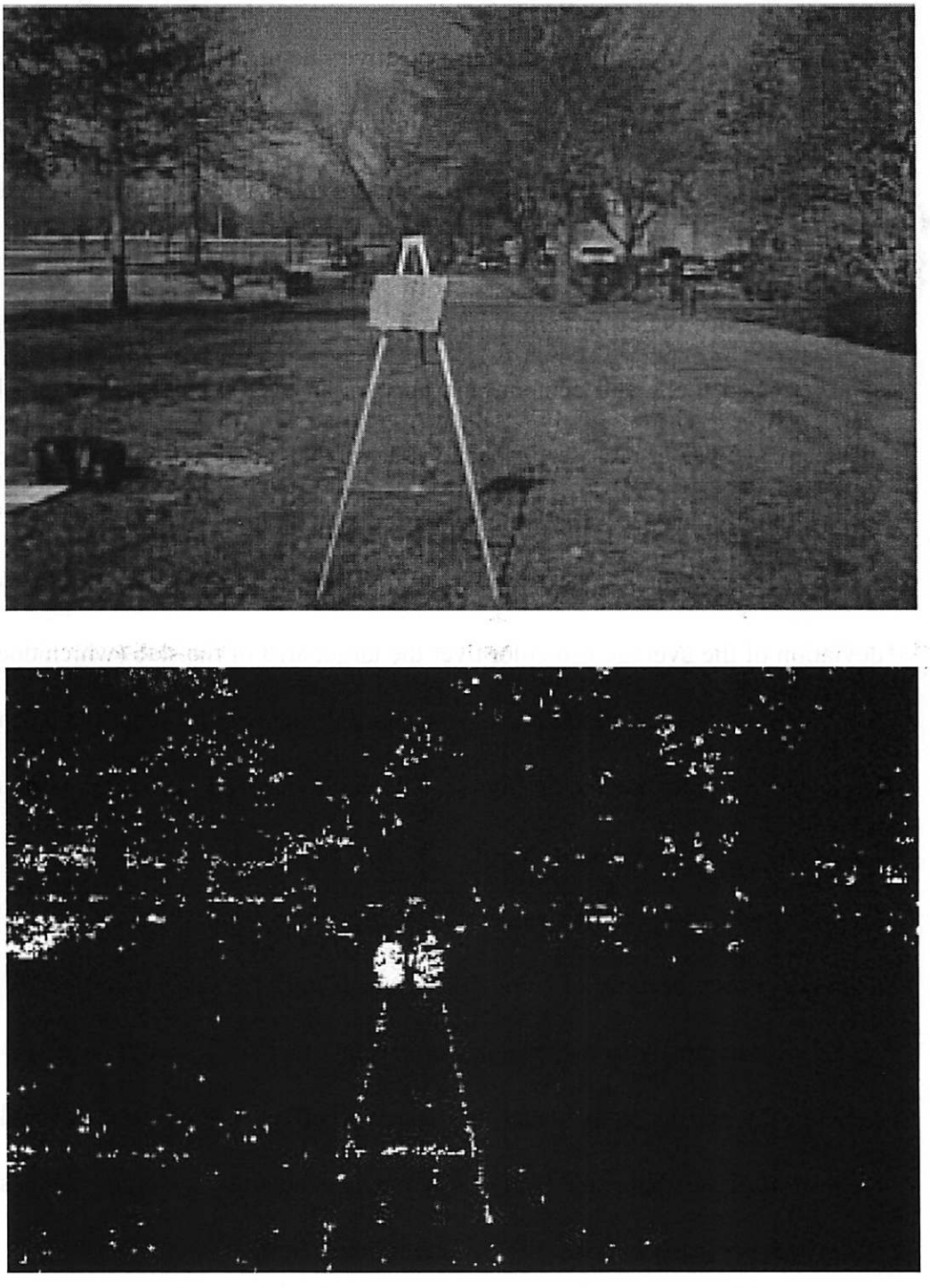

Figure 6.13. Sample results of probability-based classification with a known viewing angle for the concrete slab: the true and false positive rates were 75.9% and 12.1%, respectively.

The percentage of correctly classified pixels for the concrete slab was about 75.9%—considerably lower than that for the matte surface and the traffic signs (See Figure 6.13 and Table 6.9). In addition, the false positive rate at the pixel level was higher: 12.1%. The concrete slab in the figure is not uniformly colored, but has a vertical strip in the middle that is a slightly different color, which explains the region in the middle classified as non-target. One reason for the lower true positive classification rate is that the concrete surface is not uniformly colored. It is a mixture of various substances such as sand, crushed rocks and cement, and appears an even "gray" at a macro level (from a distance). However a closer inspection shows that small portions of the concrete (at the level of individual or small clusters of pixels in the image) have the color of the constituent material used to form the concrete. This is because of the high standard deviation of the average *rgb* color over the target area of the slab (which does not include the vertical strip in the middle). The standard deviation was about three times that of the matte surface and the traffic signs. The high standard deviation results in a higher probability of classification error. At the same time, the confidence intervals for estimated and observed *rgb* values of the target only partially overlapped. The concrete slab was chosen because of its neutral "grayish" albedo, and the number of false positive objects is due mostly to the presence of several other surfaces of neutral color. As in the case of the traffic signs under the specular effect, color-neutrality makes detection difficult because there are likely to be several neutrally colored surfaces in a typical outdoor scene (such as concrete, pavement, road, etc.).

The examples of the traffic signs and the concrete surface illustrate another phenomenon common to neutral colored surfaces and to surfaces with strong specular

components. This effect can be understood by imagining the *rgb* normalized dichromatic lines for a number of surfaces, some specular and some neutral colored. All these lines coincide at the illuminant point, making that part of the color space very ambiguous for recognition. In other words, pixels in that part of color space could belong to any of a number of (specular or neutral-colored) surfaces in the scene. Lee [46] describes a number of examples such surfaces, along with their reflectances in normalized color space.

Sun angle	Illumination angle	Viewing angle	% Cloud cover	Sun visibility factor	# Samples	True positive rate	False positive rate
10	0	0	0	1	4	84.0%	12.0%
35	10	0	0	1	4	76.1%	9.7%
50	0	50	80	0	4	68.5%	4.9%
60	180	80	20	1	4	76.2%	11.2%

Table 6.9. Results of probability-based classification for the concrete slab. Four sets of conditions were sampled over 16 images.

6.4.3.5 Road asphalt

Sun angle	Illumination angle	Viewing angle	% Cloud cover	Sun visibility factor	# Samples	True positive rate	False positive rate
10	0	0	0	1	4	54.8%	24.0%
35	10	0	0	1	4	62.1%	27.1%
50	0	50	80	0	4	71.1%	19.6%
60	180	80	20	1	4	62.4%	13.8%

Table 6.10. Results of probability-based classification for the slab of road asphalt. Four sets of conditions were sampled over 16 images.

The results from the slab of road asphalt were worse than those for the concrete slab—only 61.8% of the target pixels were correctly classified, with a false positive rate of 20.8% (See Table 6.10 and Figure 6.14). The reasons for the poor performance are more extreme cases of the same factors affecting the concrete slab. To begin with, the road surface is not uniformly colored, has the average *rgb* value is accompanied by a very

high standard deviation (0.012), leading to a larger confidence interval and consequently higher classification errors, both in terms of false negatives and false positives. Second, road asphalt is neutral colored, leading to a high false positive rate at the object level. The examples of the road surface and the concrete slab show that for neutral colors, there is so little color information that color may not be a good feature for recognition.

6.4.4 Results: when the relative viewing angle is not known

In the absence of knowledge about the relative viewing angle, the only surfaces affected are those with a specular content, i.e., the traffic signs. As in Section 6.3, the only difference is that classification is done based on the entire dichromatic line and the corresponding confidence interval, rather than a point. For the "No Parking" sign, the average true positive rate was about 95.3%, with an average false positive rate of about 7.4% (Figure 6.15). For the "Stop" sign, the corresponding rates were 97.1% and 10.8%, respectively (Figure 6.16). Typically, the false positive rates will tend to be higher when the viewing angle is not used, because targets are classified from a larger portion of the color space. In addition, when the viewing angle is not known, the NPF cannot be used to determine which target pixels will be specular and which non-specular; hence all pixels are classified based on the dichromatic line, further increasing the likelihood of false positives. However, the true positive rate should be at least as high, because the target region in *rgb* does not get smaller.

The methods discussed in this section have been tested on images from two outdoor applications: road/lane detection for automotive applications, and color-based focus-of-attention for objects detection. These results are discussed in Chapter 7.

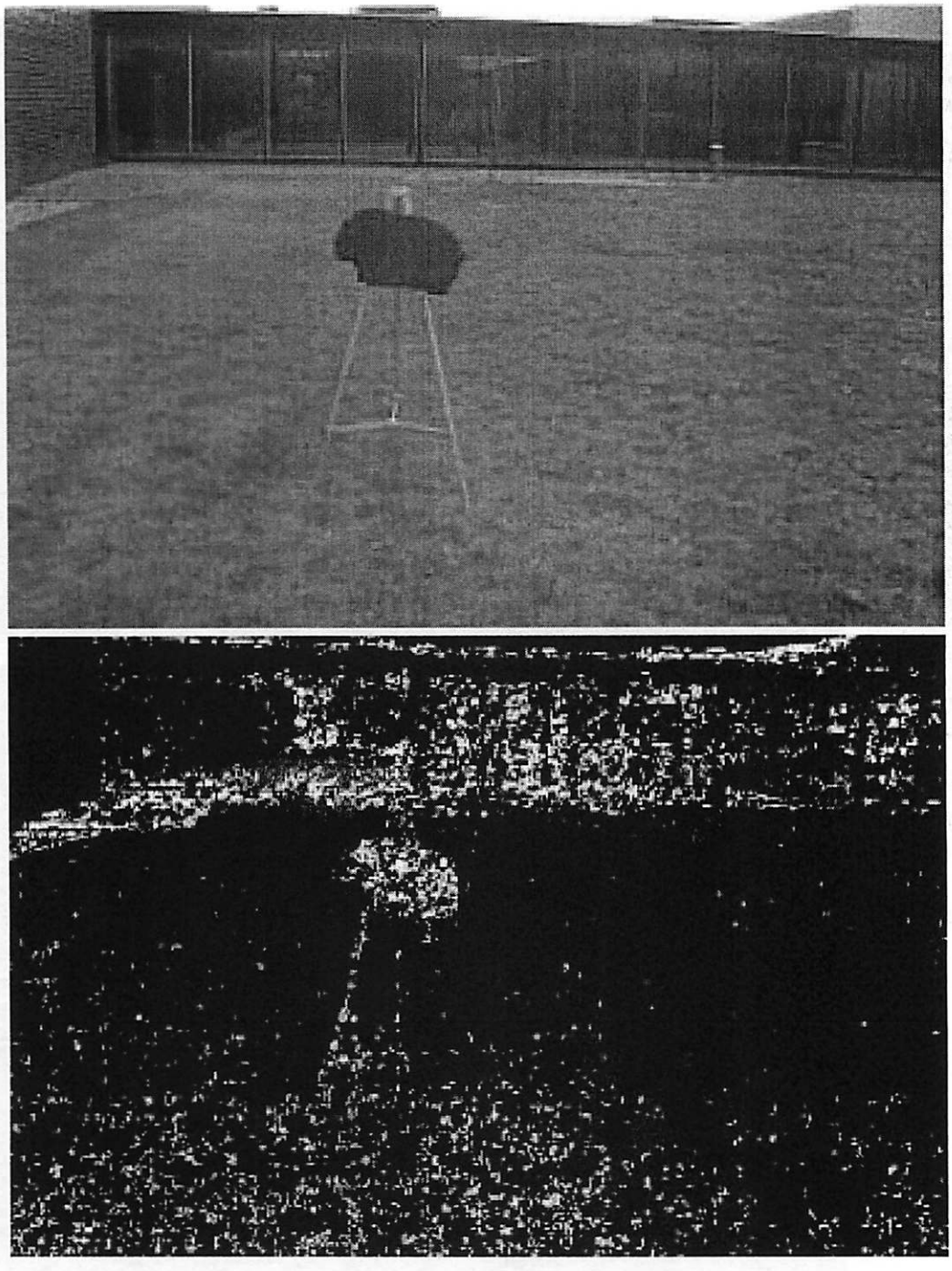

Figure 6.14. Sample results of probability-based classification with a known viewing angle for the slab of road asphalt: the true and false positive rates were 61.8% and 20.8%, respectively.

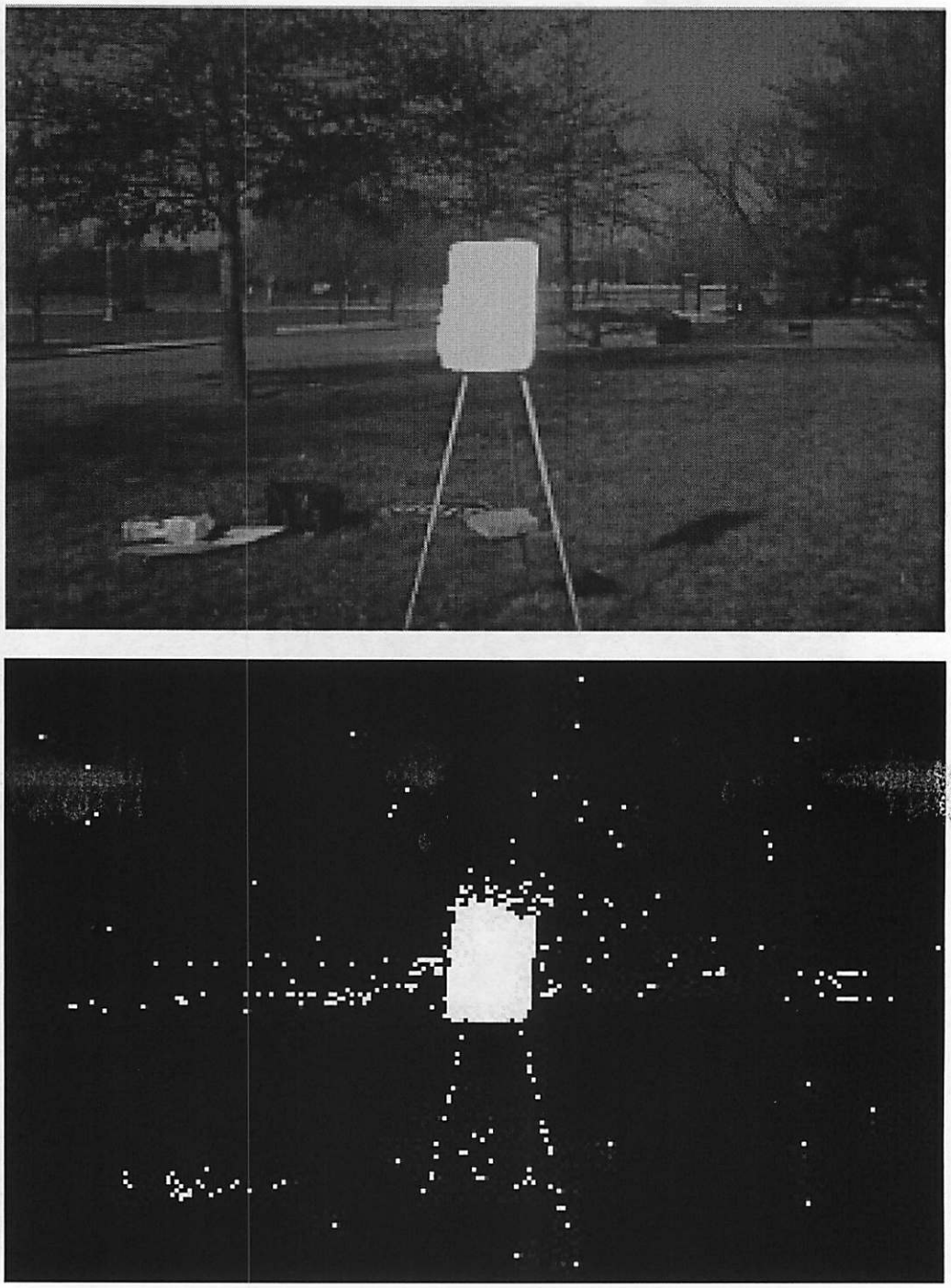

Figure 6.15. Results of probability-based classification without knowledge of the relative viewing angle for the "No Parking" sign.

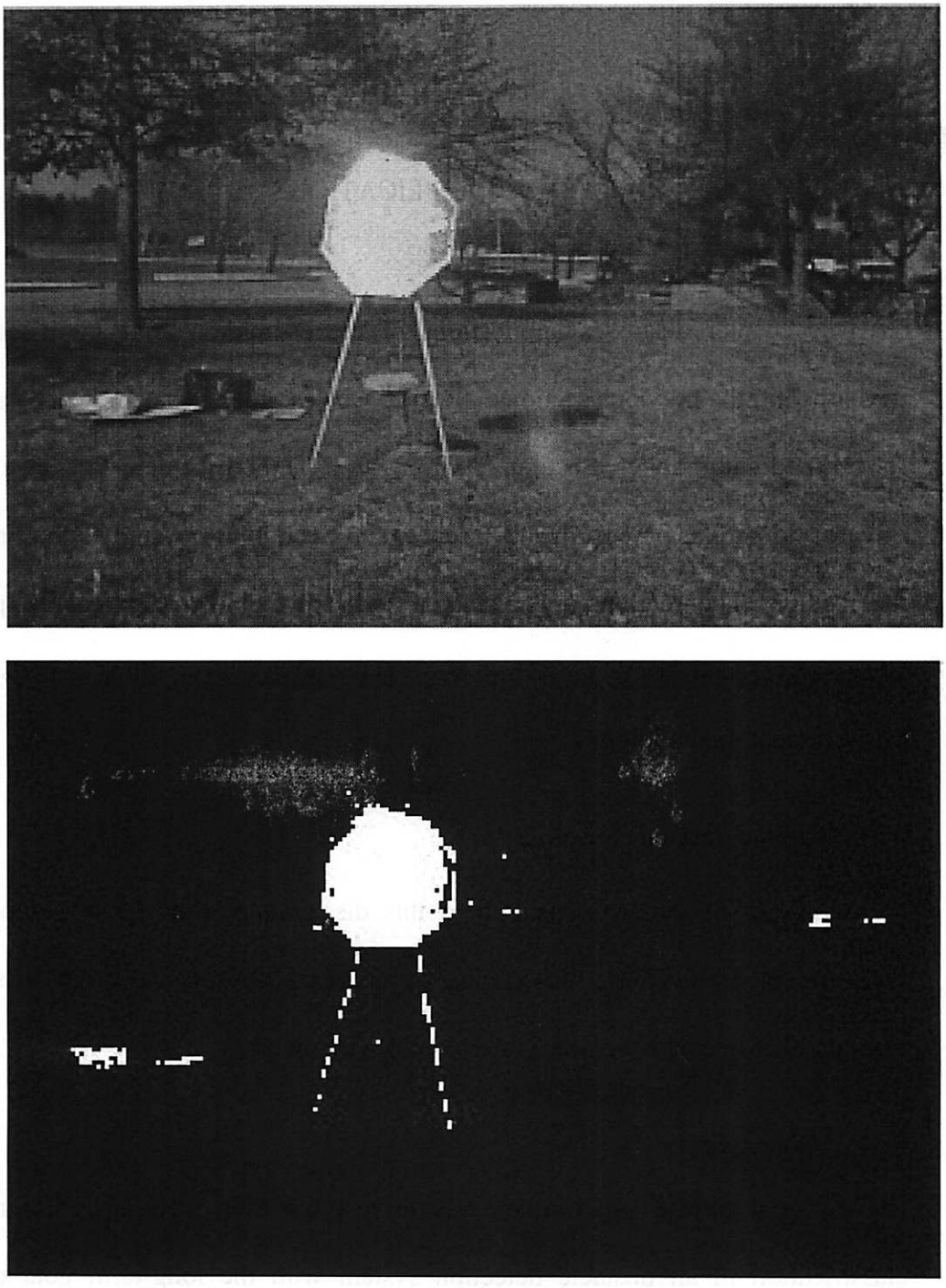

Figure 6.16. Results of probability-based classification without knowledge of the relative viewing angle for the "Stop" sign.

CHAPTER 7

APPLICATIONS

7.1 Overview

This chapter discusses applications of the estimation and classification methods developed in the previous sections. Section 7.2 describes a system for obstacle detection for on-road automobiles, Section 7.3 discusses a method for detecting specific instances of cars and similar objects in road scenes, and Section 7.4 examines the implications of the results. The sections specifically describe the objective of each experiment, the methodology and setup used, and the results/observations from the tests (including measurement methodology).

7.2 On-road obstacle detection

As a part of the work leading to this dissertation, tests were conducted on data collected in 1996-97 for developing color-based obstacle detection systems in the National Automated Highway System (NAHS) project.

7.2.1 Objective

The goal of the experiments was to test the effectiveness of color-based pixel classification in an obstacle detection system with the long-term goal of eventually combining a suite of sensors and systems. The set of tests described were intended to test how NPF-based classification would be able to recognize pixels that belonged to the road surface and distinguish them from pixels from non-asphalt areas of the road (which are presumably from potential obstacles). The system was biased towards being

conservative—i.e., avoiding false negatives at the risk of detecting more false positives or false alarms—due to the nature of the application (obstacle detection for domestic automobiles).

7.2.2 Methodology and setup

The method consisted of four steps: collecting the training data, collecting the test data, classifying pixels, and using region-level logic with along with an external system [74] to identify potential obstacles. To begin with, the surface reflectance parameters were estimated from six randomly chosen training images (which, the reader may recall from the discussion in Sections 5.4.1 and 6.4.2, is the minimum number of images required to estimate the color-coefficient matrix and NPF). The data was collected using the same Kodak digital camera used in the experiments in the previous sections; the camera was mounted on the inside of a car on a fixed platform that was parallel to the longitudinal axis of the car. The car was driven along a stretch of road on a test-track belonging to an automobile manufacturing firm.[33]

The test data consisted of 5 sets of 25 images (for a total of 125) of a single stretch of road, with the illumination conditions recorded. These five sets were collected over five types of conditions (see Table 7.1): a clear morning (sun-angle 15°, cloud cover 0-5%), a clear afternoon (sun-angle 45°, cloud cover 0-5%), a clear afternoon (sun-angle 50°, cloud cover 0-5%), a cloudy evening (sun-angle 15°, cloud cover 60-70%, sun visibility factor 0), and a cloudy morning (sun-angle 20°, cloud cover 60-70%, sun-visibility factor 0). The road surface in these images is locally horizontal with respect to the camera, so that the viewing geometry is different for different parts of the road. However, since the

[33] The firm wishes to remain anonymous.

road surface does not have a strong specular component (i.e., since it has a flat NPF), the change in viewing geometry does not change the apparent color of the different parts of the road. When the sun-visibility factor was non-zero (i.e., in the first, second and third image sets), it was assumed that the light incident upon the surface was the color of sunlight (as described in Table 4.1). Figure 7.1(a) shows a sample from the test set—as the figure shows, the lane markers are clearly visible, and the lane is free of potholes. What is less evident from the image is that there are occasional tire skid marks, oil patches, and smudges from repeated painting of the right lane-marker. Four objects (a car tire, a traffic cone, a cardboard box, and a nondescript piece of debris) were chosen as obstacles and manually scattered over different, random parts of the road. Across the 125 images, there were 178 instances of obstacles. Figure 7.1(a) shows a single obstacle (the nondescript piece of debris) about 60 feet in front of the car/camera.

Using the classification described in the previous chapter, the pixels in all 125 images were classified into target and background classes. The output of this step is a set of binary images. Figure 7.1(b) shows result from classifying the sample image in Figure **7.1**(a). As the figure shows, there are a non-trivial number of false negatives as well as false positives; details of the classification results will be discussed in the next section. The logic used by the system was that any pixel that is not the color of the road is a potential obstacle.

In order to detect obstacles at the region level, the lane-markers are first extracted from the original color image using the intensity-profiling algorithm in the RALPH road-follower [74]. Based on the lane-extraction, a triangular region is generated for the lane occupied by the vehicle, stretching from the vanishing point to the part of the road just

before the vehicle. Note that for roads with curves, the RALPH algorithm "straightens" the lanes by pixel-wise shifting of rows, so that the triangular region can still be fitted; Figure 7.2(a) shows the triangular region extracted for the sample image. This process considerably reduces the size of the search area, thereby voiding the impact of any errors in color-based pixel classification outside the road area. Note also that pixels on the lane-markers are themselves kept outside the triangle, removing them from the search window. A 10×5 search window was used at the apex of the triangle, and any search window with more that 10% (an empirically chosen number) non-road pixels was marked as an obstacle. The size of the search window was gradually increased as the area being searched approached the base of the triangle; the magnitude of the increase (15% per iteration) was based on empirical measurements of loom (i.e., actual measurements of how objects increased in size in the image as the approached the camera). Figure 7.2(b) shows a sample result after extracting the obstacles using this technique—the obstacle is detected, but so is one false positive. Evident in the figure is that most of the incorrectly classified pixels within the search window did not result in errors at the region level because of the size of the search window. However, the large number of positive pixels near the bottom right corner of the search window (which were caused by minor "smudging" of the lane marker during maintenance) caused the false positive shown in the figure.

7.2.3 Results and observations

The performance of the system was evaluated at two levels: pixel level and region level. At the pixel level, there are two measures of performance—the true positive rate (which measures the percentage of non-road/obstacle pixels correctly identified), and the

false positive rate (which measures the percentage of road pixels identified as non-road). Over the 125 images, the average estimation error (measuring the *rgb* distance between with estimated and true colors under each set of conditions) was 0.013. The true and false positive rates were determined by extracting road and non-road pixels from each image[34] and counting the actual number of correctly and incorrectly classified pixels. The pixel-level true positive rate was 76% (i.e., the false negative rate was 24%), with a 19% false positive rate. Of the 24% false-negative pixels, a substantial number (about 90%) were from the tire that was used as a sample obstacle (which is also black, the color of the road). Out of the false positive pixels about 95% were from discolorations on the road (specifically, oil patches, tire skid marks, road wear patches and shadows).

At the region level, the two measures of performance are the true positive rate (number of *full obstacles* identified) and the false positive rate (number of *full obstacles* missed). Note that the impact of pixel-level errors on region-level performance is minimized by limiting the search area to the extracted triangle, and by applying loom-based logic, which assumes that objects get larger as they approach the camera. Over the 125 images, 171 of the 178 obstacles were detected; the 7 obstacles that were undetected were instances of the tire (which is the same color as the road). In addition, 107 regions of the actual road were falsely identified as obstacles; these were all from the discolorations due to tire skid-marks, road wear, shadows and oil. As mentioned earlier, the high false positive number is the consequence of the conservative threshold (the

[34] Pixels were extracted by drawing boxes (rectangular area provide a simple means for iterative region-extraction) around clusters of pixels and cropping them from the rest of the image. Because not all regions are rectangular (e.g., some obstacles are cones), only about 95% of the total pixels were actually evaluated.

reader may remember that any region with more that 10% non-road pixels is classified as a potential obstacle).

Sun angle	% Cloud cover	Sun visibility factor	Pixel true positive rate	Pixel false positive rate	Region true positive rate	# region false positives
15	0-5%	1	74%	17%	94%	20
45	0-5%	1	78%	19%	95%	23
50	0-5%	1	72%	16%	97%	24
15	60-70%	0	79%	20%	100%	19
20	60-70%	0	75%	21%	94%	21

Table 7.1. Results from NPF-based classification for road/obstacle detection. For each of the 5 test conditions, 25 images were sampled (for a total of 125 images). The table shows the true positive rate (76% overall) and false positive rate (19%) at the pixel-level for each set of conditions, along with the percentage of actual obstacles detected (96%, 171 out of 178) and the number false positives at the region-level (i.e., the number of times the obstacle detection system would have set off a false alarm, which occurred on the average 0.86 times per image).

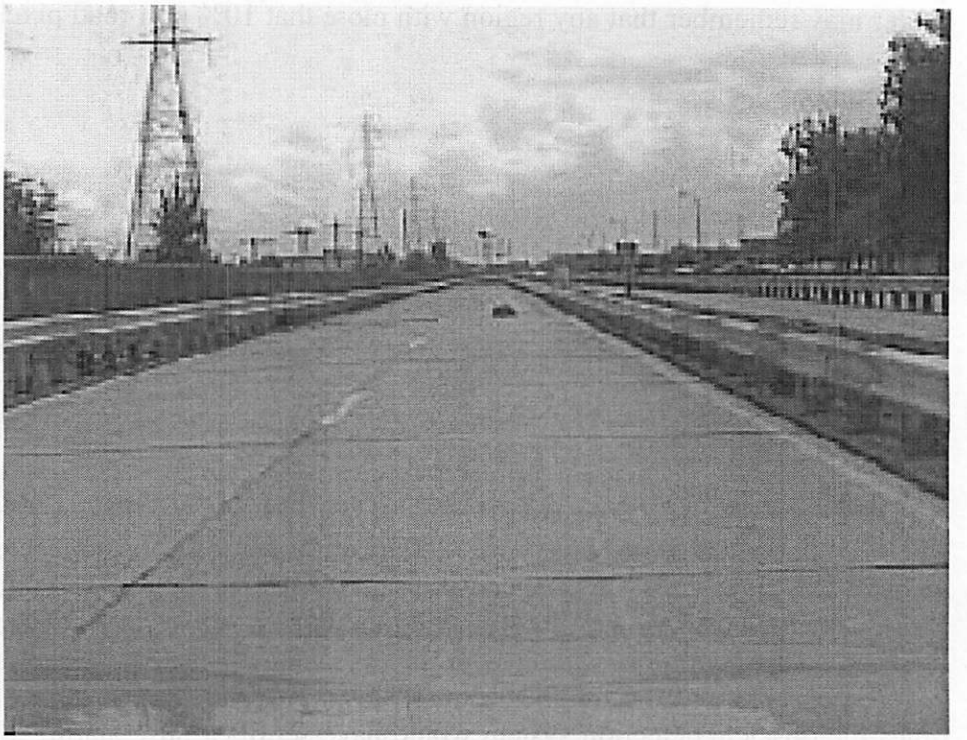

(a) Original color image

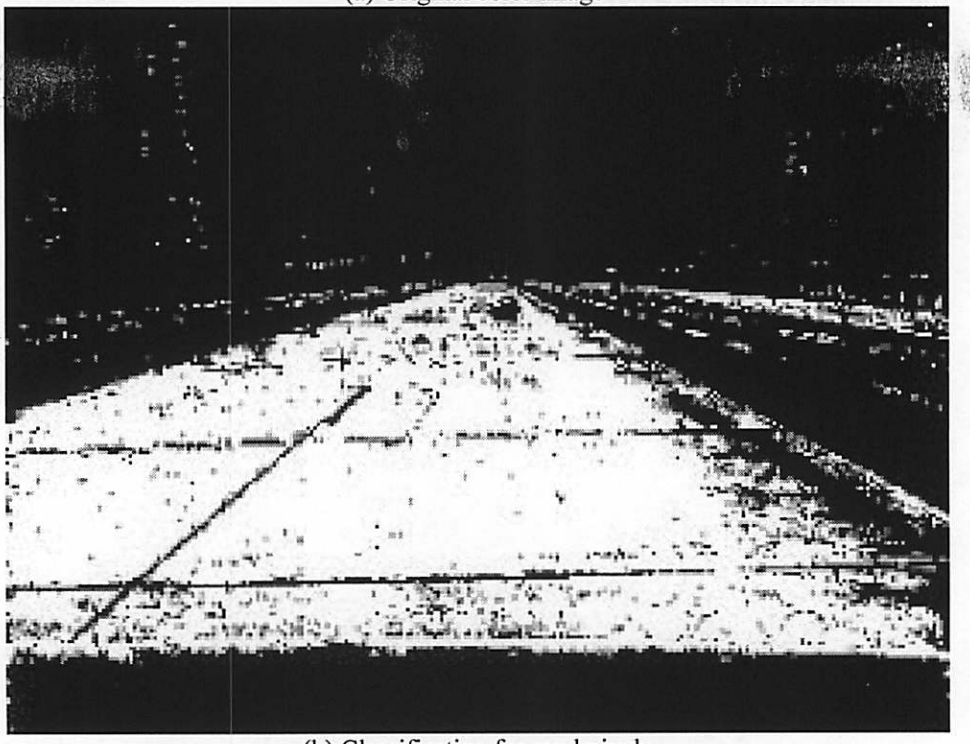

(b) Classification for road pixels

Figure 7.1. Sample results from color-based classification used in conjunction with an external lane-extraction system: (a) original color image; (b) classification for road pixels.

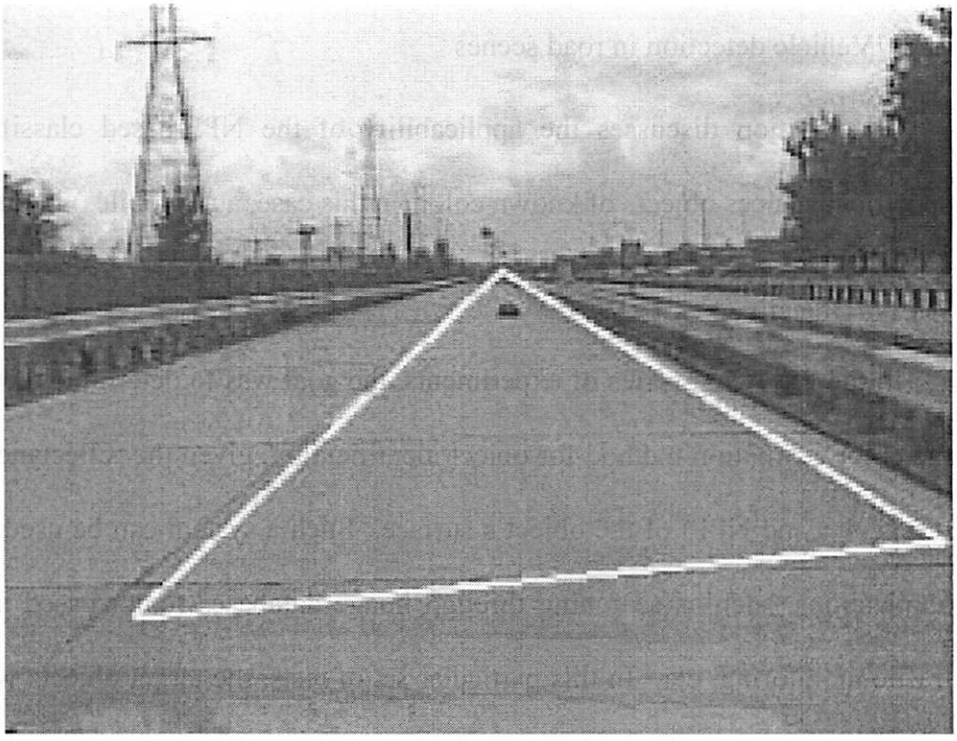

(a) Lanes extracted using an external system

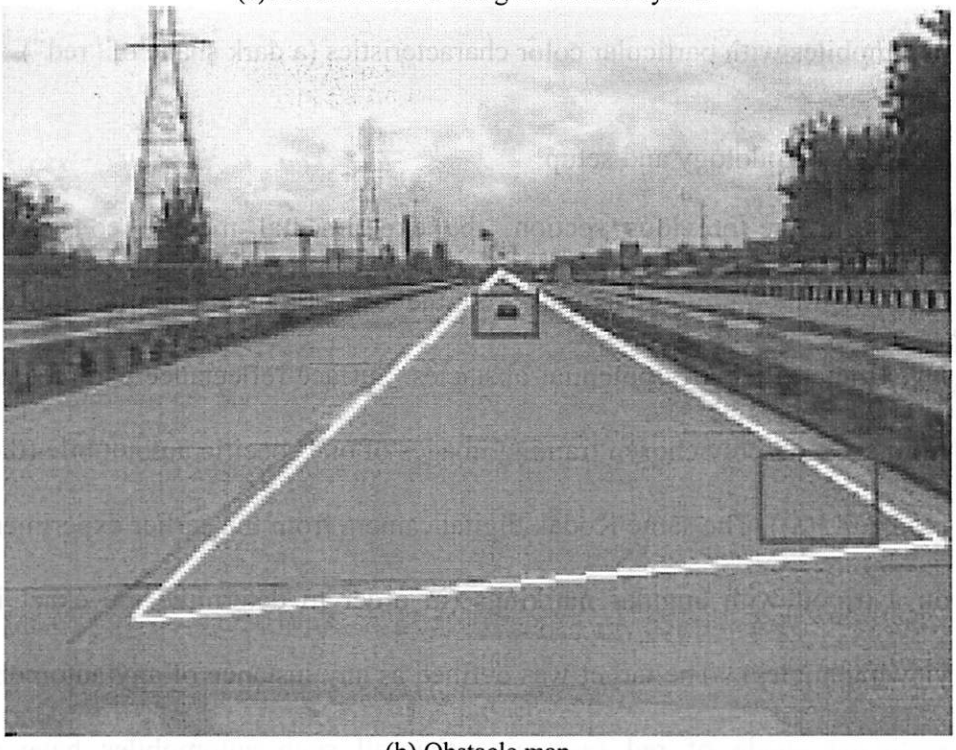

(b) Obstacle map

Figure 7.2. Sample results from color-based classification used with an external lane-extraction system: (a) triangular search regions after lane-extraction; (b) extracted obstacles: one true obstacle and one false positive.

7.3 Vehicle detection in road scenes

This section discusses the applicability of the NPF-based classifier in detecting specific instances objects of known color (in this case, automobiles) in outdoor scenes.

7.3.1 Objective

In the following series of experiments, the goal was to determine the effectiveness of the color estimation method for object identification, given the reflectance characteristics (i.e., color and NPF) of the object's surface. Such a system can be used for a number of applications, such as searching through image databases (color-based image indexing), traffic monitoring, etc. In this particular set of tests, the target objects were automobiles (a car and a pickup truck), and the methods were used to identify instances of automobiles with particular color characteristics (a dark shade of "red").

7.3.2 Methodology and setup

As in the previous section, the experimental method consisted of four steps: collecting the training data, collecting the test data, pixel classification, and using region-level logic to identify potential obstacles. Surface reflectance parameters were estimated from six randomly chosen training images of one specific automobile (the truck shown in Figure 7.3(a)). The same Kodak digital camera from the earlier experiments was mounted on a tripod with angular markings (in order to determine the exact illumination and viewing angles). The target was defined as any instance of any automobile that is of the particular shade of red (assuming that all such automobiles have similar specular characteristics).[35] In other words, the training data was obtained from a single vehicle,

[35] This assumption might not hold for older automobiles with faded paint.

with the aim of detecting all vehicles in that have similar reflectance characteristics—the reason being that even over a large set of images, only a small amount of training data may be available. A total of 50 test images were collected, consisting of 10 images each under 5 sets of conditions (see Table 7.2): a clear sky at 10° and 30° sun angles, and an overcast sky at sun angles of 10°, 30°, and 50° (in dry and snowy conditions). All the images were from the same parking lot over the course of 10 days; hence many of the same automobiles were present in all the images. Figure 7.3 shows two of the sample test images—in these images, there are two instances of potential target vehicle (shown in ellipses). Across the 50 images, there were exactly 50 instances of 3 target automobiles. In other words, there were only 3 red automobiles in the set of images, which collectively appear 50 times in the 50 images (some images had more than one target, while some others had none). The figure also shows that there is red-brick building in the background, which looks very similar in color to the red vehicles. That background was chosen intentionally, in order to test the effectiveness of the method in distinguishing between subtle shades of the same general hue. In addition, the tail-lights of all the vehicles shown in the figure are also of similar color.

As with the traffic signs discussed in the previous chapter, when direct sunlight is incident upon the specular vehicle surface, a portion of the surface reflects the direct sunlight, but the rest of the surface is still the characteristic "red" of the Lambertian component. In order to deal with this problem, when the incident light was direct sunlight and the relative viewing angle was 0° (for at least a portion of the target), both the color of the sunlight and the apparent color of the Lambertian component were

considered target colors.[36] In addition, since the surface of the vehicle is typically non-planar, local surface brightness cannot be used; hence classification was done in the *rgb* space. Figure 7.4 shows the binary images which resulted from classifying the images in Figure 7.3. As the images show, a number of the pixels from the red-brick building and car tail-lights were classified as targets (the next section will discuss the results in greater detail).

After pixel classification, a standard boundary following algorithm [3] was used to determine the (rectangular) size of pixel-clusters that were classified as target; overlapping rectangular regions were coalesced together. Figure 7.5 shows the final results on the two sample images.

7.3.3 Results and observations

For this test, all pixels on the body of the vehicles of the chosen vehicles—excluding tires, mirrors and wind-shields—were considered target pixels. All other pixels, including those from other the background building and tail-lights, were considered background pixels. A false positive pixel was defined as any background pixel that was classified as target, and any cluster of false positive pixels that was larger than 5×5 (this size was empirically chosen to eliminate the effect of pixel-level noise) was considered a false positive region.[37] Any pixel on the body of the vehicle that was not classified as target was considered a false negative (at the pixel level), and if there were no clusters on the vehicle that were marked as targets, that failure was counted as one false negative at

[36] The obvious risk with this assumption is that any specular surface can potentially be mis-classified as a target. For the purposes of this particular test, that risk was ignored.

[37] This 5x5 window size was empirically chosen to eliminate the effect of pixel-level noise; as a result some small objects (e.g., tail-lights) were classified as false positives. In practice, the appropriate window size should be chosen depending on the false positive and false negative thresholds for the particular application.

the region level. Finally, multiple clusters on the body of vehicle were counted as one. Over the 50 images, the average estimation error (measured as the distance between the estimated and true *rgb* colors under each set of conditions) was 0.015, and the true positive pixel classification rate was about 74% (i.e., with 26% false negatives), with a false positive rate of about 11% (See Table 7.2 for more details). Further analysis of the false negatives showed that about 80% of them due to light reflecting off other vehicles in the proximity of the target; for instance, a green car next to the target would make the specular surface of the target appear green rather than red. About 10% of the false positives due to the deposition of snow on the body of the targets; the remaining were simply outside the estimate confidence interval due to minor errors in the estimation. At the region level, all 50 instances of the target were detected, along with 24 false positive regions. As evident from the discussion of pixel-level false positives, all the false negatives were from the red-brick building and the tail-lights.

7.4 Implications

The above results suggest that the NPF and daylight models provide an effective platform for color-based pixel classification in unconstrained outdoor images. However, the results also show that it is difficult to achieve true positive classification rates above 80%. This is primarily due to the confounding factors inherent in unconstrained outdoor (e.g., inter-reflections, which are very difficult to model), suggesting that a significant improvement in performance by adjusting the parameters of the daylight or NPF models is not likely. However, utilization of region-level logic can prove to be a very effective method of capitalizing on correct pixel-level results (which tend to occur in clusters) while minimizing the impact of isolated pixel-level errors. In addition, the high rates of

region-level true and false positives highlight the benefit of combining a color-based system with other sensor modalities (such as stereo-based systems [51] for separating two-dimensional discolorations or patches on the road from three-dimensional objects) for effective sensor fusion.

Sun angle	% Cloud cover	Sun visibility factor	Pixel true positive rate	Pixel false positive rate	Region true positive rate	# region false positives
10	0-5%	1	74%	9%	100%	5
10	100%	0	70%	10%	100%	4
30	0-5%	1	76%	14%	100%	6
30	100%	0	71%	10%	100%	3
50	60-70%	0.5	79%	11%	100%	6

Table 7.2. Results from NPF-based classification for detection for specific instances of a characteristic ("red") shade of automobile. For each of the 5 test conditions, 10 images were sampled (for a total of 50 images). The table shows the true positive rate (74% overall) and false positive rate (11%) at the pixel-level for each set of conditions, along with the percentage of actual instances detected (100%, 50 out of 50) and the number false positives at the region-level (24 separate instances, 0.48 instances per image).

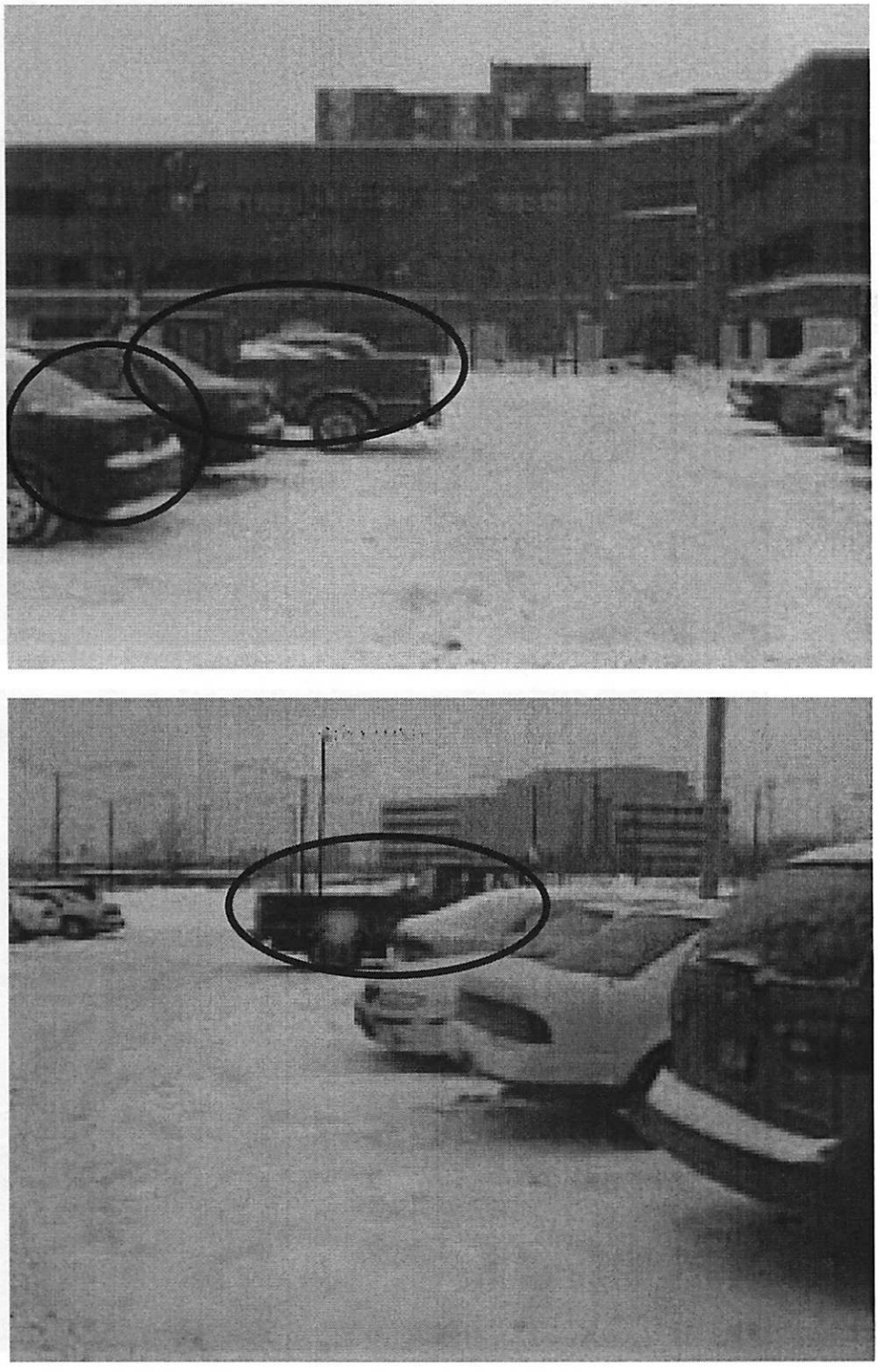

Figure 7.3. Results of NPF-based classification for detecting a instances of automobiles of a characteristic ("red") color: original images with targets marked (dark circles/ellipses).

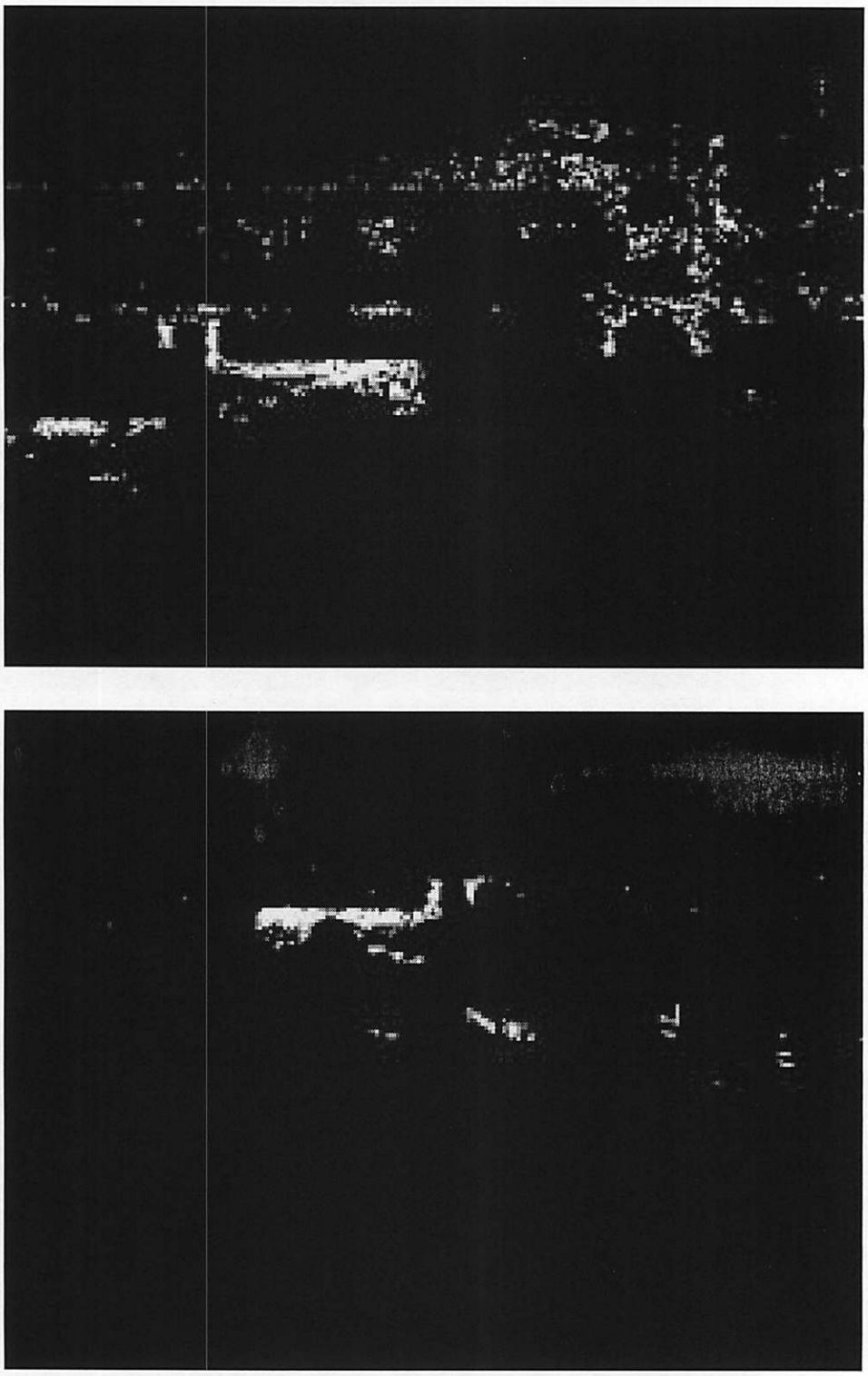

Figure 7.4. Results of NPF-based classification for detecting a instances of automobiles of a characteristic ("red") color: binary images resulting from pixel classification of the images shown in Figure 7.3.

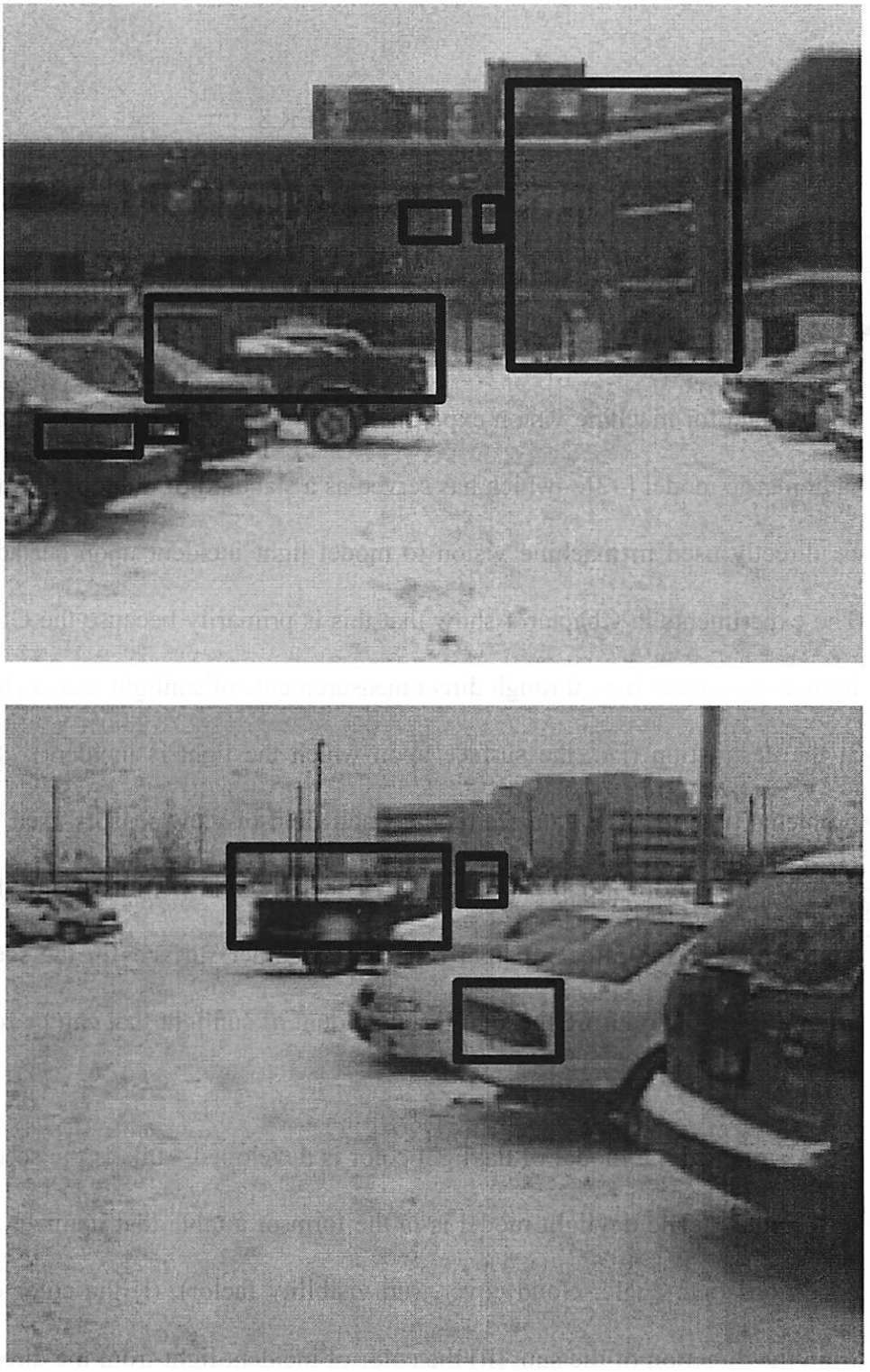

Figure 7.5. Results of NPF-based classification for detecting a instances of automobiles of a characteristic ("red") color: targets extracted (dark boxes) from the binary images shown in Figure 7.4.

CHAPTER 8

CONCLUSIONS

Of the contributions made in this dissertation, the most significant is a demonstration of why a daylight model based on direct sampling of portions of the sky is not appropriate for machine vision experiments. In particular, Chapter 4 shows that the CIE radiometric model [42]—which has served as a standard of outdoor illumination—cannot be directly used in machine vision to model light incident upon surfaces in an image. The experiments in Chapter 4 show that this is primarily because the CIE data measures light at the source (i.e., through direct measurements of sunlight and skylight), rather than at the destination (i.e., the surface upon which the light is incident). Specifically, the problems with the CIE data are (i) the small field-of-view sensors used for the CIE data measure light from too small a portion of the sky, and (ii) measuring directly from the source ignores the effect of light reflected off other surfaces in the scene, such as the ground (thereby ignoring the significant amount of sunlight that can be reflected onto the surface).

As a remedy, a model of daylight color is developed—this is the second contribution of the study. The daylight model is in the form of a table that itemizes, for specific sky conditions (sun angle, cloud cover, sun visibility factor), (i) the color of incident light from the direction of the sun, (ii) the color of incident light from the direction away from the sun, and (iii) the average color of skylight. The table also provides the standard deviations and brightness values for each of these measurements in order to provide an

estimate of the expected consistency of the measurements. An additional (originally unintended) application of the daylight table is in computer graphics models.

The third contribution of the study is a reflectance model (the Normalize Photometric Function) that is a simplification of existing physics-based models [56][70][80] (that cannot be used in outdoor color images) specifically for use in outdoor images. The specific advantages of the NPF are that it (i) reliably models specularity for real surfaces of different reflective characteristics, (ii) accounts for extended illumination (i.e., daylight, which is a combination of sunlight and ambient light), and (iii) eliminates the dependence on brightness (which, as Chapter 4 shows, is extremely inconsistent and hard to predict for incident daylight). Hence, the NPF maintains physics-based accuracy while being simple enough to used in relatively unconstrained outdoor images.

The applicability of the daylight and NPF models to outdoor domains is demonstrated over a large number of images. In the process of developing and testing the models, a number of approximation methods for effectively dealing with the complexities of outdoor images are also developed (such as the polyhedral model of omnidirectional daylight, and the method for imposing brightness constraints in order to reduce false positives).

This study is one of the first attempts at building usable models for color outdoor machine vision. As a consequence, the robustness of the models across a broad range of tests is yet to be proven. To begin with, the daylight model has been tested for three relatively similar geographical locations in North America; it is not clear if the consistency will hold in other parts of the world. Specifically, the effect of humidity, haze and other particulate matter in the air may significantly affect the model. In

addition, the daylight model does not account for the effect of stray light from objects in a complex scene (the simple polyhedral model notwithstanding); this may be a hindrance to applying the model in unconstrained images.

The NPF model has proven to be a simple yet effective way of modeling reflectance over a small set of surfaces. However, the tests over the concrete and asphalt slabs show two weaknesses of this model. First, in neutral-colored surfaces, there may not be enough color information for recognizing surfaces in *normalized* color space; hence, the NPF may not provide as useful a description as an intensity-based model. Secondly, the NPF is a *local* reflectance descriptor; as a consequence, surfaces that are not uniformly colored cannot be easily modeled using such a method.

With the above in mind, potential future work is expected to be be along several directions:

(i) Consolidating the daylight model to account for haze, humidity and other atmospheric factors—this can either be in the form of additional entries in the table, or as a parametric modification to existing entries based on quantifiable measures of the above factors.

(ii) Testing the daylight model for robustness. Specifically, this will involve (a) testing the consistency of the measurements across a broad range of geographical areas, (b) testing robustness across different types of cameras, and (c) building additional parameters (if required, in addition to the polyhedral model) to account for the presence of multiple reflective surfaces in the scene.

(iii) Testing the applicability of the NPF for surfaces that have characteristics different from the ones tested. This could involve testing over a broad range of Lambertian/specular characteristics, as well as uncommon surfaces (e.g., fluorescent, retroreflective) surfaces that can occur in outdoor domains.

(iv) Extending the NPF to model reflectance with non-uniform albedo. Currently, the only way to deal with multicolored surfaces (e.g., the traffic signs discussed in the earlier chapters) is to ignore the secondary colors or model (and look for) one color at a time. A more elegant way of dealing multi-colored surfaces will likely be very useful in building real applications. This will be particularly useful for specular surfaces which may exhibit both Lambertian and specular effects.

(v) Exploring new applications of the developed techniques.

APPENDIX A

RETROREFLECTIVITY

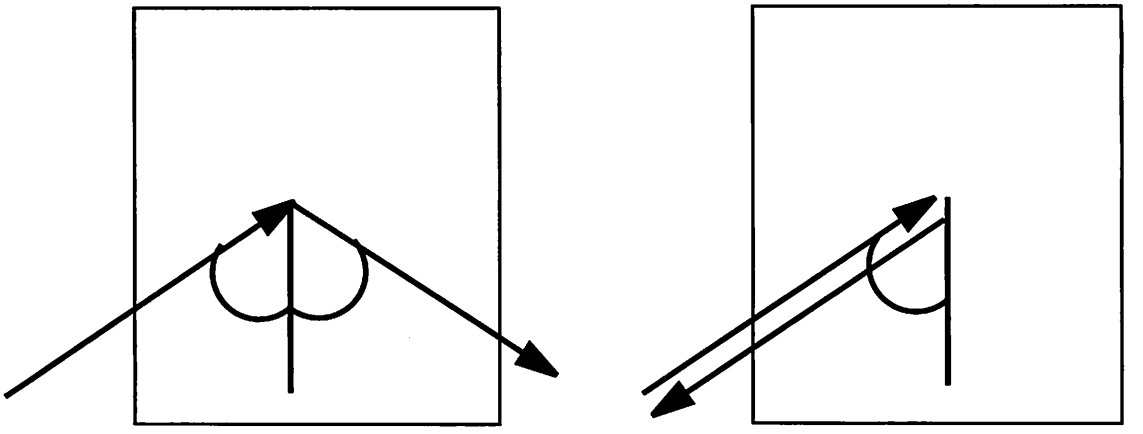

(a) Regular reflection (b) Retroreflection

Figure 9.1. Regular optical reflection vs. retroreflection: (a) In regular reflection, the reflected ray is symmetric to the incident ray across the surface normal; (b) In retroreflection, light is reflected back in the direction exactly opposite to the incident ray.

While retroreflectivity would ordinarily be out of the scope of a discussion of outdoor color machine vision, it is discussed here because the experiments in the earlier chapters use traffic signs. Many government-regulated traffic signs are designed to be retroreflective, typically by mixing tiny beads of glass into the surface coating [1][89]. Retroreflectivity is a phenomenon in which light is reflected back along the direction of illumination; this is done in order to enhance visibility of the signs to drivers at night, when the illumination and viewing directions are assumed to be the same (i.e., the vehicle carrying the driver). This phenomenon is different from regular optical reflection, in which the reflected ray is symmetric to the incident ray across the surface normal. Figure 9.1 contrasts the two phenomena.

All that said, retroreflectivity is a non-issue in the experiments in this study because the traffic signs used here were privately-owned and not retroreflective. Note, also, that retroreflective surfaces are notorious for losing their property rapidly because of dirt and exposure to the elements [1]; consequently, most traffic signs cease to be retroreflective a few months (typically) after installation. Still, understanding how to address retroreflectivity in the context of outdoor color machine vision may prove interesting; hence a brief discussion follows.

Since retroreflectivity is a property specifically designed for night-time conditions (i.e., a single beam of light in an otherwise dark setting), it is important to separate its behavior at night from that under daylight. Under daylight, two further lighting conditions exist: (a) when the surface faces away from the sun and is illuminated by ambient skylight, and (b) when it is directly illuminated by sunlight. In the former case, since the incident light is ambient, light is reflected back along all directions; in effect, this result is exactly the same as regular, non-retroreflective refection.

Under direct sunlight, the process is only slightly more complicated. The reader may recall that in Chapter 5, the relative viewing angle was defined as the difference between the viewing angle and the angle of maximal reflectance. Since light is reflected back along the illuminant direction in retroreflection, the angle of maximal reflectance is also in the direction of incidence. Hence, the relative viewing angle is the angle between the directions of viewing and incidence. The rest of the process of using the NPF, as described in Chapter 5, is exactly the same as that for non-retroreflective surfaces.

The interpretation of the model under night conditions is similar to that under direct sunlight—the relative viewing angle is still the angle between the directions of

illumination and viewing. The only difference is that under daylight, the presence of ambient light makes the surface visible throughout the 180° field-of-view. Presumably, the night-light is a non-ambient beam of light, which means that the surface is visible from a much smaller range of viewing angles.

APPENDIX B

FLUORESCENCE

Fluorescence is the property that causes a surface to reflect light along a wavelength that is longer than the incident light. The complication in modeling fluorescent reflectance is that typically, a matrix specifying the complete spectra emitted as the result of being exposed to a given wavelength is required [3]. Barnard [3] shows that it is possible to model fluorescence based on some canonical illuminants. It may be possible to use Barnard's method in place of the color-coefficient matrix to model the diffuse component of surface reflectance under each of the entries in the daylight table, and then apply the NPF to model specularity. However, since that line of research was considered out of the scope of this particular study, it is not discussed further here; that said, it is one potential subject of extensions to this study.

BIBLIOGRAPHY

[1] Anders, R. *On-road investigation of fluorescent sign colors to improve conspicuity*, Master of Science Thesis, Virginia Polytechnic Institute and State University, 2000.

[2] Arend, L. and Reeves, A. "Simultaneous color constancy", *Journal of the Optical Society of America*, 3(10):1743-1751, 1986.

[3] Ballard, D. and Brown, C. *Computer Vision*, Prentice-Hall, Englewood Cliffs, NJ, 1982.

[4] Barnard, K. "Color constancy with fluorescent surfaces", *Proceedings of the IS\&T/SID Seventh Color Imaging Conference: Color Science, Systems and Applications*, 1999.

[5] Boult, T. and Wolberg, G. "Correcting Chromatic Aberrations Using Image Warping", *DARPA Image Understanding Workshop*, 1992.

[6] Benzschawel, T., Brill, M. and Cohn, T. "Analysis of human color mechanisms using sinusoidal spectral power distributions", *Journal of the Optical Society of America*, 3(10):1713-1725, 1986.

[7] Brainard, D. and Wandell, B. *An Analysis of the Retinex Theory of Color Vision*, Stanford University Press, Stanford, CA, 1985.

[8] Buchsbaum, G. "A Spatial Processor Model for Object Colour Perception", *Journal of the Franklin Institute*, 310:1-26, 1980.

[9] Budde, W. Unpublished, referenced in \cite.

[10] Buluswar, S. and Draper, B. "Color Recognition in Outdoor Images", *Proceedings of the International Conference on Computer Vision*, 1998.

[11] Buluswar, S. and Draper, B. "Nonparametric Classification of Pixels Under Varying Outdoor Illumination", *Proceedings of the DARPA Image Understanding Workshop*, 1994.

[12] Chen, Y. and Hsu, Y. "Computer Vision on a Color-Blindness Plate", *Image and Vision Computing*, 13(6):463-478, August 1995.

[13] Cheng, F., Hsu, W. and Chen, T. "Recovering Colors in an Image with Chromatic Illuminant", *Image Processing*, 7(11), November 1998.

[14] Condit, H. and Grum, F. "Spectral Energy Distribution of Daylight", *Journal of the Optical Society of America*, 54(7):937-944, 1964.

[15] Cook, R. and Torrance, K. "A Reflectance Model For Computer Graphics", *Image Understanding*, 2:1-19, 1987.

[16] Crisman, J. and Thorpe, C. "Color Vision for Road Following", *Vision and Navigation: The Carnegie Mellon NAVLAB*, Kluwer, 1990.

[17] Dana, K., van Ginneken, B., Nayar, S. and Koenderink, J. "Reflectance and Texture of Real World Surfaces", *ACM Transactions on Graphics*, 18(1):1-34, 1999.

[18] Digital Video Cameras Co., On-line user information, *http://www.edt.com/dvc/gamma.html*.

[19] Dixon, E. "Spectral distribution of Australian daylight", *Journal of the Optical Society of America*, 68(4), July, 1964.

[20] Finlayson, G. "Color Constancy in Diagonal Chromaticity Space", *Proceedings of the Fifth International Conference on Computer Vision*, 1995.

[21] Finlayson, G., Funt, B. and Barnard, K. "Color Constancy Under Varying Illumination", *Proceedings of the Fifth International Conference on Computer Vision*, 1995.

[22] Finlayson, G.D., Drew, M.S. and Funt, B.V. "Diagonal Transforms Suffice", *Journal of the Optical Society of America*, 11(11):3011-3019, 1994.

[23] Finlayson, G., Hordley, S. and Hubel, P. "Color by Correlation: A Simple, Unifying Approach to Color Constancy", *Proceedings of the International Conference on Computer Vision*, 1998.

[24] Forsyth, D. "A Novel Approach for Color Constancy", *International Journal of Computer Vision*, 5:5-36, 1990.

[25] Freeman, W. and Brainard, D. "Bayesian Decision Theory: the maximum local mass estimate", *Proceedings of the Fifth International Conference on Computer Vision*, 1995.

[26] Funt, B. and Finlayson, G. "The State of Computational Color Constancy", *Proceedings of the First Pan-Chromatic Conference, Inter-Society Color Council*, 1995.

[27] Funt, B. and Drew, M. "Color Space Analysis of Mutual Illumination", *IEEE Transactions on Pattern Analysis and Machine Intelligence*, 12:1319-1326, 1993.

[28] Funt, B. and Finlayson, G. "Color constant color indexing" *IEEE Transactions on Pattern Analysis and Machine Intelligence*, 17(5):522-529, 1995.

[29] Funt, B., Barnard, K. and Martin, L. "Is Machine Color Constancy Good Enough?", *Proceedings of the Fifth European Conference on Computer Vision*, 1998.

[30] Funt, B., Cardei, V. and Barnard, K. "Method of Estimating Chromaticity of Illumination using Neural Networks" *Proceedings of the IS\&T/SID Fourth Color Imaging Conference*, 1996.

[31] Gershon, R., Jepson, A. and Tsotsos, J. *The Effects of Ambient Illumination on the Structure of Shadows in Chromatic Images*. RBCV-TR-86-9, Dept. of Computer Science, University of Toronto, 1986.

[32] Grum, F. and Bartleson, C. *Optical Radiation Measurements: Color Measurement*, Academic Press, 1980.

[33] Healy, G. "A Color Reflectance Model and its use for Segmentation", *International Conference on Computer Vision*, 1988.

[34] von Helmholtz, H. *Handbuch der Physiologischen Optik*, Voss, Hamburg, 1896.

[35] Henderson, S. and Hodgkiss, D. "The Spectral Energy Distribution of Daylight", *British Journal of Applied Physics*, 14:125-131, 1963.

[36] Henry, R. "Colorimetry in the Natural Atmosphere", *Proceedings of the First Pan-Chromatic Conference*, 1995.

[37] Hill, F. *Computer Graphics*, Macmillan, New York, 1990.

[38] Horn, B. *Robot Vision*, MIT Press, Cambridge, MA, 1987.

[39] Horn, B. "Understanding Image Intensities", *Artificial Intelligence*, 8:201-231, 1977.

[40] Horowitz, P. and Hill, W. *The Art of Electronics*, Cambridge University Press, Cambridge, UK, 1989

[41] Jackowski, M., Goshtasby, A., Bines, S., Roseman, D. and Yu, C. "Correcting the Geometry and Color of Digital Images", *IEEE Transactions on Pattern Analysis and Machine Intelligence*, 19(10):1152-1158, October 1997.

[42] Judd, D., MacAdam, D. and Wyszecki, G. "Spectral Distribution of Typical Daylight as a Function of Correlated Color Temperature", *Journal of the Optical Society of America*, 54(8):1031-1040, 1964.

[43] Klinker, G., Shafer, S. and Kanade, T. "Color image analysis with an intrinsic reflection model", *Proceedings of the International Conference on Computer Vision*, 1988.

[44] von Kries, J. "Die Gesichtsempfindungen", *Handbuch Physiologie Menchen*, 1904.

[45] Land, E. "Lightness and Retinex Theory", *Scientific American*, 237(6):108-129, December 1977.

[46] Lee, H., Breneman, E. and Schulte, C. "Modeling light reflection for computer color vision", *IEEE Transactions on Pattern Analysis and Machine Intelligence*, 12:402-409, 1990.

[47] Lee, S. *Understanding of Surface Reflections in Computer Vision by Color and Multiple Views*, Ph.D. Dissertation, University of Pennsylvania, 1992.

[48] Lenz, R., Osterberg, M., Hiltunen, J., Jaaskelainen, T. and Parkkinen, J. "Unsupervised filtering of color spectra," *Journal of the Optical Society of America*, 13(7):1315-1324, 1996.

[49] Maloney, L. and Wandell, B. "Color Constancy: A Method for Recovering Surface Spectral Reflectance", *Journal of the Optical Society of America*, A3:29-33, 1986.

[50] Matloff, N. *Probability Modeling and Computer Simulation*, PWS-Kent, Boston, 1988.

[51] Matthies, L. "Stereo Vision for Planetary Rovers: Stochastic Modeling to Near Real-Time Implementation", *International Journal of Computer Vision*, 8(1):71-91, 1992.

[52] Maxwell, B. and Shafer, S. "A framework for segmentation using physical models of image formation", *IEEE Computer Society Conference on Computer Vision and Pattern Recognition*, 1994.

[53] Meeus, J. *Astronomical Formulae for Calculators*, Willman-Bell, Richmond, 1985.

[54] Montag, J. "Influence of Boundary Information on the Perception of Color", *Journal of the Optical Society of America-A*, 14(5):997-1006, May 1997.

[55] Munsell Color (Corp.), *Munsell Book of Color - Matte Finish Collection*, Baltimore, MD, 1976.

[56] Nayar, S., Ikeuchi, K. and Kanade, T. "Determining Shape and Reflectance of Hybrid Surfaces by Photometric Sampling", *IEEE Transactions on Robotics and Automation*, 6:418-431, 1990.

[57] Nayar, S., Ikeuchi, K. and Kanade, T. "Surface Reflection: Physical and Geometric Perspectives", Carnegie Mellon University technical report, CMU-RI-TR-89-7, 1989.

[58] Nayatani, Y. and Wyszecki, G. "Color of Daylight from North Sky", *Journal of the Optical Society of America*, 53(5):626-629, 1963.

[59] Nicodemus, F., Richmond, J., Hsia, J. Ginsberg, I. and Limperis, T. "Geometrical considerations and nomenclature for reflectance", *NBS Monograph 160*, National Bureau of Standards, 1977.

[60] Novak, C., Shafer, S. and Wilson, R. "Obtaining Accurate Color Images for Machine Vision Research", *Proceedings of the SPIE*, v 1250, 1990.

[61] Novak, C. and Shafer, S. *A Method for Estimating Scene Parameters from Color Histograms*, Carnegie Mellon University School of Computer Science, technical report, CMU-CS-93-177, 1993.

[62] Novak, L. and Hesse, S. "Optimal Polarizations for Radar Detection and Recognition of Targets in Clutter", *Proceedings of the SPIE*, 1992.

[63] Ohta, Y. and Hayashi, Y. "Recovery of Illuminant and Surface Colors from Images Based on the CIE Daylight", *Proceedings of the Third European Conference on Computer Vision*, 1994.

[64] Ohta, Y. *A region-oriented image-analysis system by computer*, Doctoral Dissertation, Kyoto University, Japan, 1980.

[65] Oren, M. and Nayar, S. "Generalization of the Lambertian Model and Implications for Machine Vision", *International Journal of Computer Vision*, 14(3):227-251, 1995.

[66] Parkkinen, J. "Color Spectra Database", Lappeenranta University of Technology on-line data, *http://www.lut.fi/ltkk/tite/research/color/lutcs_database.html*.

[67] Parraga, C., Brelstaff, G., Troscianko, T. and Moorehead, I. "Color and Luminance Information in Natural Scenes", *Journal of the Optical Society of America-A*, 15(3):563-569, March 1998.

[68] Petrov, A. "Surface Color and Color constancy", *Journal of Color Research and Application*, 18(4):236-240, 1993.

[69] Pietikaeinen, M., Nieminen, S., Marszalec, E. and Ojala, T. "Accurate Color Discrimination with Classification Based on Feature Distributions", ICPR 91(2), 1996.

[70] Phong, B. "Illumination for Computer Generated Images", *Communications of the ACM*, 18:311-317.

[71] Plataniotis, K., Androutsos, D., Vinayagamoorthy, S., and Venetsanopoulos, A. "Color Image-Processing Using Adaptive Multichannel Filters", *Image Processing*, 6(7):933-949, July 1997.

[72] Poggio, T. and Girosi, F. "Regularization algorithms for learning that are equivalent to multilayer networks", *Science*, 247:978-982, 1990.

[73] Pomerleau, D. *Neural Network Perception for Mobile Robot Guidance*, Kluwer Academic Publishers, Boston, 1993.

[74] Pomerleau, D. "RALPH: Rapidly Adapting Lateral Position Handler", *IEEE Symposium on Intelligent Vehicles*, 1995.

[75] Ripley, B. *Pattern Recognition and Neural Networks*, Cambridge University Press, 1996.

[76] Rogers, D. *Procedural Elements for Computer Graphics*, McGraw-Hill, New York, 1985.

[77] Sato, Y. and Ikeuchi, K. "Reflectance analysis under solar illumination", *Proceedings of the IEEE Workshop for Physics-based Modeling in Computer Vision*, 1995.

[78] Sato Y. and Ikeuchi, K. "Temporal-color Space Analysis of Reflection", *Journal of the Optical Society of America*, 11(11):2990-3002,November, 1994.

[79] Schachter, B., Davis, L. and Rosenfeld, A. "Some Experiments in Image Segmentation by Clustering of Local Feature Values", *Pattern Recognition*11(1):19-28, 1979.

[80] Shafer, S. "Using Color to Separate Reflection Components", *Color Research Application*, 10:210-218, 1985.

[81] Simonds, J. "Application of characteristic vector analysis to photographic and optical response data", *Journal of the Optical Society of America*, 53(8), 1963.

[82] Swain, M. and Ballard, D. "Color Indexing", *International Journal of Computer Vision*, 7:11-32, 1991.

[83] Swain, M. "Happy patrons make better tippers: Creating a robot waiter using Perseus and the Animate Agent Architecture", *The 2nd International Conference on Automatic Face- and Gesture-Recognition*, 1996.

[84] Syeda-Mahmood, T. "Detecting Perceptually Salient Texture Regions in Images", *Computer Vision and Image Understanding*, 76(1):93-108, October, 1999

[85] Syeda-Mahmood, T. and Cheng, Y. "Indexing Colored Surfaces in Images", *The Proceedings of the International Conference on Pattern Recognition*, 1996.

[86] Thompson, E., Palacios, A. and Vareln, F. "Ways of coloring: Comparative color vision as a case study for cognitive science", *Behavioral Brain Sciences*, 15, 1992.

[87] Torrance, K. and Sparrow, E. "Theory for Off-Specular Reflection from Roughened Surfaces", *Journal of the Optical Society of America*, 57:1105-1114, 1967.

[88] Trussell, H. and Kulkarni, M. "Sampling and Processing of Color Signals", *Image Processing*, 5(4):677-681, April 1996.

[89] U.S. Department of Transportation, Federal Highway Administration, *Manual on uniform control devices*, 2000.

[90] Vrhel, M. and Trussell, H. "Filter considerations in color correction" *IEEE Transactions on Image Processing*, 3:147-161, 1994.

[91] Vriesenga, M., Healey, G., Sklansky, J. and Peleg, K. *Colored Illumination for Enhancing Discriminability in Machine Vision, Journal of Visual Communication and Image Representation*, 6(3):244-255, September 1995.

[92] Wandell, B. *Foundations of Vision*, Sinauer Associates, Sunderland, MA, 1995.

[93] Wolff, L., Nayar, S. and Oren, M. "Improved Diffuse Reflection Models for Computer Vision", *International Journal of Computer Vision*, 30(1):55-71, 1998.

[94] Wyszecki, G. and Stiles, W. *Color Science: Concepts and Methods, Quantitative Data and Formulas*, John Wiley and Sons, Inc., New York, 1982.

[95] Yuille, A. "A method for computing spectral reflectance", *Biological Cybernetics*, 56:195-201, 1987.

[96] Zaccarin, A. and Liu, B. "A Novel Approach For Coding Color Quantized Images", *Image Processing*, 2(4):442-453, 1994.

[97] D'Zmura, M. and Iverson, G. "Color Constancy: Basic theory of two stage linear recovery of spectral descriptions for lights and surfaces" *Journal of the Optical Society of America*, A 10:2148-2165, 1993.

[98] Zombeck, M. *Handbook of Space Astronomy and Astrophysics*, Cambridge University Press, Cambridge, UK, 1990.